Development of a Static Fourier Transform Spectrometer and Real-Time Substrates for Surface Enhanced Raman Scattering

by

Behzad Sardari Ghojehbeiglou

Submitted to the Institute of Engineering and Natural Sciences
in partial fulfillment of
the requirements for the degree of
Doctor of Philosophy

Sabancı University
July 2017

Development of a Static Fourier Transform Spectrometer and Real-Time Substrates for
Surface Enhanced Raman Scattering

APPROVED BY:

Assoc. Prof. Dr. Meriç Özcan
(Thesis Supervisor)

Assoc. Prof. Dr. Cleva Ow-Yang

Prof. Dr. Ibrahim Tekin

Prof. Dr. Necati F. Ecevit

Prof. Dr. Rauf Süleymanov

DATE OF APPROVAL: 26/07/2017

Abstract

In the first part of this thesis a novel broadband static Fourier transform spectrometer (static-FTS) configuration based on the division of the optical spectrum into multiple narrow-bands is proposed and implemented by combining a static-FTS and dispersive elements. Dividing the broadband input spectrum into narrow-band signals we have used the band-pass sampling theorem to reduce the sampling frequency (or increase the scanning step in the FTS concept). The dispersive part includes a double diffraction grating structure to disperse the input spectrum in horizontal direction (to divide the input light into multiple narrow-band signals) and the static-FTS part includes a static Michelson interferometer to make different path length differences (PLD) in the vertical direction. The static Michelson interferometer is composed of a beam-splitter (BS), a flat mirror and a stair-case mirror. However, in actual setup a diffraction grating in Littrow configuration is used to realize the stair-case mirror. Using off-shelf diffraction gratings as the stair-case mirror decreases the total cost of the prototyped device. A CCD camera is used at the exit port of the static-FTS part, to record the formed interferograms.

The proposed novel configuration based on band-pass sampling theorem not only decreases the spectrometer size but also allows operation in the traditional spectrometer wavelength range, namely 400 nm - 1100 nm with better resolution. This technique solves the Nyquist sampling rate issue and enables recording high resolution spectrums with regular CCDs. The proposed configuration and the method, in fact, solve the trade of between resolution and bandwidth, and also eliminate the need for nanometer step size mirrors. An algorithm is developed to process the recorded signal and calculate the Fourier transform of the recorded interferograms on the CCD camera.

In the second part, we have shown the capability of copper oxide (CuO) nanoparticles formed on copper (Cu) electrodes by the electrolysis as a real time active substrate for surface enhanced Raman scattering (SERS). We have experimentally found that using just the ultra pure water as the electrolyte and the Cu electrodes, ions are extracted from the copper anode form copper oxide nanoparticles on the anode surface in matter of minutes. Average particle size on the anode reaches to $100\,nm$ in ninety seconds and grows to about $300\,nm$ in five minutes. This anode is used in SERS experiments in real time as the nanoparticles were forming and the maximum enhancement factor (EF) of Raman signals were over five orders of magnitude. Other metal electrodes made of brass, zinc (Zn), silver (Ag) and aluminum (Al) also tested as candidate anode materials for their potential as real-time substrates for SERS applications. Experimentally obtained enhancement factors were above five orders of magnitude for brass electrodes like the copper but for the other metals no enhancement is observed. Electron microscope images show the cubic nanoparticle formation on copper and brass electrodes but none in the other metals studied. The standard electrode potential of the electrodes plays the key role in production of the nanoparticles.

The proposed method has some key advantages over existing SERS substrates: its not only a real time SERS substrate but also is a very fast, simple and a low cost technique. Furthermore this substrate is tunable in wavelength -albeit only irreversibly and in one direction- as the particle size is increasing as a function of time which implies that plasmon resonance wavelengths are increasing as well. This technique also omits the need for an electrolyte containing the metal ions of interest for the nanoparticle production as just the deionized or distilled water is enough. This is an important point for the SERS measurements because the electrolyte being simply just the water there will not be an extra background noise added to the spectrum. This technique also allows preparation of a large effective area for SERS enhancement, virtually unlimited area. As long as the current distribution over the anode is uniform which is a trivial arrangement, nanoparticle distribution will have quite homogeneous distribution. The homogeneous nanoparticle distribution means a uniform enhancement factor on the produced substrate.

Özet

Bu tezin ilk bölümünde, optik tayfın çok dar bantlara bölünmesine dayanan geniş bant statik-Fourier dönüşüm spektrometre (statik-FTS) kurulumu önerilmiş ve bu özgün kurulum statik-FTS ile dağıtıcı (dispersiv) elemanlar birleştirilerek gerçekleştirilmiştir. Geniş bantlı giriş tayfını dar bantlı sinyallere bölebilmek için bant geçiren örnekleme teoremi kullanılmıştır. Bu teorem, örnekleme frekansını azalttığı (veya FTS konseptinde tarama adımını arttırdığı) bilinmektedir. Dağıtıcı parça, girdi spektrumunu yatay yönde dağıtmak ve giriş sinyalini çoklu dar bant sinyallere bölmek için bir çift kırınım ızgara yapısı içerir. Statik-FTS ise dikey doğrultuda farklı yol uzunluğu farkları oluşturmak için Michelson girişimölçer içerir. Statik Michelson girişimölçeri; ışın ayırıcı (beam splitter), bir ayna ve merdiven aynasından (staircase mirror) oluşur. Ancak, gerçek kurulumda merdiven aynası yerine Littrow kurulumundaki kırınım ızgarası kullanılmış ve bu durum prototip cihazın toplam maliyetini düşürmüştür. Oluşturulan girişim eğrilerini kaydetmek için statik-FTS parçasının çıkış portuna CCD kamera yerleştirilmiştir.

Bant geçiren örnekleme teoremine dayanan özgün kurulum, spektrometrenin boyutunu düşürmekle kalmaz aynı zamanda geleneksel spektrometre dalga boyu aralığında (400 nm - 1100 nm) ve daha iyi çözünürlükte çalışmayı sağlar. Bu teknik, Nyquist örnekleme hız problemini çözer ve normal CCD' lerle yüksek çözünürlüklü tayfların kaydedilmesini sağlar. Önerilen kurulum ve yöntem, çözünürlük ve bant genişliği arasındaki sorunu çözmekte ve aynı zamanda nanometre büyüklüğündeki ayna ihtiyacını ortadan kaldırmaktadır. Kaydedilen sinyali işlemek ve CCD kamera ile kaydedilen girişim eğrilerinin Fourier dönüşümünü hesaplamak için bir algoritma geliştirilmiştir.

İkinci bölümde, bakır (Cu) elektrotlarında elektroliz yoluyla oluşturulan ve gerçek zamanlı aktif alt madde (substrate) olan bakır oksit (CuO) nanoparçacıkların yüzey gerilimli Raman saçılımı (SERS) için kabiliyeti araştırılmıştır. Sadece elektrolit olarak saf su ve bakır elektrotlar kullanıldığında, anot yüzeyinde bakır oksit nanoparçacıkların bir kaç dakika içerisinde oluştuğu deneysel olarak gözlemlenmiştir. Anot üzerindeki ortalama parçacık boyutu doksan saniye içinde 100 nm' ye ulaşır ve beş dakikada yaklaşık 300 nm' ye kadar büyür. Nanoparçacıklar oluştukça ve Raman sinyallerinin azami iyileştirme faktörü (EF) 10^5 kattan fazla oldukça; bu anot SERS deneylerinde gerçek zamanlı olarak kullanılır. Pirinç, çinko (Zn), gümüş (Ag) ve alüminyumdan (Al) yapılmış diğer metal elektrotlar, potansiyel anot malzemesi olarak ve gerçek zamanlı SERS uygulamaları için test edilmiştir. Deneysel olarak elde edilen iyileştirme faktörleri, bakır gibi pirinç elektrotlar için 10^5 kat büyüklüğünde olduğu gözlemlenmiş, ancak diğer metaller için herhangi bir iyileşme gözlenmemiştir. Elektron mikroskop görüntülerinde bakır ve pirinç elektrotların üzerlerinde kübik nanoparçacık oluşumunu gözlenmiş ancak diğer metallerin hiçbirinde buna benzer bir durum gözlenmemiştir. Elektrotların standart elektrot potansiyeli, nanoparçacıkların üretiminde önemli bir rol oynamaktadır.

Önerilen yöntem, mevcut SERS alt maddelerine kıyasla bazı önemli avantajlara sahiptir. Bunlar; gerçek zamanlı SERS alt maddesi olması ile çok hızlı, basit ve düşük maliyetli bir teknik olmasıdır. Dahası, parçacık boyutu zamanın bir fonksiyonu olarak arttıkça (bu durum plazmon rezonans dalga boylarının da arttığına işaret eder) alt madde dalga boyu ile ayarlanabilir. Bu teknikte, sadece iyondan arındırılmış veya damıtılmış su yeterli olduğu için nanoparçacık üretiminde kullanılan ve metal iyonları içeren elektrolite ihtiyaç duyulmaz. Bu, SERS ölçümleri için önemli bir noktadır; çünkü elektrolit sadece sudur ve böylece tayfa fazladan bir arka plan gürültüsü eklenmez. Bu teknik, aynı zamanda, SERS iyileştirmesi için geniş etkili bir alan hazırlanması sağlar. Anot üzerindeki akım dağılımı tek biçimli (uniform) olduğu sürece, nanoparçacık dağılımı oldukça homojen bir dağılıma sahip olacaktır. Homojen nanoparçacık dağılımı, üretilen alt katman üzerinde tek biçimli bir iyileştirme faktörü anlamına gelir.

Acknowledgments

I would like to thank to my supervisor Assoc. Prof. Meriç Özcan for guiding and supporting me throughout the PhD years, at Sabanci University. So happy and lucky to have a supervisor who cared about my work and my future.

I would also like to thank to the jury members of my thesis defense Prof. Necati F. Ecevit, Prof. Rauf Süleymanov, Prof. Ibrahim Tekin and in particular, Assoc. Prof. Cleva Ow-Yang for their interest and useful comments to improve my thesis and presentation.

Moreover, I also would like to thank Sirous Khabbaz, Omid Akhlaghi, and Ali Toufani for their help in taking SEM images.

Furthermore, I like to thank The Scientific and Technological Research Council of Turkey (TÜBİTAK) for supporting scholarship and funding this thesis work through the project named "Development of Fast and High Resolution Raman Spectrometer" under the research fund No: 113F357.

Finally, I would like to thank my family for supporting and encouraging me during the long years far away from them.

Contents

List of Figures

Chapter 1

Introduction to Spectroscopy

The broad-band, high signal-to-noise ratio (SNR) and high resolution spectrometers are highly in demand for industrial and scientific measurements such as atmospheric sounding, bacteria detection, etc. [1–5]. Among the spectroscopy techqniques, the fast, high SNR and high resolution capability of the Fourier transform spectroscopy [FTS] [6] makes this method as a unique method in a wide range of applications such as chemical and surface analysis [7, 8], bio detection [9, 10], environmental applications such as pollutant concentration measurement in atmosphere [11, 12].

The spectrometers are essentially divided into two different categories; dispersive spectrometers and Fourier transform spectrometers (FTS). Dispersive spectrometers (see Fig. 1.1 and Fig. 1.3) relies on the diffraction of light from the diffraction gratings (DG), while, the Fourier transform spectrometers (see Fig. 1.4) relies on the self interference of light through a Michelson interferometer at different path length differences (PLD) [13–15].

The PLD for light interference through a Michelson interferometer (see Fig. 1.4) is mainly created by two different techniques; moving mechanism and static mechanism (called static - FTS). In moving mechanism, one of the flat mirror is fixed while the second one moves and produces PLD. In static mechanism (see Fig. 1.6), one flat mirror and one stair-case mirror are used rather than two flat mirrors; in which the individual steps (in the stair-case mirror) create different PLDs.

The FTSs have some classified advantages over dispersive spectrometers such as the multiplex (Fellgett's advantage), the high throughput (Jacquinot's advantage) and the wavelength accuracy (Connes' advantage) [16–18].

In FTSs with moving mechanism a very high resolution and precision sampling mechanism is required to satisfy the Nyquist sampling rate, which according to this theorem the minimum sampling frequency must be at least twice the highest frequency in the signal. This restriction makes the moving mechanism a complicated and costly process. Therefore, static mechanism is developed to overcome this drawback of the moving mechanism based FTSs. However, the existing static-FTSs have to operate either at longer wavelengths (micrometer or above) or in a narrow-band spectrum (due to Nyquist sampling theorem), and in general they have low resolution. Also, they are not necessarily any smaller size than the traditional FTIR [19–23], and fabrication of staircase mirrors in nano or micro scales is costly and needs high-tech fabrication facilities.

In reference [19], staircase mirrors have been used instead of the fixed and scanning mirrors setup to create the PLD. This system works around $10\,\mu m$ wavelengths and, in the best case, resolution is limited to $8\,cm^{-1}$. Micro multi-step mirrors (MMSMs) were fabricated by micro optical electro mechanical systems (MOEMS) technology to guarantee accurate PLD. The proposed configuration in reference. [20] uses two tilted mirrors instead of a fixed and a scanning mirror to realize the static-FTIR. The bandwidth and the resolution of this setup are limited to $150\,nm$ and $8\,cm^{-1}$, respectively. Noise analysis was done in this work as well as the theoretical limits on the resolution and signal-to-noise ratio (SNR) was studied. In another work [21] which is dedicated for carbon monoxide detection, tilted mirrors are used as well. It has high resolution of $0.1\,cm^{-1}$ but very narrow range of operation around $2.2\,\mu m$. In reference [22], the proposed static-FTIR works in mid-infrared region between $7.2\,\mu m$ and $16\,\mu m$ with resolution of $8\,cm^{-1}$. A single mirror with a beam splitter and a convex lens are used to create different PLDs. In reference [23], a Fourier transform near-infrared spectrometer was proposed in which PLD are created by a corner cubes. The proposed configuration works in a very narrow band region of infrared region but with resolution of $1\,cm^{-1}$. Basically, all these studied configurations are narrow-band, operate at longer wavelengths and/or suffer from low resolution.

1.1 How Does a Dispersive Spectrometer Work?

Generally, the dispersive spectrometers can be categorized from the detector point of view, which two different configurations are commercially available. 1. Dispersive spectrometers with a CCD and, 2. Dispersive spectrometers with a photodetector. Dispersive spectrometer with a CCD does not need any moving mechanism, while in the dispersive spectrometers with a photodetector, a rotating mechanism is required to focus the desired wavelengths on the photodetector.

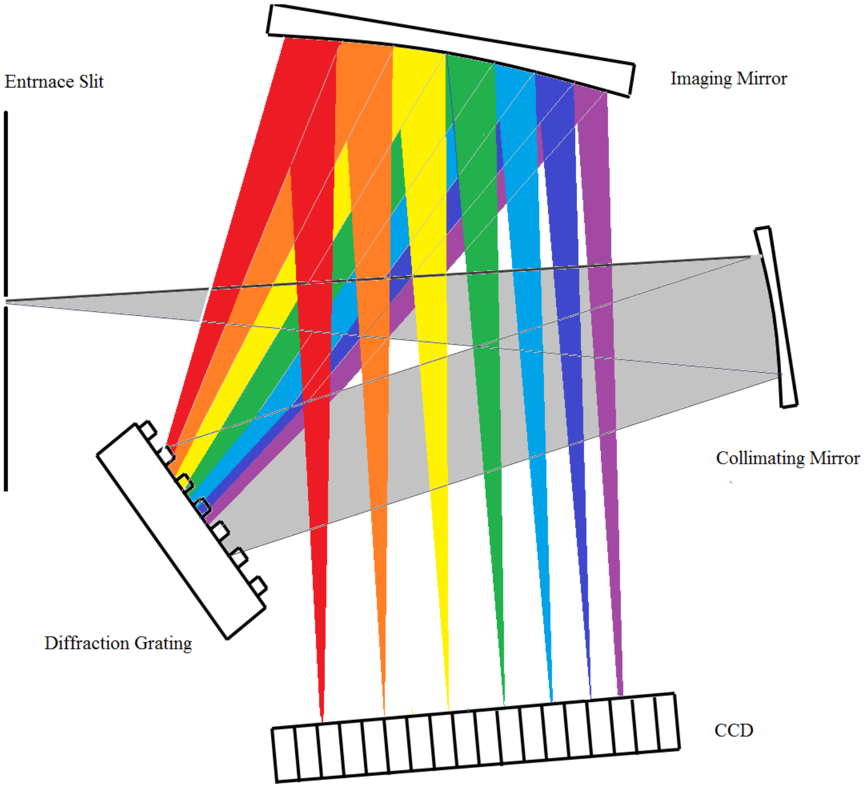

Figure 1.1: Czerny-Turner configuration as a dispersive spectrometer.

There are three most common optical configurations for dispersive spectrometers with CCD, called crossed Czerny-Turner, unfolded Czerny-Turner, and concave holographic spectrographs. Here the crossed Czerny-Turner is discussed in detail. Crossed Czerny-Turner configuration as a dispersive spectrometer and the ray paths on this configuration are illustrated in Fig. 1.1 and Fig. 1.2. This configuration is composed of a diffraction grating and two concave mirrors. The entrance slit is placed at the focal

Figure 1.2: A CCD based dispersive spectrometer made by Ocean Optics, Inc. [24] This spectrometer has a 1-D CCD of 3648 pixels and wavelength range of $200\,nm - 1100\,nm$. It can be connected to a computer by a USB cable.

length of the collimating mirror which this mirror directs the collimated beam of light onto the diffraction grating. The diffraction grating diffracts and separates the incident beams of light into its chromatic components. Finally, imaging mirror is used to focus the dispersed light from the diffraction grating onto the CCD plane. Each pixel on the CCD corresponds to different wavelengths.

A Czerny-Turner monochromator configuration as the dispersive spectrometer with photodetector and the ray paths are illustrated in Fig.1.3. This configuration composed of two concave mirrors called collimating mirror and focusing mirror, two slits as the entrance slit and the exit slit, and a diffraction grating mounted on a rotating base. In this configuration, the broad-band light source passes through an entrance slit. The entrance slit is placed at the focal point of a collimating mirror (to collimate the incident beams). A diffraction grating mounted on a rotating base (to focus the desired wavelength on the exit slit) is used to diffract the collimated light. The diffracted light is collected by the focusing mirror which focuses the dispersed light on exit slit plane. Therefore, the light is spread out on the slit plane.

Each color on the exit slit plane is the image of the entrance slit which focused on the plane. Therefore, the slit width determines the the sharpness of the images. The narrower the slit, the sharper the image. Due to finite with of the slit which causes the overlap of the nearby images, it can be concluded that the detected light behind the exit slit, contains the image of the entrance slit at the selected wavelength as well as the image of the entrance slit at the adjacent wavelengths. The portion of the overlap among the adjacent wavelengths depends on the entrance slit width and diffraction grating. Mounting the diffraction grating on a rotating base enables focusing the desire entrance slit image on the exit slit.

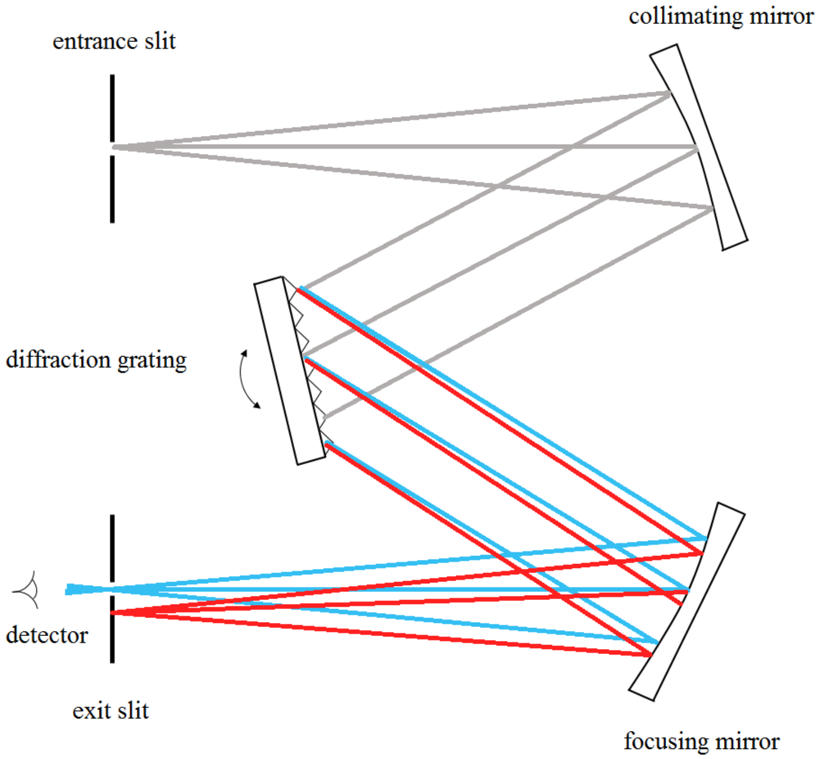

Figure 1.3: A Czerny-Turner monochromator configuration as the dispersive spectrometer with photodetector.

1.2 How Does a Fourier Transform Spectrometer Work?

The general form of a Fourier transform spectrometer is schematically represented in Fig. 1.4 and Fig. 1.5. These kind of spectrometers principally work as follow: The incident light is split into two separate arms in which one of these hits a fixed flat mirror while the other one hits a mobile flat mirror. The reflected lights from the mirrors interfere on the detector plane, and the detector records the intensity of their interference. Obviously, the interference depends on the phase difference of the reflected lights from the mirrors. The phase difference is the result of the path length difference (PLD) of the two arms ($2 \times (x_1 - x_2)$), which, for instance, at $PLD = 0$ and $PLD = \lambda/2$ they yield constructive interference and destructive interference respectively.

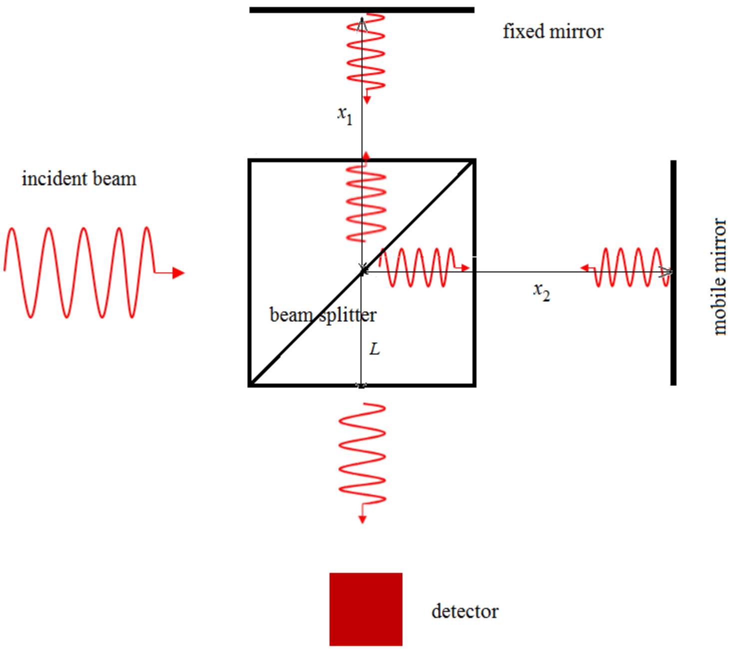

Figure 1.4: Michelson interferometer as a spectrometer; the reflected beams from the flat mirrors interfere on a photodetector. The created PLD is $2(x_1 - x_2)$.

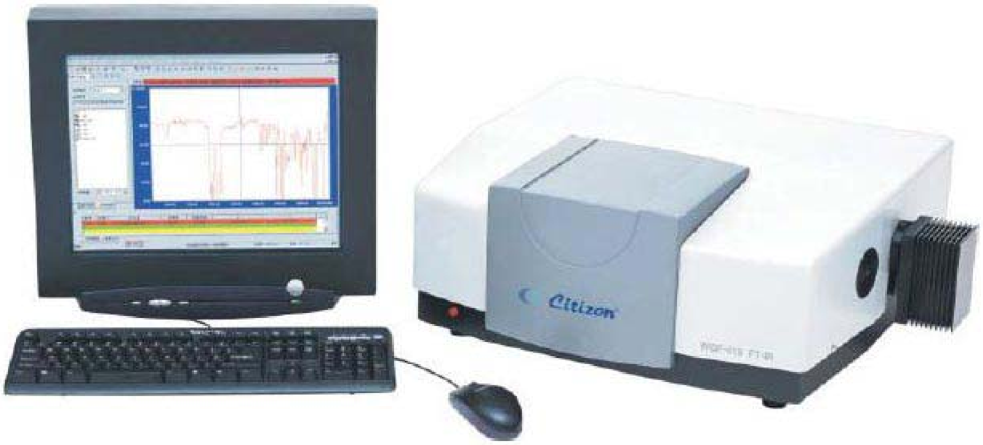

Figure 1.5: An FTIR spectrometer made by Citizen Scale (I) Pvt. Ltd. company [25]. This spectrometer operates in the range of $7800cm^{-1} - 350cm^{-1}$ with resolution better than $1cm^{-1}$.

Let's assume a monochromatic incident beam in general form as $\vec{E} = 2E_0 cos(\omega t+\phi)$ which after the beam splitter splits into two different beams, $\vec{E_1} = E_0 cos(\omega t + \phi)$ and $\vec{E_2} = E_0 cos(\omega t + \phi)$. The reflected light from the mirrors experience different phase changes. Therefore, through the detector the fields can be written as $\vec{E_1} = E_0 cos(\omega t + 2k_0 x_1 + \phi)$ and $\vec{E_2} = E_0 cos(\omega t + 2k_0 x_2 + \phi)$, where k_0 and ϕ are the incident wave number and a random phase respectively. The recorded intensity on the interferometer can be calculated as follows (the distance of the detector from the beam splitter (L) is ignored as it does not affect the final result):

$$\begin{aligned} I = {} & < E.E^* >= |\vec{E_1} + \vec{E_2}|^2 \\ & =(E_0 cos(\omega t + 2k_0 x_2 + \phi) + E_0 cos(\omega t + 2k_0 x_1 + \phi))^2 \\ & =E_0^2[cos^2(\omega t + 2k_0 x_2 + \phi) + cos^2(\omega t + 2k_0 x_1 + \phi)+ \\ & \quad 2cos(\omega t + 2k_0 x_2 + \phi) cos(\omega t + 2k_0 x_1 + \phi)] \\ & =E_0^2[\frac{1 + cos2(\omega t + 2k_0 x_2 + \phi)}{2} + \frac{1 + cos2(\omega t + 2k_0 x_1 + \phi)}{2} + \\ & \quad cos(\omega t + \phi + k_0 x_1 + k x_2) + cos(k_0 x_1 - k_0 x_2)] \end{aligned} \tag{1.1}$$

Since, the integration in time domain occurs on the detector, and $\int_{-\infty}^{+\infty} cos(\omega t) dt = 0$, the Eq. 1.1 becomes as follows:

$$I(\Delta) = E_0^2[1 + cos(k_0 \Delta)], \qquad \Delta = x_1 - x_2 \tag{1.2}$$

For a broadband light source the Eq. 1.2 becomes as follows:

$$\begin{aligned} I(\Delta) &= \int I(k)[1 + cos(k\Delta)]dk \\ &= DC + \int I_0(k) cos(k\Delta) dk \end{aligned} \tag{1.3}$$

As it is clear from Eq. 1.3, the recorded intensity composed of a DC part and a modulated part which is called as interferogram. In order to calculate the $I(k)$ from the $I(\Delta)$ we can do as follows:

$$I(k) = \int I(\Delta) e^{-jk\Delta} d\Delta \tag{1.4}$$

Where Eq. 1.4 is in fact the Fourier transform function. The ideal case would be a *PLD* (Δ) from zero to infinity which means the moving mirror must move up to infinite, which is impossible. Therefore, for a limited *PLD*, to say, $\Delta = T$, since it is multiplied with a rectangular function of width T, the resolution of the system reduces to $\frac{1}{T}$. The bigger the T, the better the resolution, hence the resolution of the spectrometer is determined by Δ. Another important fact that should be considered is that, in practice continuous scanning (or continuous data recording) is not possible, so we have to record the interferogram at steps. The length of the step (2δ) is defined based on the shortest wavelength (or the largest frequency) due to Nyquist's sampling rate. According to Nyquist's sampling rate, a signal can be sampled with a frequency larger than the twice of the highest frequency in the signal. For instance, in order to recover a signal of above $400\,nm$ region we must sample this signal with steps below $200\,nm$ which means $\delta = 100\,nm$ or smaller.

1.3 How Does a Static Fourier Transform Spectrometer Work?

1.3.1 Generic Form of a Static-FTS

A generic form of a static-FTIR is shown in Fig. 1.6 in which an incident beam splits into two beams reflected by a flat mirror and a staircase mirror. A linear CCD array collects the interfered beams which contain the multiple *PLDs* originated from the staircase mirror; every pixel (or group of pixels) records a discrete *PLD*. Let's assume the light of frequency υ_0 is shed on the beam splitter. The transmitted beam 1' and reflected beam 1 travel distance $(d_1 + L_{BS})$ and are reflected from the staircase mirror and the flat mirror respectively. The first pixel of the CCD will record their interference, and since they have traveled same optical path length $(2 \times (d_1 + L_{BS}) + L)$, their *PLD* is zero. It means that the first pixel of the CCD records the interference with minimum *PLDs*. If we consider the similar approach to the reflected beam 3 and the transmitted beam 3', since beam 3 travels optical path length $(2 \times d_1 + L_{BS} + L)$ and beam 3' travels optical path length $(2 \times (d_1 + d_2) + L_{BS} + L)$, the *PLD* of 3 and 3' is $2 \times d_2 = 2n\delta$ which is the maximum *PLD*. The last pixel of the CCD records the interference of beams 3

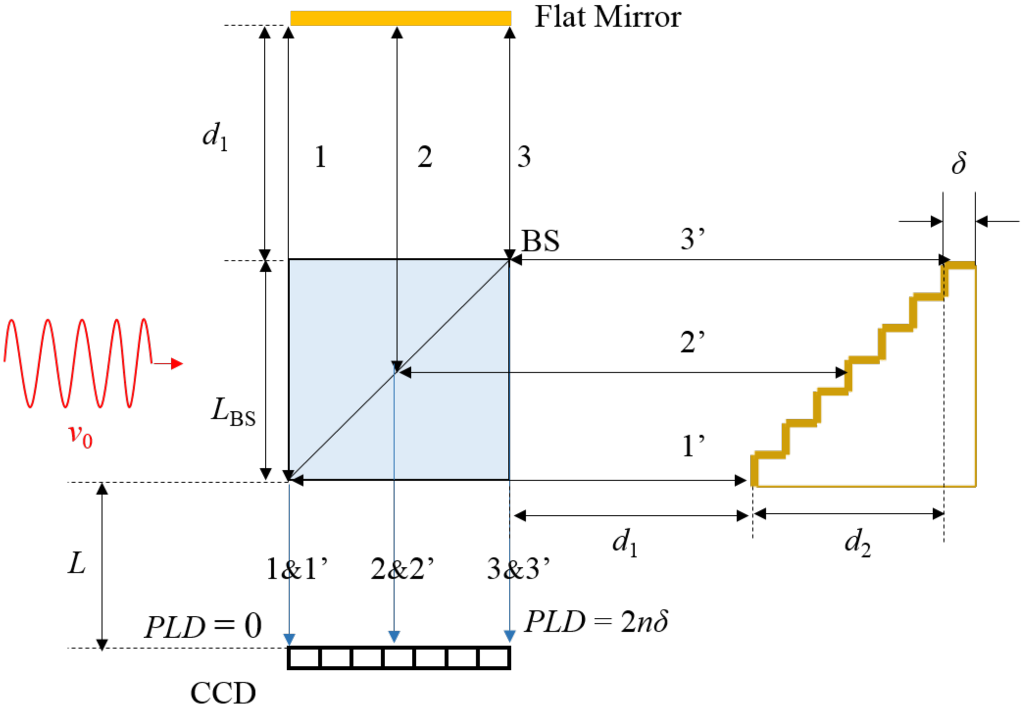

Figure 1.6: A generic static Fourier transform spectrometer cross sectional view. Beams 1 and 1' which are reflected from the flat mirror and the stair case mirror, interfere on the 1-D CCD. Total PLD is $2d_2 = 2n\delta$.

and 3'. We can conclude that each pixel of the CCD records the beams interference with different $PLDs$ ranges from ($PLD = 0$) to ($PLD = 2d_2 = 2n\delta$). As a simple example if we assume the incident light has frequency υ_0, the recorded interferogram is as Fig. 1.7a. Taking Fourier transform of the recorded interferogram, the spectrum of the input light becomes as Fig. 1.7b.

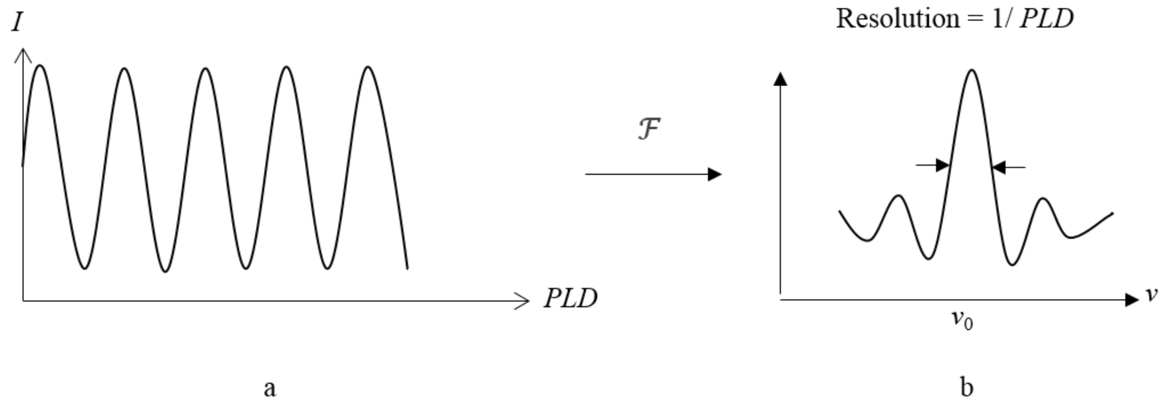

Figure 1.7: a)The recorded interferogram of an input signal of frequency υ_0, b) The spectrum of the input signal. The resolution of the spectrum is determined as $\frac{1}{PLD}$.

In the staircase mirror, the stair depth (δ) determines the sampling step size, hence, the overall PLD obtained in this configuration is $2n\delta$, where n is the number of stairs. Therefore, the spectral resolution of the system is ($resolution = \frac{1}{PLD} = \frac{1}{2n\delta}$). For a traditional spectrometer that should operate for instance between $400\,nm - 1100\,nm$, considering a staircase mirror with n as high as 4096 stairs (each stair is allocated to a pixel on the CCD), this system would produce $12\,cm^{-1}$ resolution. For this system, according to Nyquist's sampling rate (see the next chapter) the maximum δ must be below $100\,nm$.

1.3.2 A Simple Configuration for Static-FTS

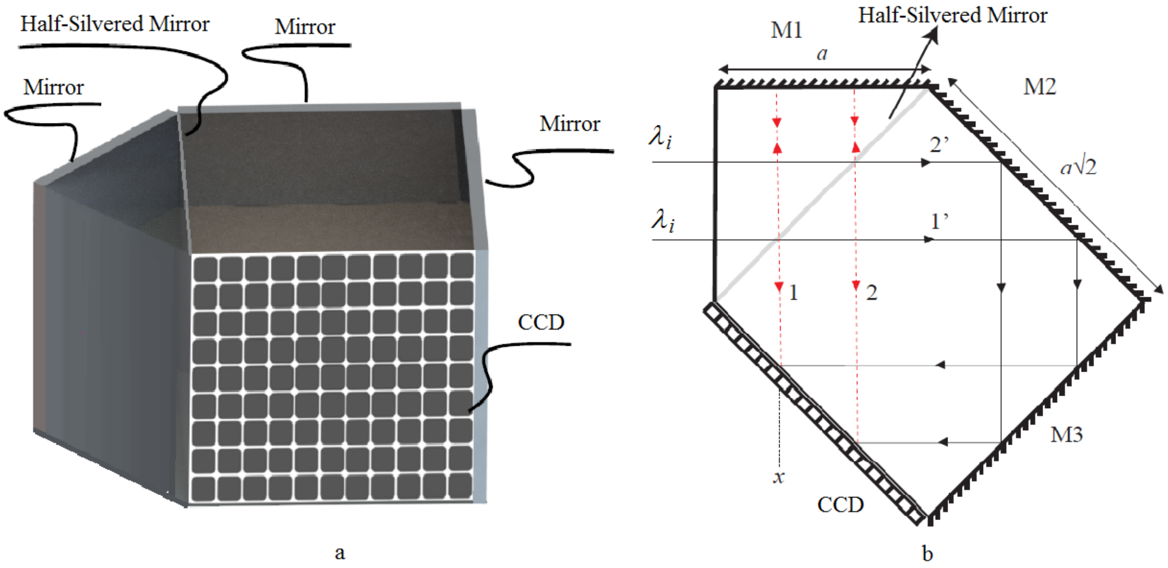

Figure 1.8: Proposed configuration for static Fourier transform spectroscopy a) 3-D configuration, b) 2-D configuration (top view). Flat mirrors are created by coating the sides of a prism and a quartz cube.

The proposed configuration for a simple and compact static-FTS is constructed by attaching a glass cube and a prism together as shown in figures Fig. 1.8 [26]. Mirrors 1, 2 and 3 (M1, M2 and M3) with unit reflection coefficients are created by coating the upper side of the prism and two sides of the glass cube respectively. In order to realize the beam splitter properties, a half-silvered mirror is used like as illustrated in Fig. 1.8b. Finally, a CCD camera is attached to the glass cube such that the split beams on the half-silvered mirror (such as 1 and 1') hit the same pixel on the CCD and yield different optical path length difference (PLD).

Lets assume a beam centered in λ_i hits the half-silvered mirror in which the reflected and transmitted beams experience path lengths 1 and 1' respectively. The optical path PLD of arms 1 and 1' is $2 \times (a - x)$ which is in the range of 0 and $2a$ (x is the point at which the beam splits into two different paths). When PLD = 0, the beams are in phase yielding constructive interference and when it is $\frac{\lambda}{2}$, they are in phases opposition and interfere destructively. Therefore, each pixel in CCD records the beams which experience different optical PLD.

The biggest problem of the proposed configuration is the CCD pixel size as the created PLD is related to the pixel width. Considering the CCD pixel width as Δ (for instance $2\,\mu m$), the minimum detectable wavelength is $2\sqrt{2}\Delta$ ($5.6\,\mu m$), according to Nyquist's sampling rate.

1.3.3 Static Single-mirror Fourier Transform Spectrometer

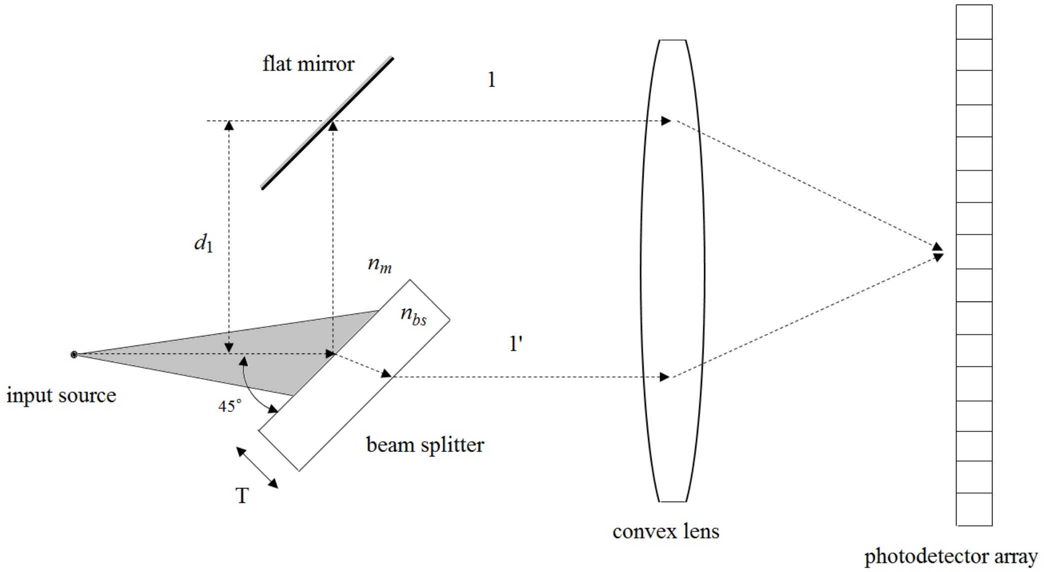

Figure 1.9: Static single-mirror Fourier transform spectrometer. A flat mirror, a beam splitter and a convex lens are used to create different PLDs on the photodetector array plane.

In reference [22], a static-FTIR is proposed which this spectrometer works in mid-infrared region between $7.2\,\mu m$ and $16\,\mu m$ with resolution $8\,cm^{-1}$. A single mirror with a beam splitter and a convex lens are used to create different PLDs as shown in Fig. 1.9. The incident light is split into two arms (1 and 1') by a beam splitter of thickness T.

The transmitted beam travels path 1' while the reflected beam travels the path 1. The reflected beam from the beam splitter experiences another reflection on the flat mirror. A convex lens is used to focus both beams (transmitted (1') and reflected (1)) on its focal plane. A detector array is positioned on the focal plane of the convex lens to record the interferogram.

Since the beam splitter has a different refractive index compared to its surrounding medium, the incident beams with different angles travel different paths and create different PLDs. An important to adjust here is the distance (d_1) between the flat mirror and the beam splitter such that the optical length of arm 1 and 1' are equal. This causes recording a centered interferogram on the photodetector array. Controlling the d_1, one can shift the interferogram upside or downside.

Chapter 2

Bandpass Sampling

2.1 Band-Pass Sampling Theorem

For each analogue signal an appropriate sampling frequency is determined according to Nyquist's sampling theorem. According to this theorem, the minimum sampling frequency is twice the highest frequency in the signal which means under this condition the sampled signal can be recovered without error. Let's assume a simple signal as shown in Fig. 2.1 a. According to Nyquist's sampling theorem, the minimum sampling frequency by which this signal can be recovered without error is $2f_H$. However, since this is a band pass signal, do we have to still sample this signal at $2f_H$? In order to answer this question let's consider the sampled signal in frequency domain which is represented in 2.1 b. The Eq. 2.1 is used to calculate the sampled signal in frequency domain.

$$X_s(f) = \sum X(f \pm Nf_s) \tag{2.1}$$

In order to plot Fig. 2.1 b, the sampling frequency (f_s) is assumed much more smaller than $2f_H$.

We should note that if we had a signal like as shown inside the box in Fig. 2.1 b, the sampled signal will be still as $X_s(f)$. Therefore if we consider a band pass signal (as Fig. 2.1 a) as a low pass signal, we can sample this signal with much lower sampling frequency, and not $f_s = 2f_H$. In order to recover the original signal, after sampling we should use a band-pass filter then transfer all the frequencies to the frequencies of the original signal. The band-pass filter bandwidth is determined based on the original signal bandwidth.

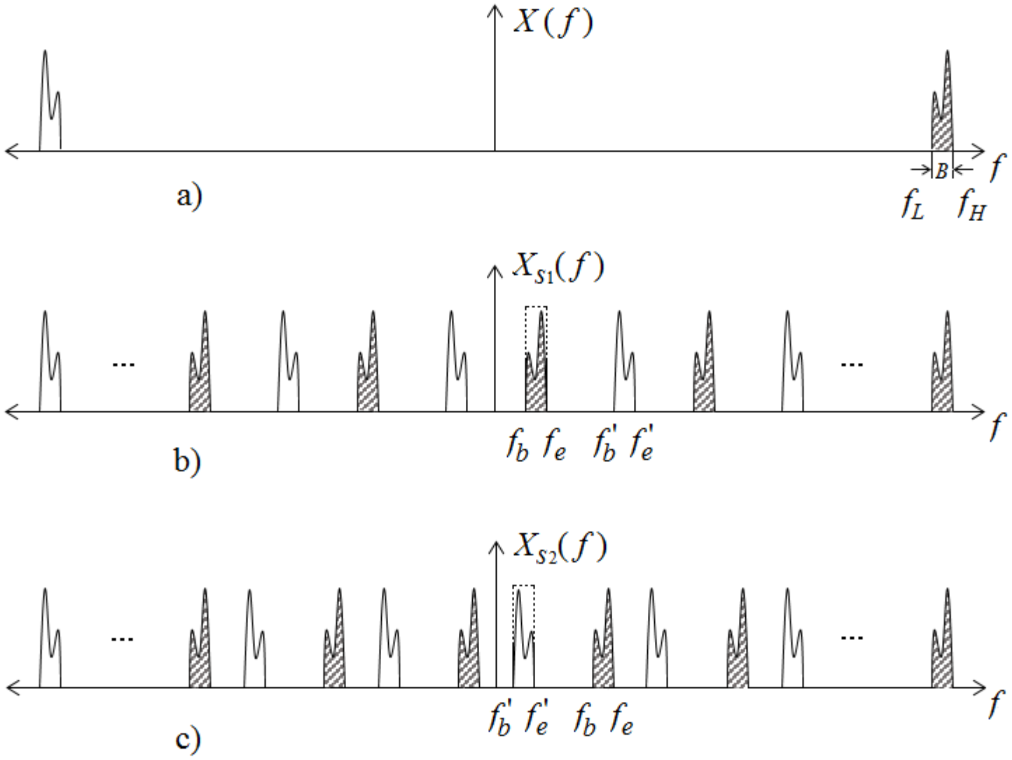

Figure 2.1: a)A general band-pass signal $X(f)$ and b) the sampled signal ($X_s(f) = \sum X(f \pm N f_{s1})$) at the sampling frequency f_{s1}, c) the sampled signal ($X_s(f) = \sum X(f \pm N f_{s2})$) at the sampling frequency f_{s2}.

In general [27], the sampling frequency for a narrow-band signal is given as:

$$\frac{2f_H}{\zeta} \leq f_s \leq \frac{2(f_H - B)}{\zeta - 1}, \qquad \zeta \leq \frac{f_H}{B} \tag{2.2}$$

where, f_H is the highest frequency in the sample, B is the bandwidth of the signal and ζ is any integer number equals to or smaller than $\frac{f_H}{B}$.
Since $f = \frac{c}{\lambda}$, we can write Eq. 2.2 in the wavelength domain as:

$$\frac{\zeta - 1}{2}\lambda_L \leq \text{scanning step} \leq \frac{\zeta}{2}\lambda_S, \;\; \zeta \leq \frac{\lambda_L}{\lambda_L - \lambda_S} \tag{2.3}$$

where, λ_S and λ_L are the shortest and the longest wavelengths in the signal respectively,

and ζ is defined as any integer number equals or smaller than $\frac{\lambda_L}{\lambda_L - \lambda_S}$.
As a conclusion for a narrow-band signal we have a rang of acceptable sampling frequency smaller than the Nyquist's sampling rate.

2.2 How to Recover a Signal Sampled with Band-pass Sampling Theorem?

In order to explain the way we can recover the original signal from the sampled signal, let's assume a simple signal as shown in Fig. 2.1 a. The sampled signals ($X_{s1}(f) = \sum X(f \pm N f_{s1})$ and $X_{s2}(f) = \sum X(f \pm N f_{s2})$) in frequency domain are represented in Fig. 2.1 b and Fig. 2.1 c. In order to recover the original signal, after sampling we should use a band-pass filter which its start and end frequencies ($f_b \& f_e$ or $f'_b \& f'_e$) are calculated as Eq. 2.4 or Eq. 2.5. The start and end frequencies should be calculated by both equations, then the smallest one is the desired band-pass filter frequencies.

$$\begin{aligned} f_b &= f_L - J f_s \\ f_e &= f_b + B \end{aligned} \tag{2.4}$$

or

$$\begin{aligned} f'_b &= -f_H + (J+1) f_s \\ f'_e &= f_b + B \end{aligned} \tag{2.5}$$

where, J is the nearest integer less than or equal to $J = \frac{f_L}{f_s}$, and f_s is the the sampling frequency. One should note that the Eq. 2.5 will be used for recovery of the signal under condition of $f_s < \frac{1}{J+0.5} f_c$ (guarantees $f'_b < f_b$), where f_c is the central frequency. Furthermore, under condition of Eq. 2.5 the recovered signal must be flipped (see Fig. 2.1 c).

As an example of band pass filter design, let's consider two different segments and show how we can design the appropriate filters. We purposely select these segments such that, in one of them we should use the result of Eq. 2.4 and in the other one the result of Eq. 2.5. Considering a signal of bandwidth range of ($400\,nm - 1100\,nm$) and dividing it into 350 segments, lets first choose segment 66 which includes wavelength range of $(530\,nm - 532\,nm)$. For this segment the calculated parameters according to Eq. 2.4 and Eq. 2.5 are as follows:

$$\left.\begin{aligned} f_b &= 3.8909 \times 10^{13} \\ f_e &= 4.1038 \times 10^{14} \\ f_b' &= 3.3962 \times 10^{13} \\ f_e' &= 3.6090 \times 10^{13} \end{aligned}\right\} \Rightarrow \quad f_b' < f_b \tag{2.6}$$

In this case since $f_b' < fb$, we must use f_b' and f_e' as the lower and upper edges of the band pass filter. Also, we have to flip the filtered signal as already mentioned.

The second case that we choose is segment 80 which includes wavelength range of $(560\,nm - 562\,nm)$. The calculated parameters for this segment is as follows:

$$\left.\begin{aligned} f_b &= 8.8078 \times 10^{12} \\ f_e &= 1.0714 \times 10^{13} \\ f_b' &= 6.4286 \times 10^{13} \\ f_e' &= 6.6192 \times 10^{13} \end{aligned}\right\} \Rightarrow \quad f_b < f_b' \tag{2.7}$$

In this case since $f_b < f_b'$, we must use f_b and f_e as the lower and upper edges of the band pass filter.

2.3 Common Acceptable Sampling Frequency

How can we sample a broad-band signal with a sampling frequency smaller than the Nyquist's sampling rate? In order to answer this question we assume a simple case in which we have only two narrow-band signals which centered at wavelengths $750\,nm$ and $950\,nm$ with $100\,nm$ bandwidth each as shown in Fig. 2.2 a. The acceptable sampling frequency regions for these two signals are calculated according to Eq. 2.3 and shown in Fig. 2.2 b. Obviously, both signals can be sampled with some common scanning steps (frequencies) which we call them as common acceptable sampling scanning steps. These common scanning steps are shown on Fig. 2.2 b with gray bars. Common acceptable scanning steps means both signal can be sampled with this scanning steps without aliasing. If we want to sample these signals at Nyquist rate, the maximum sampling step must be $350\,nm$ and $450\,nm$ for signal 1 and signal 2 respectively. However, by applying the band pass sampling theorem, these signals can be sampled with steps much larger than the Nyquist rate as shown with the solid lines in Fig. 2.2 b. Also both signal can be sampled with a common sampling scanning steps as already explained.

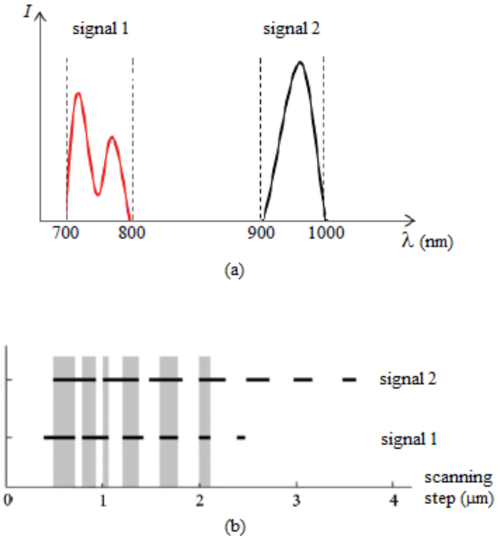

Figure 2.2: a) Simple spectrum used as an example in the text. It is composed of two separate narrow-band signals, b) Acceptable scanning step range for these narrow-band signals shown with solid lines. Gray bars demonstrate the common acceptable scanning step range for signals 1 and 2.

Now we can answer the asked question at the beginning of this section. In order to sample a broadband signal with a sampling frequency smaller than the Nyquist's sampling rate, we should divide the broadband signal into a number of narrow-band signals then calculate the common acceptable sampling frequency for these signals which, of course, will be smaller than Nyquist's sampling rate.

Chapter 3

Broadband and High Resolution Static-FTS

In this section we propose a new configuration based on bandpass sampling theorem -as explained in previous section- to solve the trade off between resolution and bandwidth and also to eliminate the need for nanometer stepsize mirrors. In order to realize this technique the input signal spectrum is separated into a number of narrow-band signals (segments), then according to what explained in previous section, we calculate the common acceptable sampling step for all the segments [28].

3.1 The Proposed Configuration for Broad-band and High Resolution Static-FTS

General form of the proposed configuration for broadband static-FTS is schematically represented in Fig. 3.1. The setup is composed of two main parts: the dispersive part and the interferometer part. In the dispersive section, the incident light is diffracted and parallelized in both x and y directions before entering the beam splitter. In this figure the x-axis is allocated to spectral segments, while the y-axis is allocated to different PLD which each segment experiences. In the interferometer section the two reflected beams from the flat and staircase mirrors interfere on a 2-D CCD as shown in the inset of Fig. 3.1.

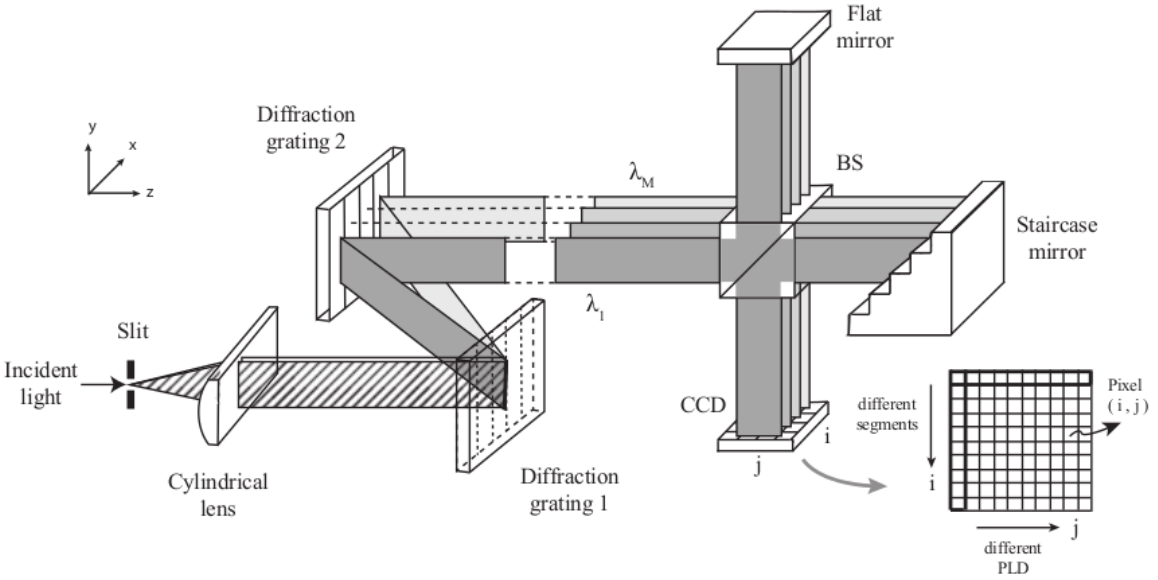

Figure 3.1: The proposed configuration for broadband static-FTS. The incident light enters from a slit and is diffracted and parallelized through the double diffraction grating structure, then it enters the beam splitter. The two reflected beams from the flat and staircase mirrors interfere on the CCD. The 2-D CCD collects on the rows i the different segments and on the columns j the different PLD. λ_1 to λ_M are the central wavelengths of the segments.

In order to better examine the proposed configuration, we assume a broadband signal in the range of $400\,nm - 1100\,nm$, then divide into M narrow-band signals. For small M, for instance $M = 100$, the segments bandwidth is large, hence, finding an acceptable common sampling step is not possible. For large M, for instance $M = 1000$, the segments bandwidth is narrow which makes the optical alignment too difficult. We found that the common acceptable sampling step occurs around $M = 350$.
Considering $M = 350$, and bandwidth of $(400\,nm - 1100\,nm)$, the acceptable scanning steps for each segment are shown in Fig. 3.2. At $M = 350$, we can use $4\,\mu m$ (or even other scanning steps) to sample all 350 segments except segments 11, 23, 36, 50, 67, 86, 108, 133, 164, 200, 244 and 300 which are shown in Fig. 3.3 . It is clear that in these segments, $4\,\mu m$ is not an acceptable scanning step.

To simulate the whole spectrum we used Halogen light as the broadband input signal and divided it into 350 segments, each of them represented by p discrete wavelengths. The intensity of the recorded interferogram on the pixel (i, j) within segment i, is given

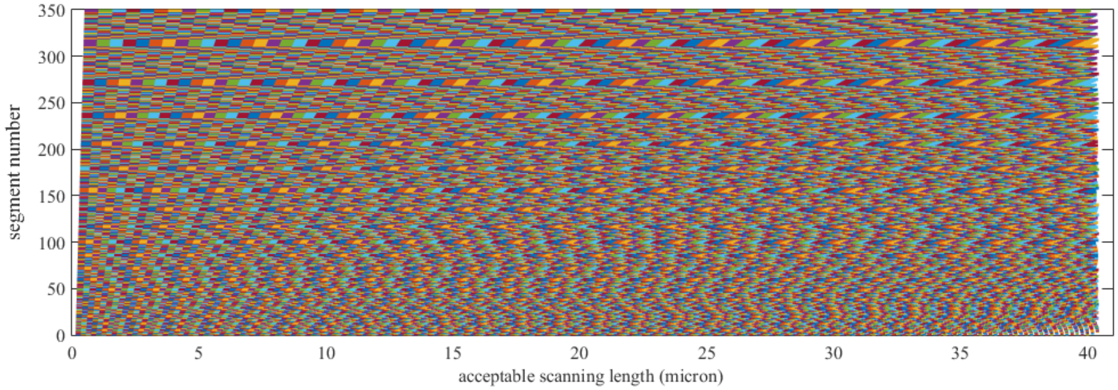

Figure 3.2: Acceptable scanning step ranges for a signal of bandwidth range of $(400\,nm - 1100\,nm)$ and segment number of 350.

as:

$$I(i,j) = \frac{1}{2} I_0(i,j)[1 + \sum_p cos(\frac{4\pi}{\lambda_i + p\Delta\lambda} j\delta + \theta_p)] \tag{3.1}$$

where, $I_0(i,j)$ is the initial intensity of the pixel (i,j), θ_p is a random phase, δ is the depth of the staircase mirrors, λ_i and $\Delta\lambda$ are the start wavelength of the segment and the wavelength step respectively, as shown in Fig. 3.4.

In order to recover the spectrum of the i^{th} segment $S_r(i)$, we calculate the Fourier transform on the pixels of the i^{th} row on the CCD.

$$S_r(i) = \mathscr{F}(I(i)) \tag{3.2}$$

The recovered spectrum is calculated by concatenating the segments' spectrum as $\sum S_r(i)$ and depicted in Fig. 3.5. The whole procedure is discussed in detail in the following sections. As it is clear from this figure, by using the proposed configuration it is possible to obtain the spectrum of a signal in the traditional spectrum range. The obtained spectrum is in good agreement with the input spectrum. The discrepancy from the original spectrum at some wavelengths occurs due to windowing function used in the FFT routines. Different windowing functions produce slightly different spectrums and the results shown in Fig. 3.5, Fig. 3.6 and Fig. 3.7 are obtained by applying the Blackman, Bartlett and Hanning windowing functions respectively.

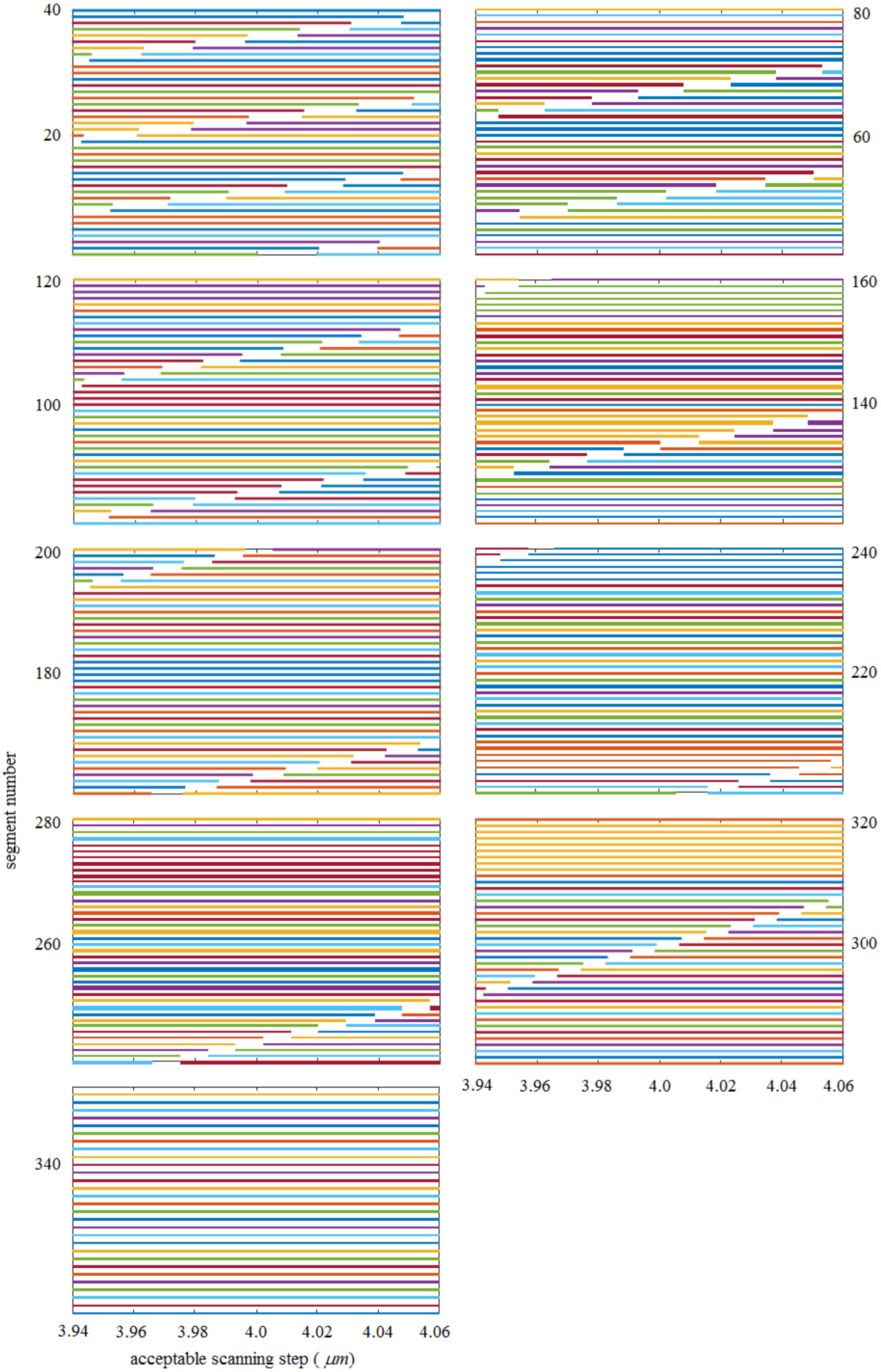

Figure 3.3: Acceptable scanning step ranges for a signal of bandwidth range of $(400\,nm - 1100\,nm)$ and segment number of 350. The Fig. 3.3 is zoomed out around $4\,\mu m$.

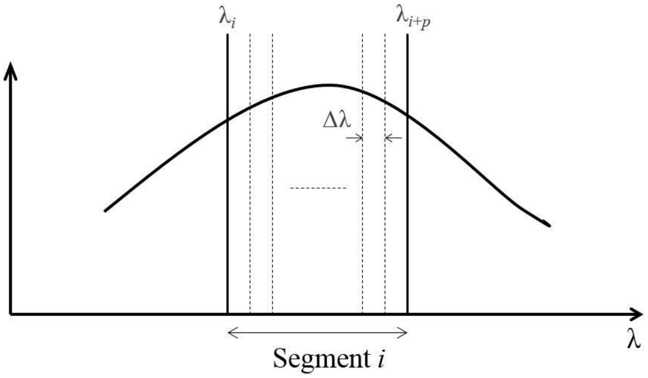

Figure 3.4: Segment analysis: each segment is discretized into p discrete wavelengths (λ) with steps $\Delta\lambda$. In this work, we have divided each segment into $p = 20$ discrete wavelengths.

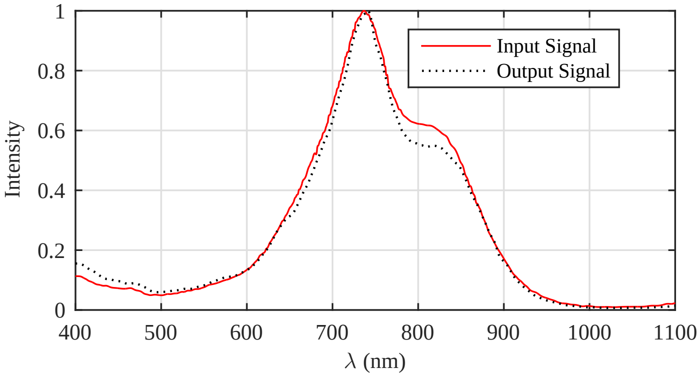

Figure 3.5: Simulation results: Halogen light spectrum as the input signal (solid line) and recovered signal by using the proposed configuration (dashed line). The number of segments and the bandwidth of each segment are 350 and $2\,nm$, respectively. The calculated common acceptable sampling step is $4\,\mu m$. We have assumed a square 4 megapixels CCD with square pixels of $4\,\mu m$ width, therefore, the overall PLD obtained by this configuration is 0.8 cm, hence the spectrometer resolution is $r = 1.2\,cm^{-1}$. The result is obtained by applying the Blackman windowing function.

3.2 Signal to Noise Ratio in the Proposed Configuration

In this section we study the signal-to-noise ratio (SNR) performance of the proposed configuration and compare it to that of the other FTIR and dispersive spectrometers [29–31]. Since in general the read-out and thermal noises are distributed uniformly on the individual channels of the spectrometer and are independent of the incident power, we consider only the shot noise for our SNR calculations.

We consider two extreme cases; signals with broadband and narrow-band spectrums. Lets assume a signal with total power P_0 and bandwidth BW which is divided into M segments as shown in the Fig. 3.8. In the case of the proposed configuration here, the shot noise power is directly proportional to the incident power on the individual

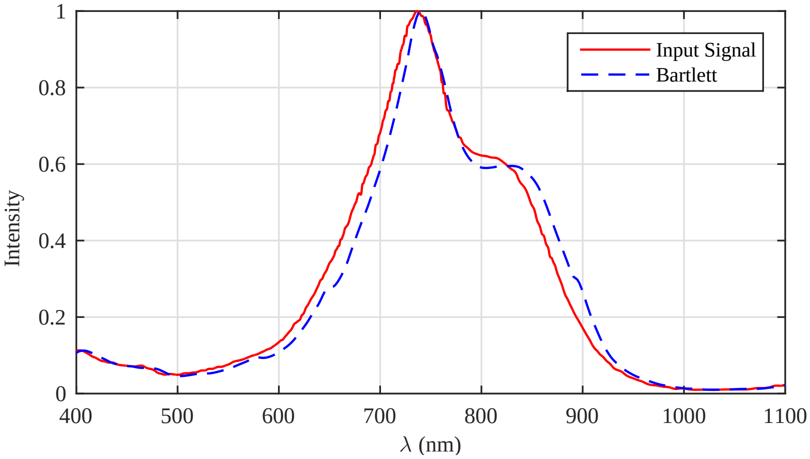

Figure 3.6: Simulation results: Halogen light spectrum as the input signal (solid line) and recovered signal by using the proposed configuration (dashed line). The number of segments and the bandwidth of each segment are 350 and 2 nm, respectively. The calculated common acceptable sampling step is 4 μm. We have assumed a square 4 megapixels CCD with square pixels of 4 μm width, therefore, the overall PLD obtained by this configuration is 0.8 cm, hence the spectrometer resolution is $r = 1.2\,cm^{-1}$. The result is obtained by applying the Bartlett windowing function.

segments since the segments are independent. Hence, for a uniform broadband signal, the SNR of a particular segment is $\sqrt{\frac{P_0}{M}}$. For a narrow-band signal (narrow band in the sense that only one segment receives signal) however, the SNR is $\sqrt{P_0}$ since the segment of interest receives whole power P_0. After determining the SNR for extreme cases, generally we can write the maximum SNR in the segments for our spectrometer as:

$$\sqrt{\frac{P_0}{M}} \leq SNR_i \leq \sqrt{P_0} \tag{3.3}$$

Now let us apply the similar approach to the traditional FTIRs where a single detector is used and assume the same number of segments are used to evaluate the spectrum as in our spectrometer. After detection a Fourier transform is performed, and since the noise in the segments adds incoherently, each segment will have a shot noise of power $\sqrt{\frac{P_0}{M}}$. For a uniform broadband signal, each segment receives power $\frac{P_0}{M}$, hence, the SNR of segment of interest is $\sqrt{\frac{P_0}{M}}$. For the narrow-band signals however, the SNR becomes $\sqrt{MP_0}$. In this case SNR is higher by a factor of $\sqrt{M}$ simply because all the segment share the noise but only single segment receives the signal. Therefore, if we generalize the situation for any signal we can write the maximum SNR in the segments

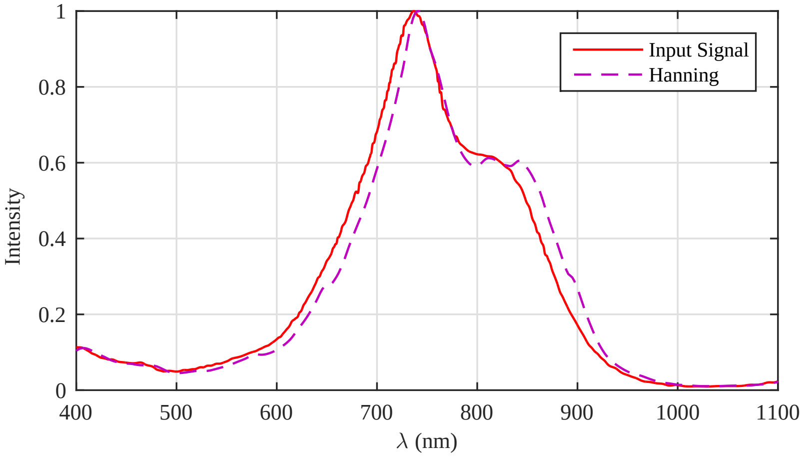

Figure 3.7: Simulation results: Halogen light spectrum as the input signal (solid line) and recovered signal by using the proposed configuration (dashed line). The number of segments and the bandwidth of each segment are 350 and 2 nm, respectively. The calculated common acceptable sampling step is 4 μm. We have assumed a square 4 megapixels CCD with square pixels of 4 μm width, therefore, the overall PLD obtained by this configuration is 0.8 cm, hence the spectrometer resolution is $r = 1.2\,cm^{-1}$. The result is obtained by applying the Hanning windowing function.

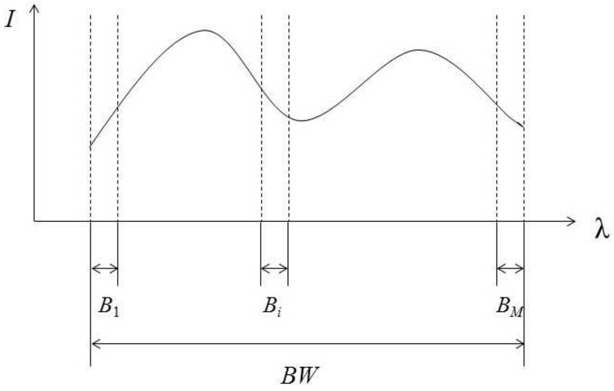

Figure 3.8: A broadband spectrum of bandwidth BW divided into M spectrums (channel) of similar bandwidth $\frac{BW}{M}$. Shot noise in each channel equals to the square root of channel power.

for traditional FTIR as follows:

$$\sqrt{\frac{P_0}{M}} \leq SNR_i \leq \sqrt{MP_0} \tag{3.4}$$

Comparing the calculated SNR for the traditional FTIRs and our proposed configuration (i.e. Eq. 3.3 and Eq. 3.4), we can conclude that in the broadband signal case our proposed configuration and the traditional FTIRs show a similar SNR performance but for the narrow-band signals the traditional FTIRs show $\sqrt{M}$ times better SNR performance.

As far as the dispersive spectrometers with CCD arrays are concerned from the CCD point of view the *SNR* performance of our spectrometer is same as the dispersive spectrometers since each segment is detected independently.

3.3 Error Analysis in the Proposed Configuration

In this section the error sources as well as their effect on the recovered signals are analyzed. In the proposed configuration, two different source of errors are predictable; first, the error that originates from double diffraction grating due to any offset from parallelism (see Fig.3.10) and the second one is due to any error in the depth of the staircase mirror (δ). The effect of offset from parallelism is shown in Fig. 3.9. When the diffraction gratings are perfectly parallel in the double diffraction grating structure, the diffracted beams from the second grating are parallel and they hit the desired pixel on the CCD as illustrated in Fig. 3.9 a. However, any offset from the parallelism causes a leakage between the adjacent channels as illustrated in Fig. 3.9 b and Fig. 3.9 c.

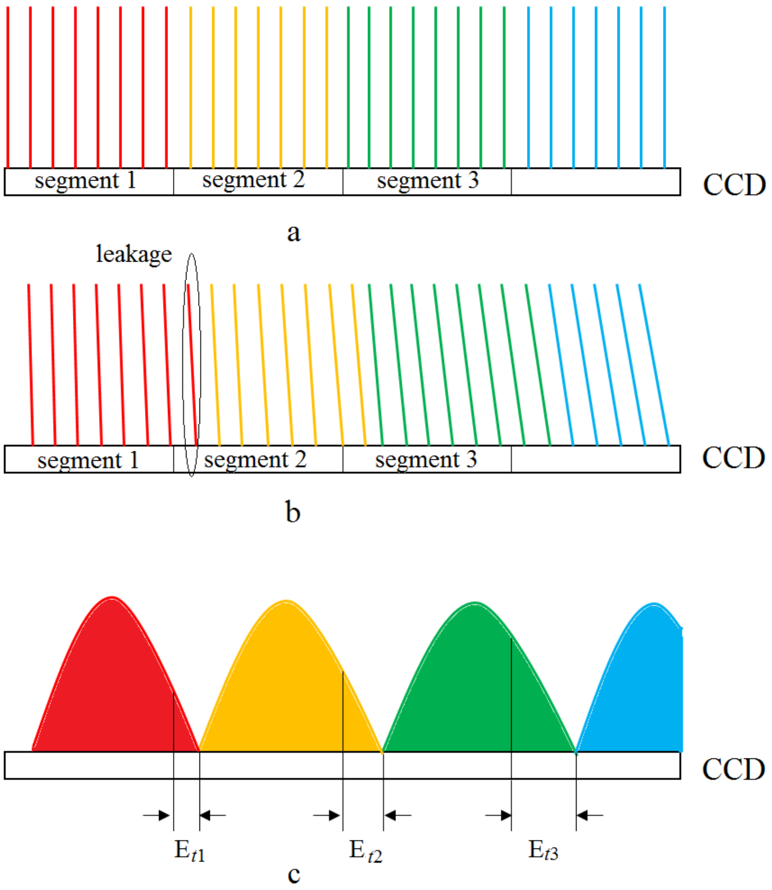

Figure 3.9: The effect of offset angle, a) The gratings are parallel, b) The gratings are not parallel which some of the beams from segment 1 falls on the segment 2, c) The energy leakage between the adjacent segments.

The effect of offset from parallelism is investigated according to general equation of diffraction gratings. Considering the ray diagram in Fig. 3.10 we have:

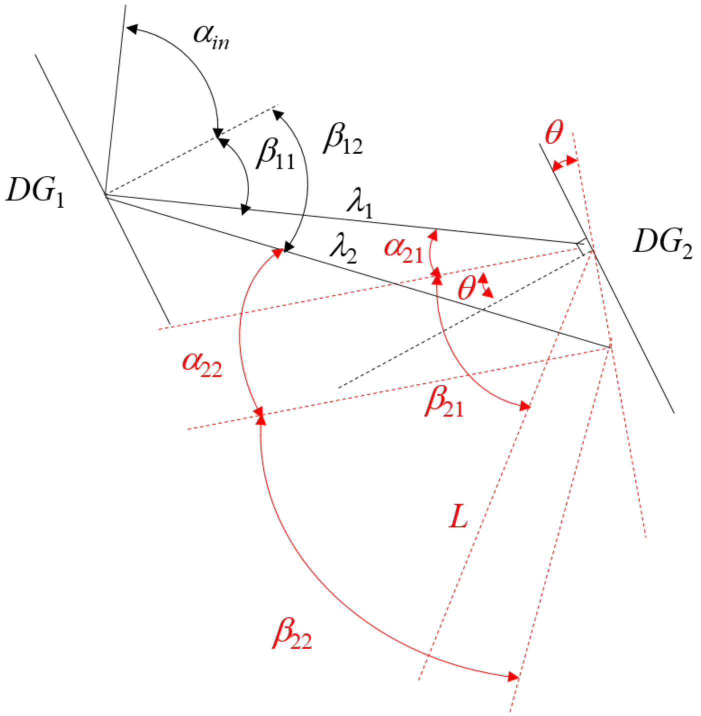

Figure 3.10: Ray diagram on a double diffraction grating configuration with offset angle θ. λ_1 and λ_2 are the edge wavelengths of the first and the second segments.

$$\begin{aligned}\beta_{21} &= \sin^{-1}(\frac{p\lambda_1}{d} - \sin(\beta_{11} - \theta)) \\ \beta_{22} &= \sin^{-1}(\frac{p\lambda_2}{d} - \sin(\beta_{12} - \theta))\end{aligned} \tag{3.5}$$

where, the angles are indicated on Fig. 3.10.

At a distance L the created error on the second segment (due to nonparallel beams) $E1$ is $E1 = L \times \tan(\beta_{21} - \beta_{22})$.

For $\alpha_{in} = 35°$, $m = 1$, $d = 1mm/600$, $L = 30\,cm$, $\lambda_1 = 400\,nm$ and $\lambda_2 = 402\,nm$ the created error versus offset angle (θ) is calculated according to Eq. 3.5 and is shown in Fig. 3.11. We have represented Fig. 3.11 right, only to to show that at small angles the error versus offset angle is linear. As it is clear from this figure, at $0.5°$ we have almost $1\,\mu m$ error which means the energy of this part leaks to the second segment.

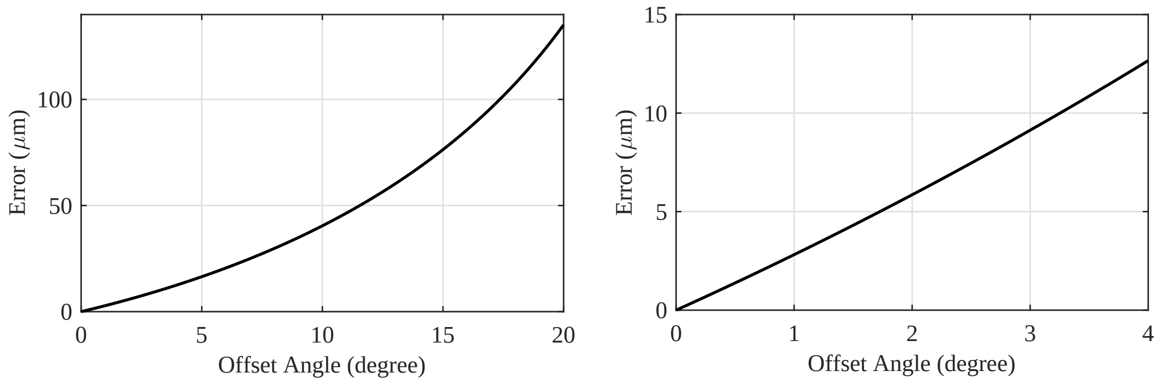

Figure 3.11: a)Created error on the second segment (due to nonparallel beams) in spatial domain versus offset angle, b) The error versus offset angle is plotted to show its linear behavior in small offset angles.

The important to not here is that, since the bandwidth of a segment is $2\,nm$, it occupies almost $96\,\mu m$ on the CCD which the total offset error on the second segment is about a percent ($\frac{1\mu m}{96\mu m} \approx 1\%$). This is why dividing to less number of segments is useful. Nowadays, 3-D printers are used to manufacture the required mounts for parallel diffraction gratings. Therefore, the offset error will be negligible since due to high precision 3-D printers it will be in the order of a few milli degree.

Since the offset error comes from the non-parallelism effect of the diffraction gratings, the error of the i^{th} segment is sum of the all errors of the previous segments plus the error created due to non-parallelism effect between the λ_i and λ_{i+1}. This error can be calculated according to Eq. 3.5 simply by substituting λ_1 and λ_2 by λ_i and λ_{i+1} respectively. We can formulate the total error (E_{ti}) on the i^{th} segment as follows:

$$E_{ti} = \sum_{1}^{i} E_n \tag{3.6}$$

Another error source in the proposed configuration (generally in all static-FTS) is the error in the depth of the stairs. In the simulation we have assumed $\delta = 2\,\mu m$, but in practice, fabrication of a staircase mirror with all steps as $2\,\mu m$ is almost impossible. Therefore, we assumed a uniform random error in each step and simulated the proposed configuration considering this error. The results are shown in Fig. 3.12. The error values on each step with maximum 5% and 10% are represented in Fig. 3.12 (bottom-left) and Fig. 3.12 (bottom-right) respectively. For instance, maximum 5% error means the depth

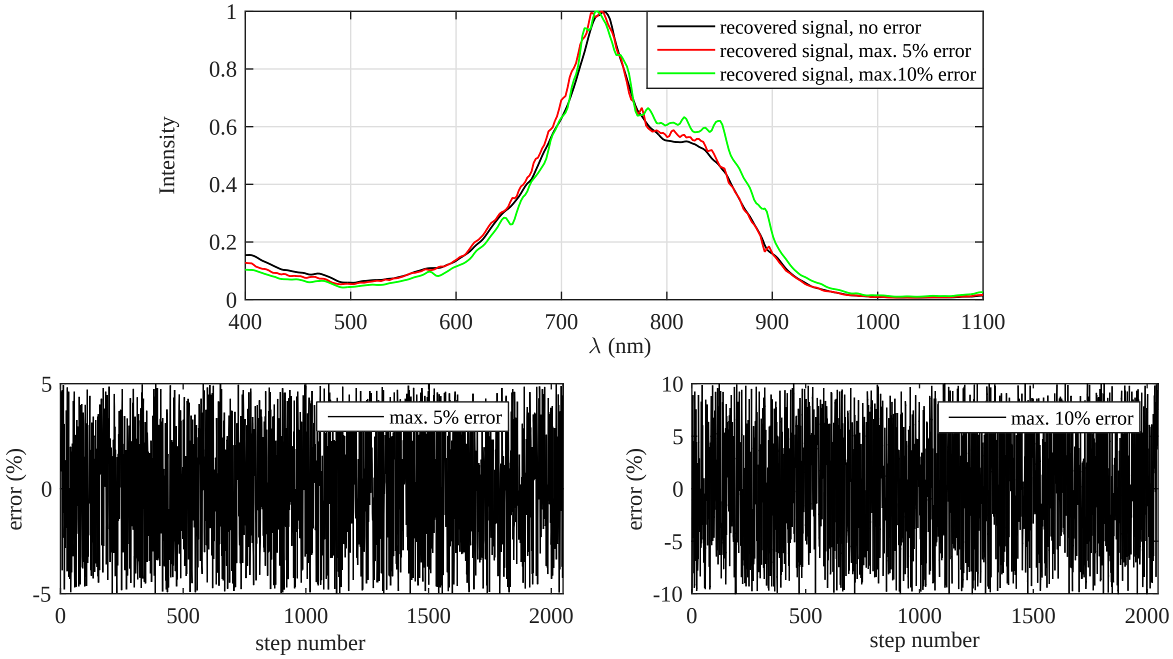

Figure 3.12: The recovered signal with maximum 5% and 10% errors (top), the error value on each staircase mirror step with maximum 5% (bottom-left), the error value on each staircase mirror step with maximum 5% (bottom-right).

of the steps is in the range of $1.9\,\mu m - 2.1\,\mu m$. As it is clear from this figure, increasing the error ratio, discrepancy from the input signal gets larger.

3.4 Advantages and Disadvantages of the Proposed Configuration

A legitimate question would be if there is any advantages of the proposed system over a dispersive spectrometer or not as we divide the spectrum also into the segments.
The resolution in a dispersive spectrometer is directly proportional to the number of pixels in the CCD, while in our proposed configuration it is proportional to the number of pixels in the CCD and also the depth of the stairs. For a dispersive spectrometer with a CCD of n pixels wide, the resolution is proportional to $r_{dis} = \frac{k_1 - k_n}{n}$, where k_1 and k_n are the first and the last wavenumbers of the recorded spectrum respectively. However, for our proposed spectrometer the resolution is proportional to $r = \frac{1}{2n\delta}$ as previously stated. For instance, with a 4 megapixels square CCD and a spectrum range of $(400\,nm - 1100\,nm)$, a dispersive spectrometer would have an average resolution of $8\,cm^{-1}$, while for our proposed configuration the resolution is calculated as $1.2\,cm^{-1}$, which is almost 7 times better.

The advantages of the proposed configuration and prototyped device over the traditional FTSs and static-FTSs are listed below.
Actually, the static-FTSs are developed to overcome the disadvantages of the FTSs originated from the moving mechanism. Therefore, the first advantage of the proposed configuration over the FTSs is that there is no moving part in the in-built device.
While the existing static-FTS's perform in a narrow band regime, the proposed configuration for the static-FTS makes it a broad band device which is due to dividing the input signal into narrow band signals.
The prototyped static-FTS works in visible range as well as in a wide band, while the existing FTSs have to operate either at longer wavelengths or in a narrow band region.
A diffraction grating in Littrow configuration is used to realize the staircase mirror which diminishes the cost of the prototyped spectrometer since it is possible to use off-shelf diffraction gratings.
The disadvantages of the prototyped device over the FTSs are: 1. Low throughput due to entrance pinhole, 2. The internal calibration is missing since we have not used any

reference beam.

In a nutshell, the proposed technique is implemented by combining a static-FTS and dispersive elements to make a broadband and high resolution spectrometer. Therefore, it will carry both advantages and disadvantages of either part. The broadband advantage is due to the dispersive parts, while the high speed and high resolution advantages come from the FTIR part. Low throughput disadvantage appears due to the entrance pinhole that we use, although all the FTIRs require an aperture to control the convergence of the beam in the interferometer. The internal calibration capability of the FTIRs is not available here, since we have omitted the reference beam. The total cost of the device is reduced due to off-shelf diffraction grating that we used in Littrow Configuration to realize staircase mirror properties.

Chapter 4

Experimental Evaluation of the Broad-Band and High Resolution Static-FTS

4.1 Design Procedure

Experimental configuration is composed of two integral parts: dispersive part and static-FTS part. The first one includes a double diffraction grating structure to disperse the input spectrum in horizontal direction such that each column of the CCD will receive a narrow band of the spectrum, and the second one is a static Michelson interferometer to make different PLDs in the vertical direction as illustrated in Fig. 4.1.

4.1.1 Dispersive Part

First of all, a parabolic mirror is required to collimate the incident beams on the diffraction grating. Since, only the incident beams from the focal point of a parabolic mirror reflect and collimate, a pinhole must be located at the focal point of the parabolic mirror. Otherwise, the reflected beams cross at some points (see Fig. 4.2). After the entrance pinhole, light is reflected from a parabolic mirror to a pair of grating. First diffraction grating receives the light as a vertical strip and disperses horizontally as a

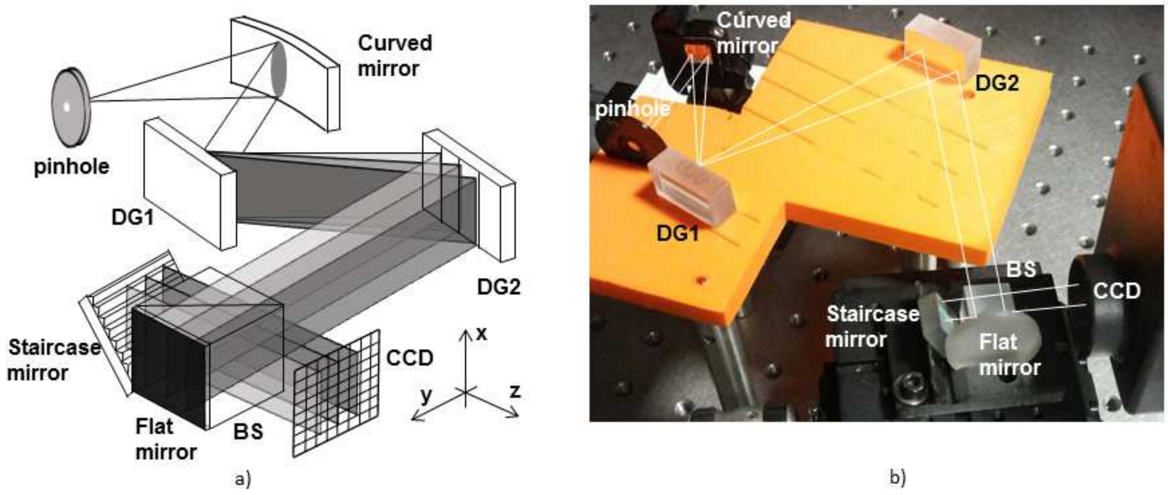

Figure 4.1: a) A drawing of the proposed static-FTS. At the entrance, a 5 μm pinhole before a concave mirror of 50 mm focal length is used. Two diffraction gratings (DG) of 600 Grooves/mm spreads the beam in wavelength in horizontal direction before a Michelson interferometer composed of a 0.5 $inch$ cube beam splitter, a flat mirror and a diffraction grating with 1200 grooves/mm. This diffraction grating is used in Littrow configuration to realize the stair-case mirror. b) An actual photo of the experimental setup.

function of wavelength and the second diffraction grating collimates the beam in horizontal (y direction).

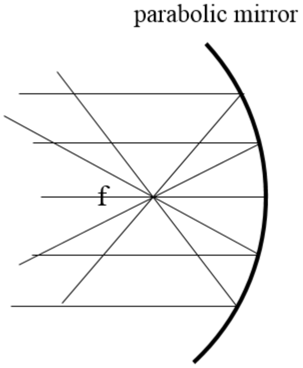

Figure 4.2: Ray diagram for a parabolic mirror.

The distance between the grating pair is adjusted considering the following facts:

- The reflected and diffracted beams from the second diffraction grating (DG2) do not hit the first diffraction grating (DG1). This item depends on the incident beam width and angles as well as the diffraction grating length, angle and groove spacing.

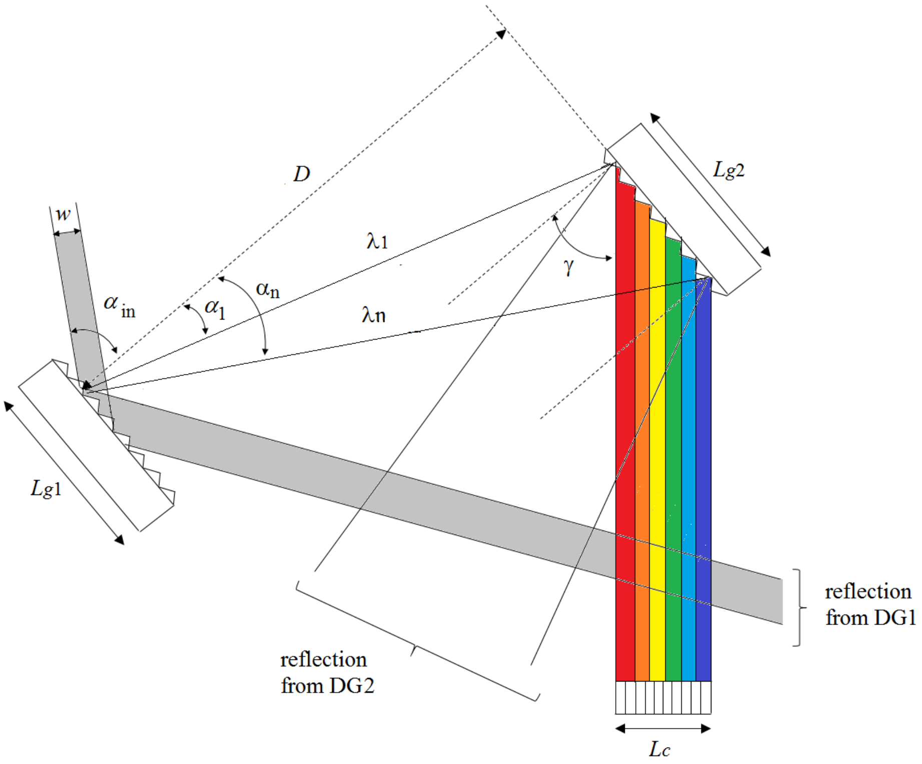

Figure 4.3: Schematic representation of ray diagram in double diffraction grating.

- CCD length in horizontal direction such that the spectrometer works at the maximum bandwidth.

The reflected and diffracted beams from double diffraction gratings are schematically represented in Fig. 4.3. As it is clear from this figure, the CCD length in horizontal direction determines the distance between diffraction gratings.

Considering the diffraction gratings general equation as $p\lambda_1 = d(\sin\alpha_{in} + \sin\alpha_1)$ and $p\lambda_n = d(\sin\alpha_{in} + \sin\alpha_n)$ for the first and the last wavelengths (λ_1 and λ_n) respectively, we can calculate the distance between diffraction gratings (D) with respect to CCD length (L_c) as follows:

$$\left.\begin{aligned} L_{g2} &= D(\tan\alpha_1 - \tan\alpha_n) \\ L_{g2} &= \frac{L_c}{\cos\gamma} \end{aligned}\right\} \Rightarrow \quad D = \frac{L_c}{\cos\gamma(\tan\alpha_1 - \tan\alpha_n)} \tag{4.1}$$

where d is the diffraction grating period, p is the order of diffraction, and angles are as indicated on Fig. 4.3. In the design procedure, we first found the minimum distance at which the reflected or diffracted beams from the second diffraction grating do not hit the first diffraction grating. Then, using Eq. 4.1 we calculate the distance between the diffraction grating pair.

4.1.2 Effect of the Incident Angle Width

The width of the incident light affects the full width at half maximum (FWHM) of the diffracted light from the diffraction grating surface. In order to investigate this, lets assume a monochromator light such as λ_1 in Fig. 4.3. The FWHM of this monochromator light on the second diffraction grating plane depends on the incident beam width (w), wavelength and distance between the diffraction gratings. Considering the diffraction grating general equation, the FWHM is calculated as follows and schematically illustrated in Fig. 4.4. Since between two maxima (constructive interference) there are $(N-1)$ minima (destructive interference), we can write the angular distance ($\Delta\alpha$) between the maxima and the first minima at $p = 1$ as follows:

$$\Delta\alpha = \frac{\arcsin(\frac{2\lambda}{d}) - \arcsin(\frac{\lambda}{d})}{N} \tag{4.2}$$

For simplicity we assumed $\alpha_{in} = 0$. In spatial domain, FWHM can be written as:

$$\mathrm{FWHM} = \frac{1}{2} \times D(\tan(\alpha_1 + \Delta\alpha) - \tan\alpha_1) \tag{4.3}$$

For $\alpha_{in} = 0$, $D = 10\,cm$ and $d = \frac{1\,mm}{600}$ the FWHM of a green laser ($532\,nm$) versus incident beam width is plotted and shown in Fig. 4.5.

From this figure we can understand that at larger beam width, the FWHM is getting smaller, linearly. Also, in order to get narrower (smaller FWHM) diffracted signal we have to increase the incident light width.

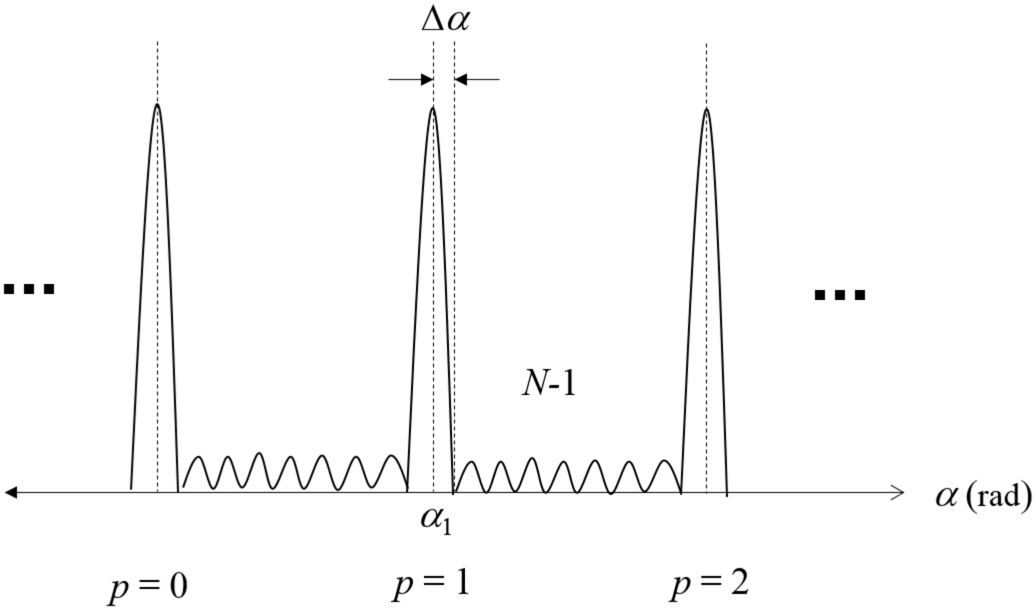

Figure 4.4: Schematically illustration of a monochromatic light diffraction at different grating orders (p).

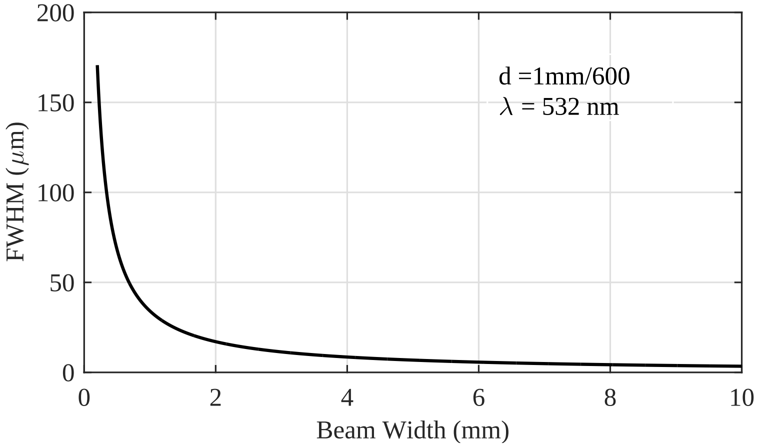

Figure 4.5: FWHM versus incident beam width for a green laser.

4.1.3 Static-FTS Part

The second part, which is composed of a beam-splitter (BS), a flat mirror and a stair-case mirror (in actual setup a diffraction grating in Littrow configuration is used), works as follows: the parallelized beams at the output of the double diffraction grating structure enter the BS, then split into two different arms; one arm is reflected from the flat mirror, and the other one is reflected from the stair-case mirror. The reflected beams from these mirrors interfere on a CCD camera which is placed on the back of

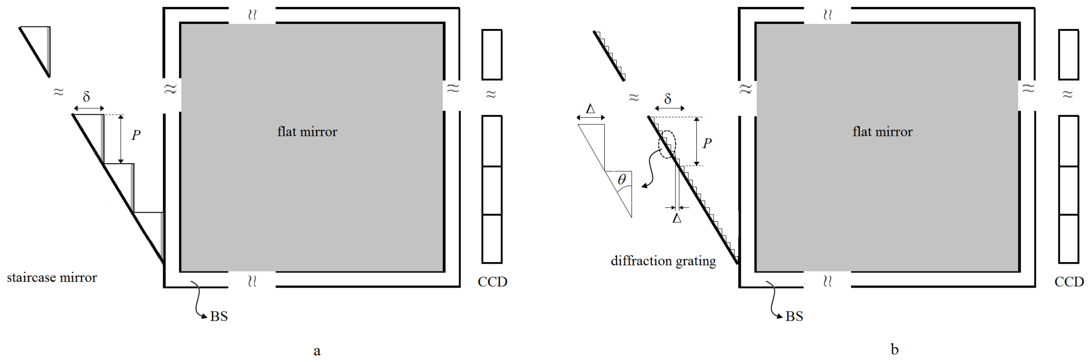

Figure 4.6: Side view of the interferometer from flat mirror side. a) Ideal experimental configuration. b) A diffraction grating with 1200 grooves/mm is used in Littrow configuration to realize staircase mirror with $\theta = 26.4°$ and $\delta = 7\Delta = 2.6\mu m$.

the BS as depicted in Fig. 4.1. The reflected light experiences different PLDs due to stair-case mirror which is realized by a diffraction grating in Littrow configuration. On the CCD, the x-direction is allocated for PLD variation, and y-direction is allocated for spectral segments (band-pass signals). In order to obtain the spectrum of a segment (lets call it $I(y)$) we must calculate the Fourier transform on the pixels of the y^{th} column on the CCD.

When the interferometer is configured with a flat mirror and a staircase mirror, the total electric field on m^{th} pixel of a segment would be as $\vec{E} = \vec{E}(k)\cos(\omega t) + \vec{E}(k)\cos(\omega t + 2mk\delta)$, where k is the wavenumber and the δ is the step size as illustrated in Fig. 4.6. Then the time averaged recorded intensity I with a distribution of wavelengths is given as:

$$I = <\vec{E}.\vec{E}^{*}> = \int A(k)[1 + \cos(2mk\delta)]dk, \tag{4.4}$$

where $A(k)$ is the spectrum of interest.

However, here we have used a diffraction grating in Littrow configuration to realize the staircase mirror since it solves the fabrication issues of the micro stair-case mirrors, and it is possible to use off the shelf diffraction gratings. This configuration is equivalent to a mirror with N sub-steps per pixel as shown in Fig. 4.6. For a staircase mirror with N sub-steps and a single wavelength, the electric field ($\vec{E}$) on the m^{th} pixel of the CCD can be calculated as:

$$\vec{E} = N\vec{E}(k)\cos(\omega t) + \sum_{i=1}^{N} \vec{E}(k)\cos(\omega t + 2mk\delta + 2ik\Delta) \tag{4.5}$$

In the experiments we used a diffraction grating with $1200\, g/mm$ and blazed angle of 26.4° which the total $N = 7$ grooves match a pixel width of the CCD. Therefore, the interferogram intensity in this case, after some algebra, is given as:

$$I(\delta) = \int A(k)[\frac{49}{2} + 2S^2 + 14\, S\ \cos(2mk\delta + 8k\Delta)]dk \tag{4.6}$$

where, $A(k)$ is the amplitude of the signal with wavenumber k and $S = 0.5 + cos(2k\Delta) + cos(4k\Delta) + cos(6k\Delta)$, δ is the stair-case mirror depth, and Δ is the depth of diffraction grating grooves as shown in Fig. 4.6. In order to calculate the $A(k)$, we calculate the Fourier transform of the recorded intensity I, then divide it by $14S$.

An important to note here is that, in the ideal case where the interferogram intensity calculated with Eq. 4.4, 50 percent of the input signal appears as a DC signal, while in our case here (Eq. 4.6) the DC value is about 75 percent. This means reduction in signal contrast or visibility in our actual experimental configuration.

4.2 Device Calibration

For a double diffraction grating structure as shown in Fig. 4.7, the relevant equations for the diffraction angles at wavelength λ_n are as follows:

$$DG_1: \qquad p\lambda_n = d(\sin\alpha_{in} + \sin\beta_n) \tag{4.7}$$

$$DG_2: \qquad p\lambda_n = d(\sin\alpha_n + \sin\gamma), \tag{4.8}$$

where d is the diffraction grating period, p is the order of diffraction, and angles are as indicated on Fig. 4.7. If the D is the distance between the grating pair, and CCD pixel dimension is P, one can write $L = \frac{P}{\cos(\gamma)}$, and $L = D \times [\tan\beta_{n+1} - \tan\beta_n]$. Then we

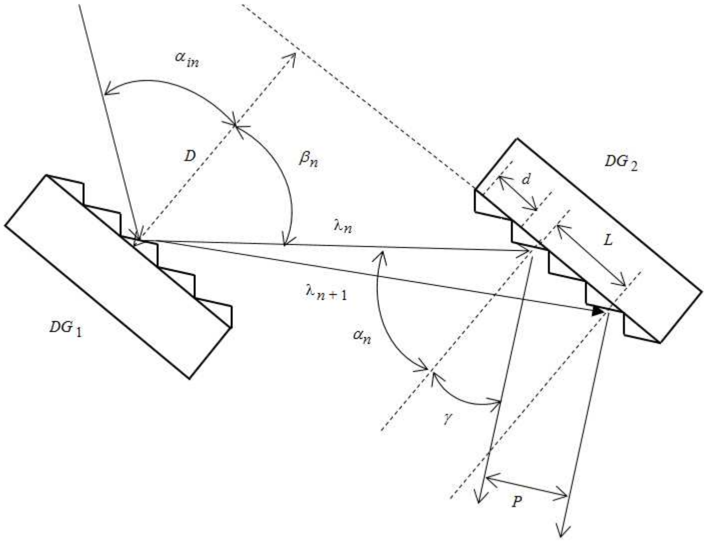

Figure 4.7: Double diffraction grating structure, in which two similar diffraction gratings are placed parallel to each other to disperse the beam in horizontal direction.

can simply calculate the wavelength λ_{n+1} that falls on the adjacent pixel:

$$\lambda_{n+1} = d \times [\sin\alpha_{in} + \sin U], \tag{4.9}$$

where $U = \tan^{-1}(\tan\beta_n + P/D\cos\gamma)$. Therefore, ignoring the inter-pixel spacing, the spectral range per pixel is $(\lambda_{n+1} - \lambda_n)$.

In conclusion, to calibrate the device, we shined a monochromator laser (for instance green laser) on the pinhole and find the pixel number on which this laser hit. We called this pixel as λ_n, then, having λ_n and the pixel that this wavelength falls on the CCD, we calculated the wavelength of the adjacent pixel (λ_{n+1}) according to Eq. 4.9.

4.3 Results and Discussions

For the proof of principle experiments, we recorded $140\,nm$ wide spectrum of signals ranging from $525\,nm$ to $665\,nm$ with a 1280×1024 pixel CCD camera. The pixel dimension of $5.25\,\mu m$ is a common acceptable sampling step for these 1280 narrow-band signals (calculated with Eq. 2.3) except the three segments. For this particular example, the segments 253, 534 and 848 violate the BPS theorem, therefore for those segments the resolution will be limited to the resolution of the dispersive section/dimension. It is important to note here again that, when this spectrum range has to be recorded with a traditional static-FTS, the sampling steps must be smaller than $262\,nm$ (stair depth of $132\,nm$) due to Nyquist's sampling theory.

The unique configuration of our proposed spectrometer actually allows the resolution and bandwidth selection independently. The delay part determines the pixel resolution and the number of segments determine the overall bandwidth of the spectrometer. The device bandwidth is limited by the CCD array width for a given dispersion from the grating pair, here in our case the width of $6.65\,mm$ provides $140\,nm$ bandwidth. The maximum delay is $2N_x\delta$ where N_x is the number of CCD pixels in the delay direction (vertical direction in here) and δ is the depth of stair-cases as shown in Fig. 4.6. Therefore the pixel resolution is limited to the inverse of this delay, and for the setup presented $(1/5.32\,mm) = 1.9\,cm^{-1}$ is the pixel resolution.

In order to calculate the spectrum of input signal from the recorded data, we used the band pass signals recovery method as already explained. For example, in our case, the number of data points that we obtained through a pixel in the dispersion domain (y-direction) is two data points, while in dispersive spectrometers each pixel corresponds to a single data point.

The reason for two data points in our case comes from the total PLD (which is related to CCD dimension in x-direction as well) which determines the pixel resolution of the system, and in our case the pixel resolution is two times better compared to dispersive spectrometers.

In order to increase the number of data points through a pixel and consequently the pixel resolution, we must increase the total PLD (CCD dimension in x-direction).

The two data points mean that we can resolve two wavelengths through a single pixel due to fact that the resolution in our system is defined by the created maximum PLD in x-direction.

In order to generalize the above-mentioned fact about the number of data points through a segment we assume a signal of bandwidth BW which is divided into M segments of bandwidths B_i as depicted in Fig. 4.8.

Since we calculate the FFT of individual segments, considering the facts about the Fourier transform (see Fig. 4.9) we can generalize the number of data points obtained through a segment. Assuming the sampling frequency as f_s, the distance between two adjacent data points in frequency domain is $df = \frac{f_s}{n}$, where n is the signal length (here the CCD dimension in PLD direction N_x). For each segment, we design a band pass filter of equal bandwidth to that of the related segment (B_i), therefore, the number of frequencies (data points) which takes place within the band pass filter can be calculated as follow:

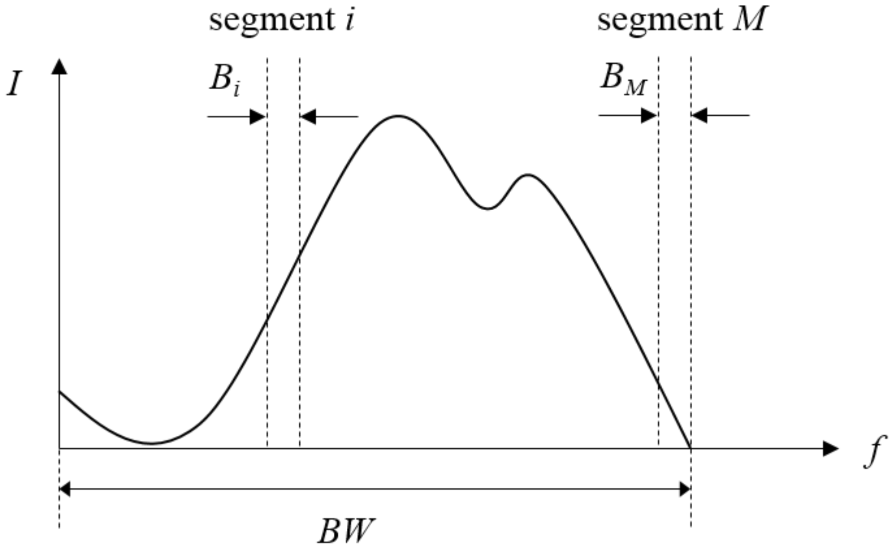

Figure 4.8: A broadband spectrum of bandwidth BW divided into M spectrums (channel) of bandwidth B_i.

$$\text{number of data points} = \lfloor \frac{B_i n}{f_s} \rfloor \tag{4.10}$$

Where$\lfloor\ \rfloor$ is the symbol of the nearest integer less than or equal to that value.

As it is clear from Eq. 4.10, the number of data points directly proportional to the CCD length ($n = N_x$).

Let's consider an example from our real data in the experiment. Since in our experiments we have used 1280 segment and recorded whole spectrum of 140 nm bandwidth, each segment has bandwidth of roughly 0.11 nm. We assume the first segment which ranges from 525 nm − 525.11 nm. The number of data points which takes place within the band pass filter is calculated as follows:

$$\left.\begin{aligned} & n = 1024 \\ & f_s = \frac{1}{\text{sampling step}} = \frac{1}{5.25\,\mu m} = 1.9 \times 10^5 \\ & B_i = \frac{1}{525\,nm} - \frac{1}{525.11\,nm} = 400\frac{1}{m} \end{aligned}\right\} \Rightarrow \text{number of data points} = \lfloor \frac{400 \times 1024}{1.9 \times 10^5} \rfloor = 2 \tag{4.11}$$

The flow chart of the signal processing on the obtained data is as follows: The FFT on each segments' data are done independently. Then a band pass filter is designed for each segment according to Eq. 2.4 or Eq. 2.5. The output of the filters which belong to the individual segments, are concatenated. The flow chart of these functions is illustrated in Fig. 4.10.

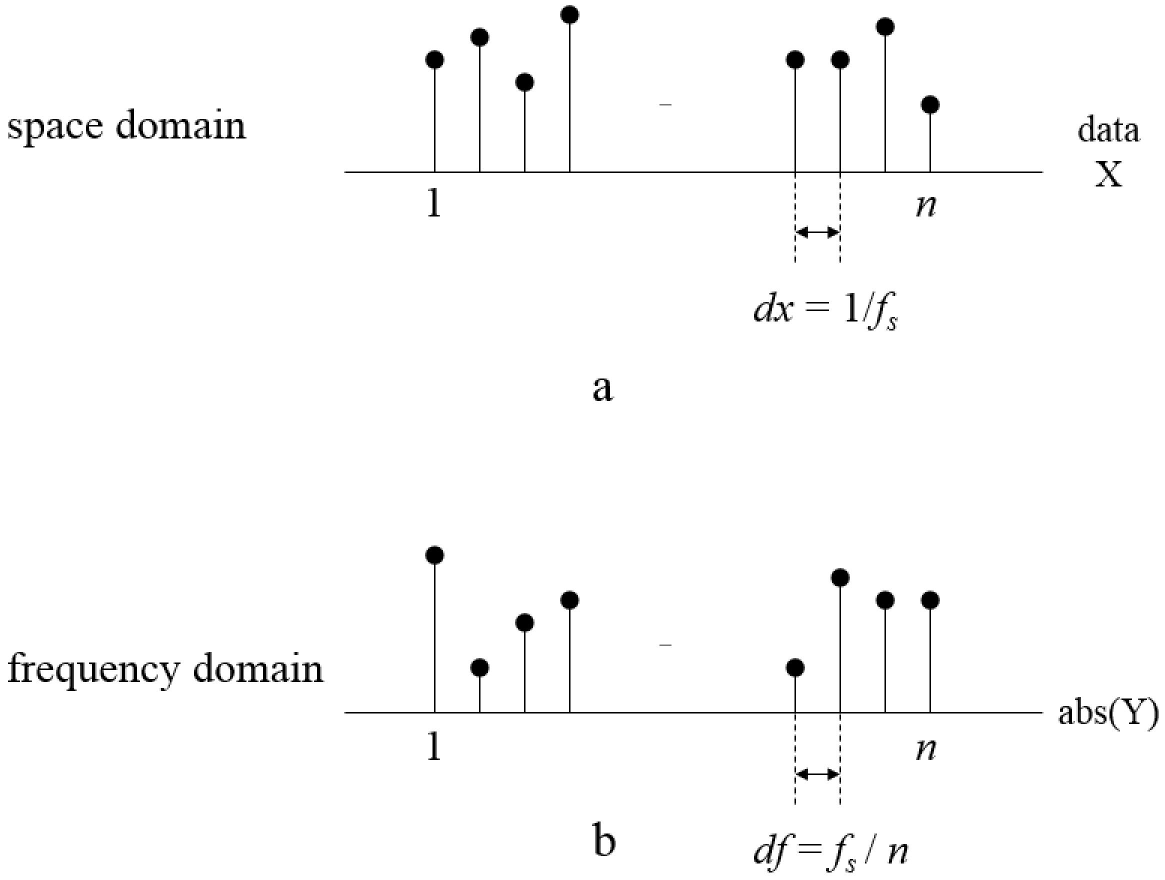

Figure 4.9: A signal of length n in space (or time) domain which is sampled with sampling frequency f_s, b) Fourier transform of the signal in frequency domain($Y_{p+1} = \sum_{j=1}^{n-1} e^{\frac{-2\pi i\, jp}{n}} X_{j+1}$) .

Fig. 4.11 shows the recorded CCD images when a green and red He-Ne lasers were both presented in the input.We used a setup as shown in Fig. 4.12 to record the spectrum of the two lasers simultaneously. A beam splitter was used to have both lasers on the pinhole simultaneously.

Fig. 4.13 shows the procedure we have calculated the segmented spectrums when we have the green and red lasers as the input signals. First we recover the M individual segments independently, then concatenate the segments as shown in Fig. 4.13 b. Fig. 4.13 a and b compares the obtained spectrums by a dispersive spectrometer and our built static-FTS respectively. As it is clear from these figures, our designed spectrometer can resolve two wavelengths on a segment while the dispersive one can only resolve a single wavelength. This is why the resolution of our spectrometer is two times

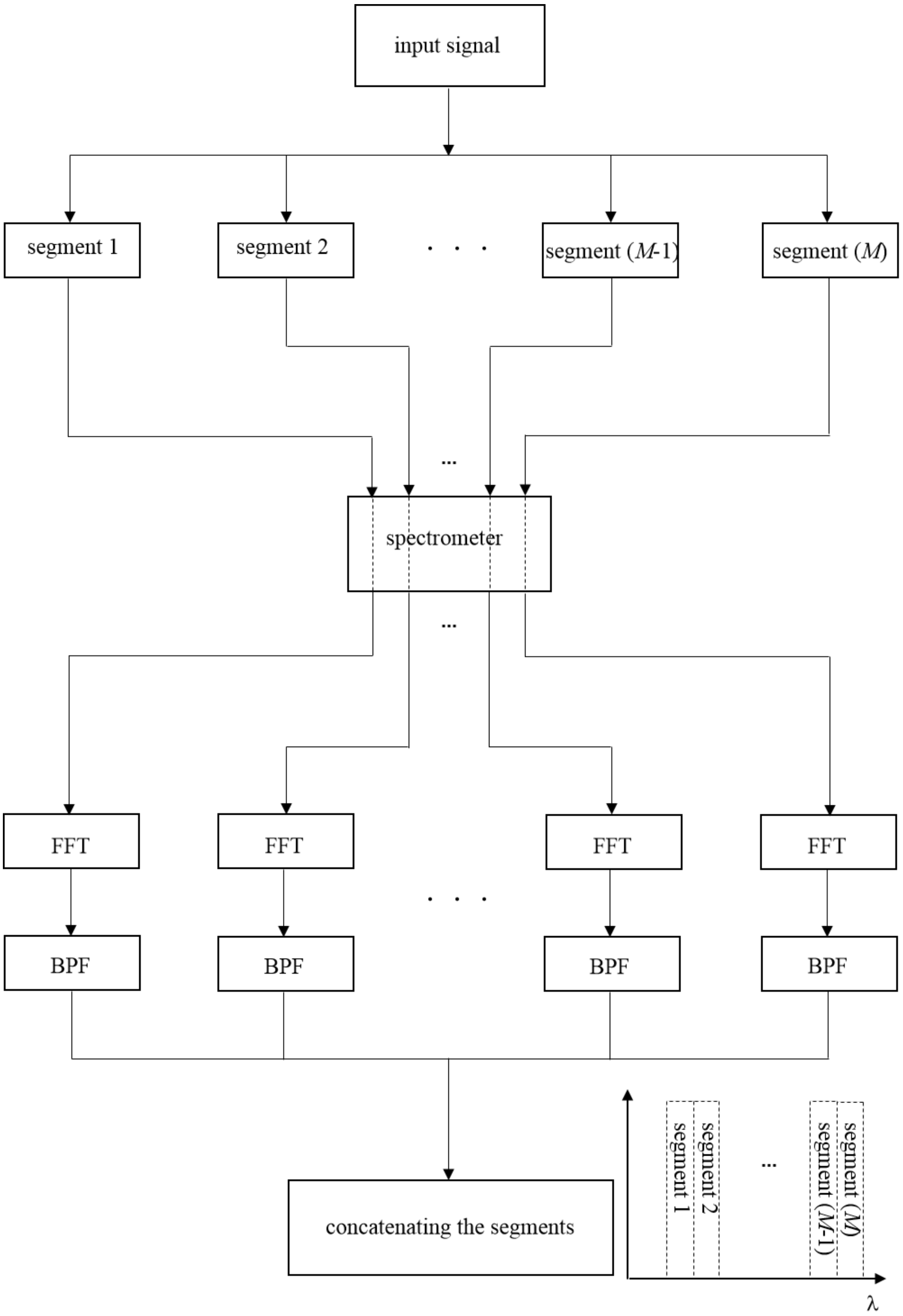

Figure 4.10: The flow chart of the signal processing on the recorded data on the CCD.

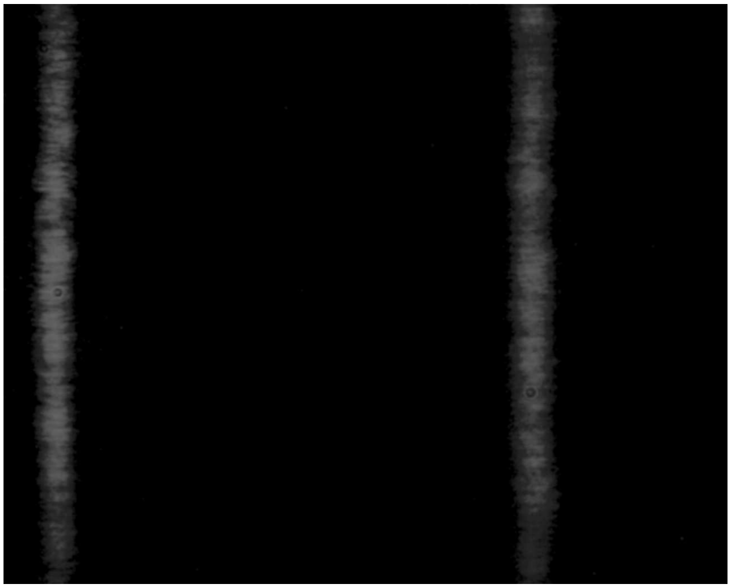

Figure 4.11: Recorded image of a green and a He-Ne red lasers by the CCD.

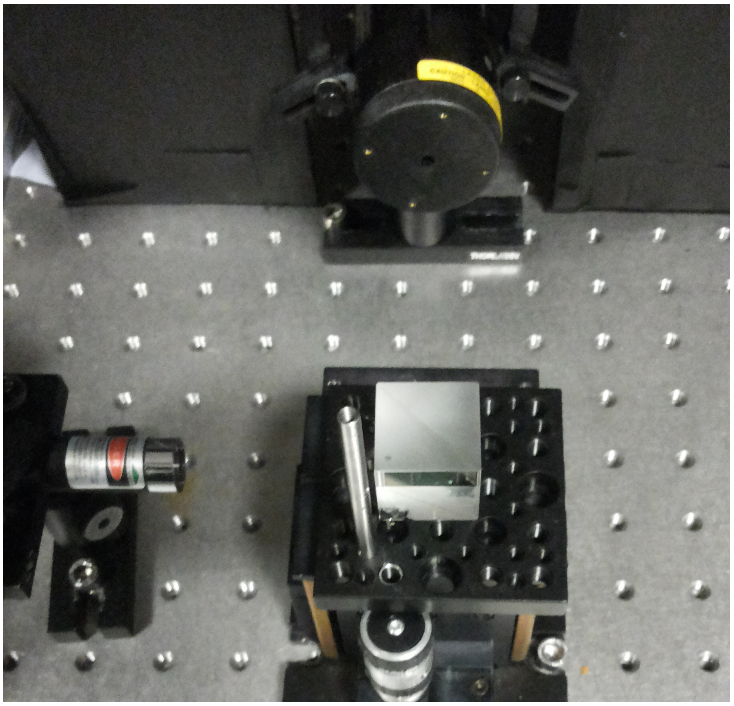

Figure 4.12: The set-up to record the green and red lasers simultaneously.

better compared to that of the dispersive one. In order to increase the resolution of the spectrometer we have to increase the maximum PLD which is directly proportional to the CCD camera dimension.

The calculated total spectrums are shown in Fig. 4.14, Fig. 4.15 and Fig. 4.16 for both dispersive and our static-FTS spectrometer where the peaks are at 532 nm for the green laser and 632 nm for the red laser.

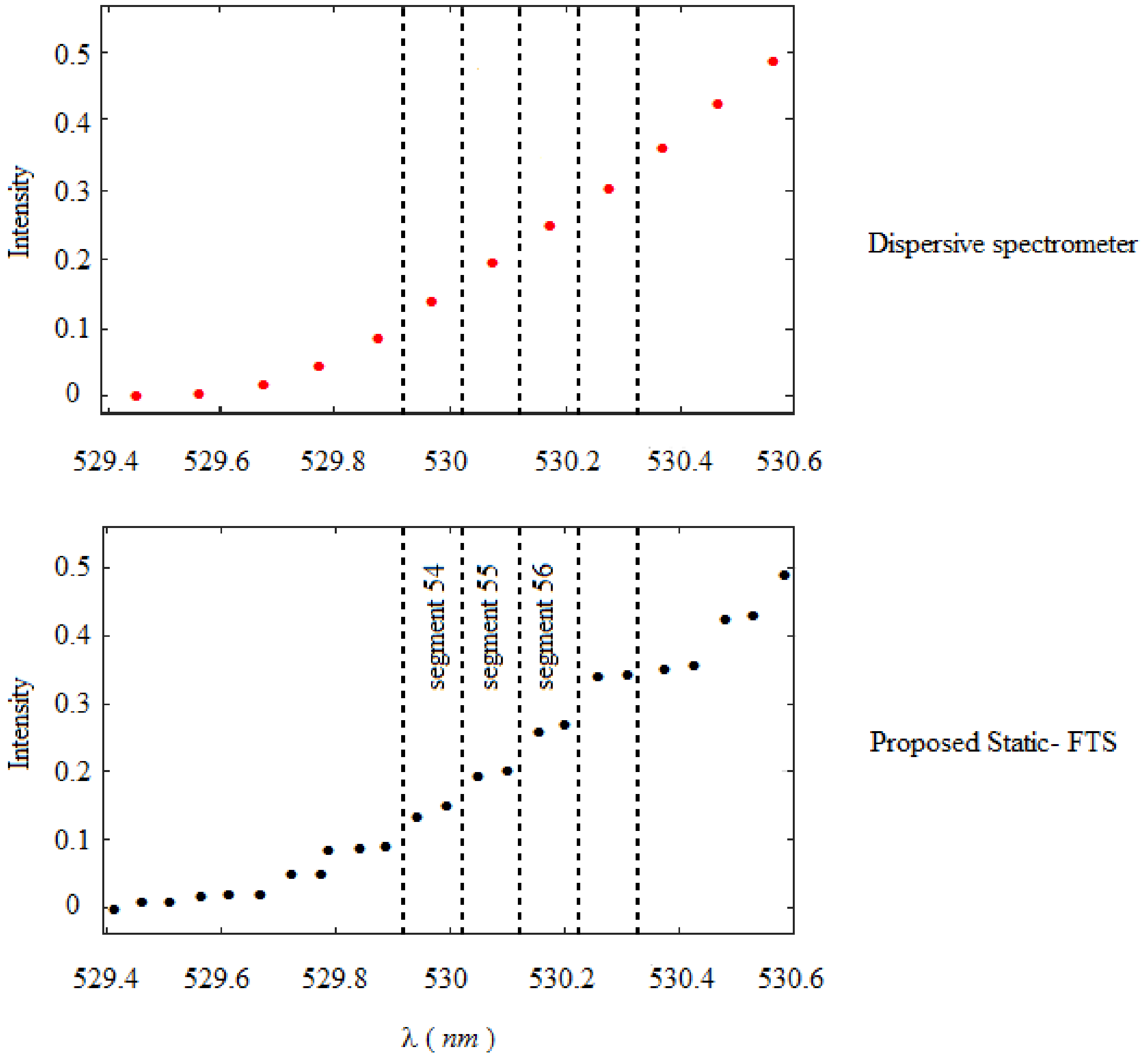

Figure 4.13: The procedure of individual segment analysis and concatenating them to obtain the input signal spectrum. a) the obtained spectrum by the dispersive spectrometer b) the individual segments spectrum obtained by our static-FTS.

The whole set-up photograph of the broadband and high resolution static Fourier transform spectrometer is shown in Fig. 4.17.

The recorded spectrum of the halogen lamp with the proposed spectrometer is shown in Fig. 4.18. The black solid line indicates the recorded spectrum with our device, and

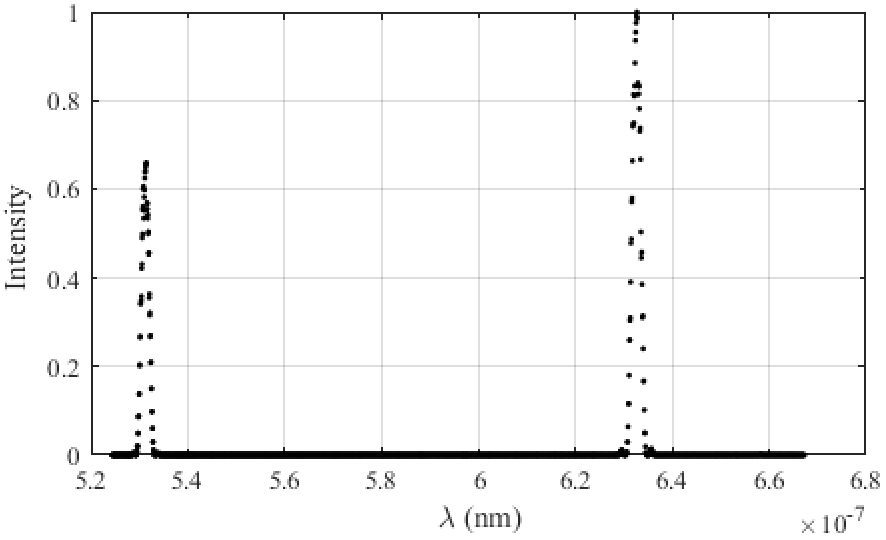

Figure 4.14: The recorded spectrum of a green ($532\,nm$) and a red He-Ne ($632.8\,nm$) lasers by our static-FTS. The measured bandwidths are roughly $1.9\,nm$ and $2.1\,nm$ for the green and red HeNe lasers respectively.

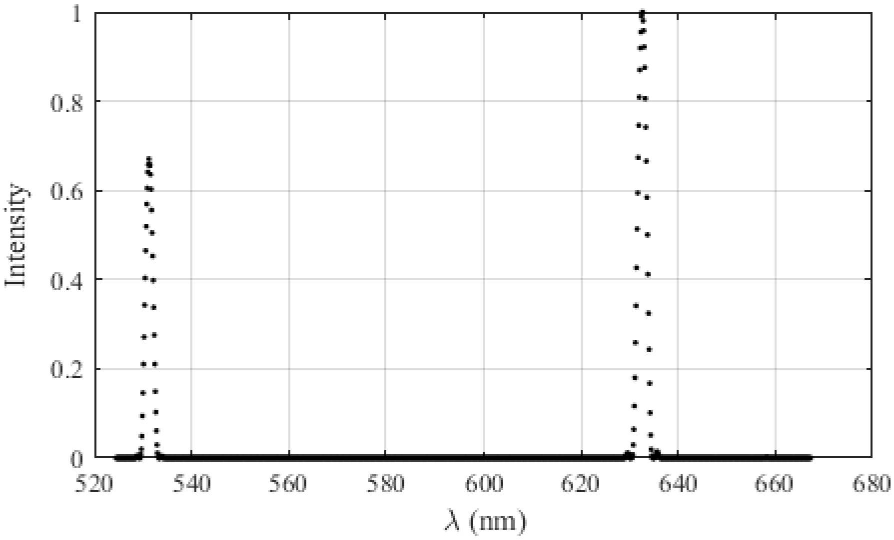

Figure 4.15: The recorded spectrum of a green ($532\,nm$) and a red He-Ne ($632.8\,nm$) lasers by the dispersive spectrometer.

the dashed line indicates the spectrum recorded with OceanOptics' HR4000 spectrometer. There is a good agreement with the recorded spectrums of the two spectrometers. In conclusion a compact, high resolution and potentially broadband static-FTS based on band-pass sampling is demonstrated. The experimental spectrometer functions as a hybrid dispersive and a static FT spectrometer and has $140\,nm$ bandwidth with $1.9\,cm^{-1}$ resolution.

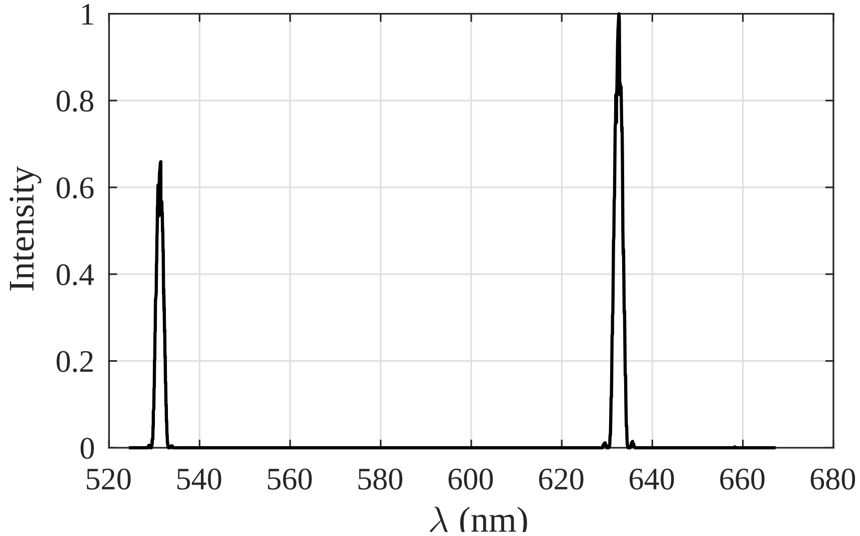

Figure 4.16: The recorded spectrum of a green ($532nm$) and a red He-Ne ($632.8nm$) lasers by our static-FTS. The measured bandwidths are roughly $1.9\,nm$ and $2.1\,nm$ for the green and red HeNe lasers respectively.

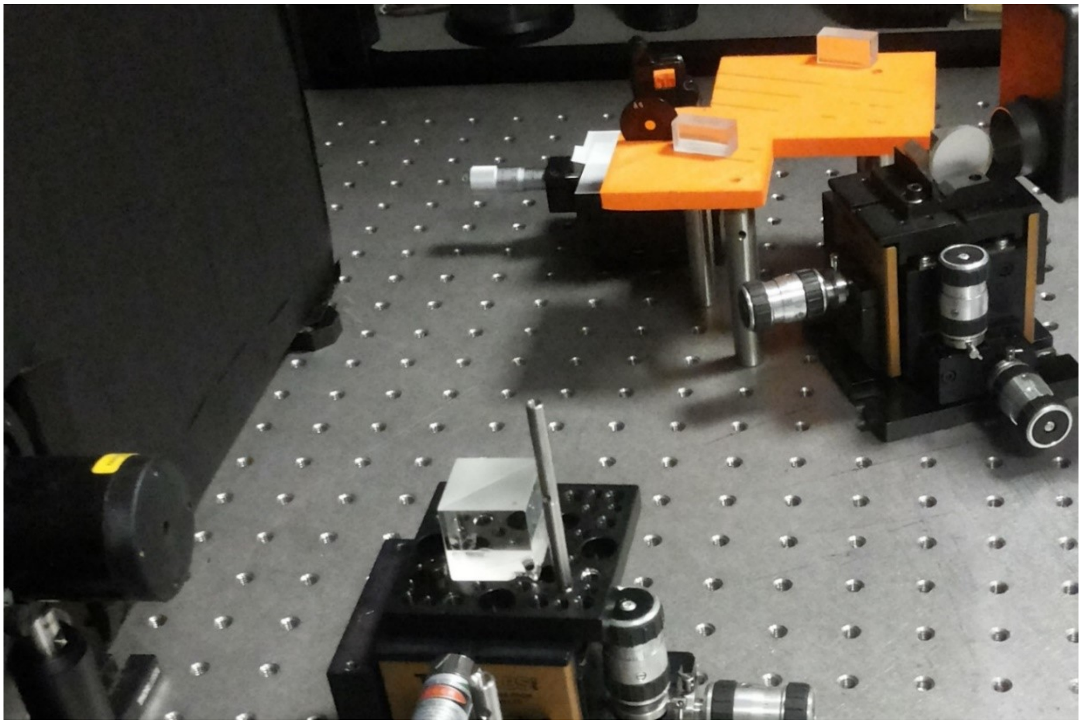

Figure 4.17: The photograph of the whole set-up of the broadband and high resolution static Fourier transform spectrometer.

If we consider only the dispersive part, the pixel resolution would have been $0.11\,nm$ or $3.5\,cm^{-1}$. While using the static FT, the pixel resolution of the device depends on the inverse of maximum delay and it is roughly $0.05\,nm$ or $1.9\,cm^{-1}$. The device bandwidth and resolution are limited by the CCD camera dimensions which here we have used a

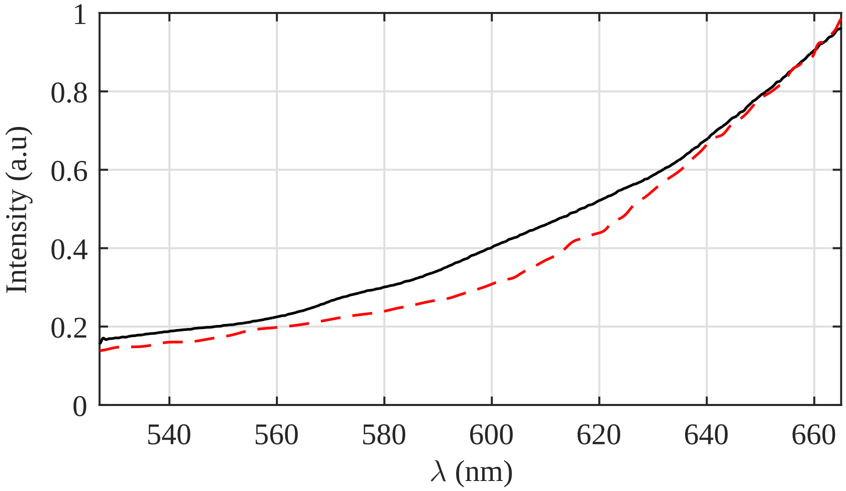

Figure 4.18: The recorded spectrums of Halogen lamp by our static-FTS (black solid line) and Ocean Optics HR4000 spectrometer (red dashed line). The resolution for the static-FTS is roughly $1.9\,cm^{-1}$. Total spectrum recording time is 5 seconds.

1.3 megapixels PixeLINK CCD camera with CCD array size of $6.65\,mm \times 5.32\,mm$. However, the method is scalable such that increasing the CCD dimensions will increase the bandwidth and the resolution of the spectrometer. This subject as well as the condition in which we can obtain maximum resolution are discussed in detail in the next section.

4.4 Optimization of the Device Resolution

In practice the resolution of a spectrometer device (O_r) is calculated as follows [24]:

$$O_r = D_r \times P_r \tag{4.12}$$

where, dispersion (D_r) is the number of the pixels (corresponds to the number of data points) which a monochromator laser beams occupy on the CCD, and pixel resolution (P_r) is defined as (see Fig. 4.19):

$$P_r = \frac{\text{Device Bandwidth}}{N_y}$$

where, N_y is the number of pixels (in our case the pixel numbers in y-direction). Therefore the device resolution can be expressed as:

$$O_r = D_r \times \frac{\text{Device Bandwidth}}{N_y} \tag{4.13}$$

Clearly, due to entrance slit, even the beams of a single wavelength laser diverge and occupy more than a single pixel on the CCD. Here we have assumed the pixel dimensions as big as a few microns. Considering our prototyped device as a dispersive spectrometer, since the bandwidth of the device is $140\,nm$, the number of pixels is $N_y = 1280$ and the number of data points $D_r = 18\,\text{pixels}$, ignoring the PLD direction (consider the device only as a dispersive spectrometer) we can calculate the device resolution as:

$$O_r = \frac{140\,nm}{1280\,\text{pixels}} \times 18\,\text{pixels} = 1.9\,nm$$

A 1-D CCD camera of pixel length Δ is illustrated in Fig. 4.19 a, and the pixels are numbered from 1 to N_y. The pixels which the beams of a single wavelength laser occupy are numbered from 1 to D_r and illustrated in Fig. 4.19 b.

In order to reach the ultimate resolution ($\frac{1}{2n\delta}$) in our designed and prototyped device, we must have a CCD of pixel length as $D_r \times \Delta$. It means, In the segment direction, the single wavelength laser beams must occupy only a single pixel on the CCD.

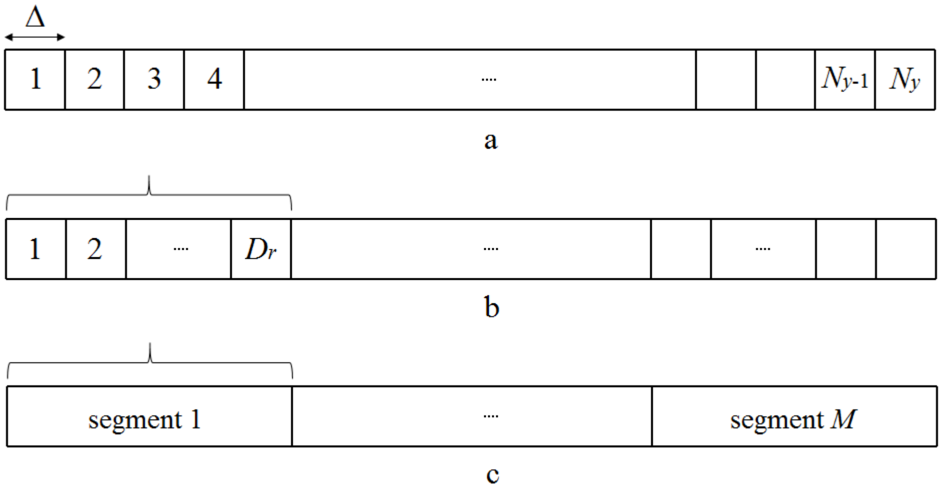

Figure 4.19: 1-D CCD representation, a) A CCD camera of pixel number of N_y and pixel width of Δ, b) The beams of a single wavelength laser occupies D_r pixels, and c) A CCD camera of pixel number of M and pixel width of $D_r\Delta$ which each pixel named as segment.

Let's consider a CCD of pixel length as $D_r \times \Delta$, then calculate the device resolution as Eq. 4.12. We consider the device in both conditions; First as a dispersive spectrometer (ignoring the PLD direction), then as a broadband static-FTS (the PLD direction also comes into account).

Considering the device as a dispersive spectrometer, we have the following calculations for the device resolution. Since, the CCD pixel length is largened D_r times, $D_r = 1$ which means a single wavelength laser occupies a single pixel (pixels are largened). Also, since the CCD length is constant, the pixel number is reduced to $\frac{N_y}{D_r}$. The device resolution is calculated as follows:

$$O_r = D_r \times P_r = 1 \times \frac{\text{Device Bandwidth}}{N_y/D_r} = D_r \times \frac{\text{Device Bandwidth}}{N_y}$$

The calculated resolution shows that enlarging the pixel length as large as D_r times, does not affect the device resolution.

However, let's consider the device as a broadband static-FTS, which means we are taking the PLD direction into account. In that case, the resolution of the device is calculated as follows:

$$O_r = \frac{D_r \times P_r}{N_d} = \frac{D_r \times \text{Device Bandwidth}}{N_d N_y} \tag{4.14}$$

where, N_d is the number of data points and is calculated according to CCD length in PLD direction and the bandwidth of the signal that hits the pixel, as already explained. Therefore, considering the same example of dispersive case for the static-FTS, since, the number of data points are increased to $D_r \times N_d$, the device resolution is calculated as follows:

$$O_r = \frac{D_r \times P_r}{N_d} = \frac{1 \times \frac{\text{Device Bandwidth}}{N_y / D_r}}{D_r \times N_d} = \frac{\text{Device Bandwidth}}{N_d N_y} \tag{4.15}$$

Comparing Eq. 4.14 and Eq. 4.15 we can clearly understand that enlarging the pixel length such that the beams of a single wavelength laser occupy only a single pixel, improves the device resolution, N_d times, which is the ultimate resolution we can obtain. This resolution value is determined according to the PLD direction of the CCD.

Chapter 5

Raman Scattering

Raman spectroscopy indicates the wavelength shift of a photon due to inelastic scattering and produces the spectral information about molecular vibrations. When a photon of wavelength λ_0 (frequency ν_0) is shined on a sample, most likely a photon of the same wavelength λ_0 will be emitted which is called elastic Rayleigh scattering, however there is a low probability (one per million) that the shined photon loses its energy to or even gain energy from the molecule. This process is called inelastic Raman scattering, which is the fingerprint of the molecules. In inelastic scattering the energy of the emitted photon $h\nu_1$ or $h\nu_2$ is different than the energy of the incident photon $h\nu_0$ as shown in Fig. 5.1. Raman shifts are calculated in wavenumbers as $k = \frac{1}{\lambda_0} - \frac{1}{\lambda_1}$ and is expressed usually in cm^{-1}.

Raman scatterings can be classified according to the energy level of the emitted photons compared to that of the incident photons: The emitted photon has higher energy which is called anti-Stokes else Stokes Raman scattering (Fig. 5.1). In Stokes Raman scattering the incident photons loses the energy to the network while in anti-Stokes Raman scattering energy is transferred from the vibrating molecules to the scattered photons, which means increment of the energy of scattered photons. In the anti-Stokes process, the molecule is intially assumed to be in an excited vibrational state rather than the ground state. Inasmuch as the population of the excited vibrational states is much lower than that of the ground state, the ratio of the intensity of anti-Stokes to the intensity of Stokes Raman scattering is a small number. This ratio can be calculated

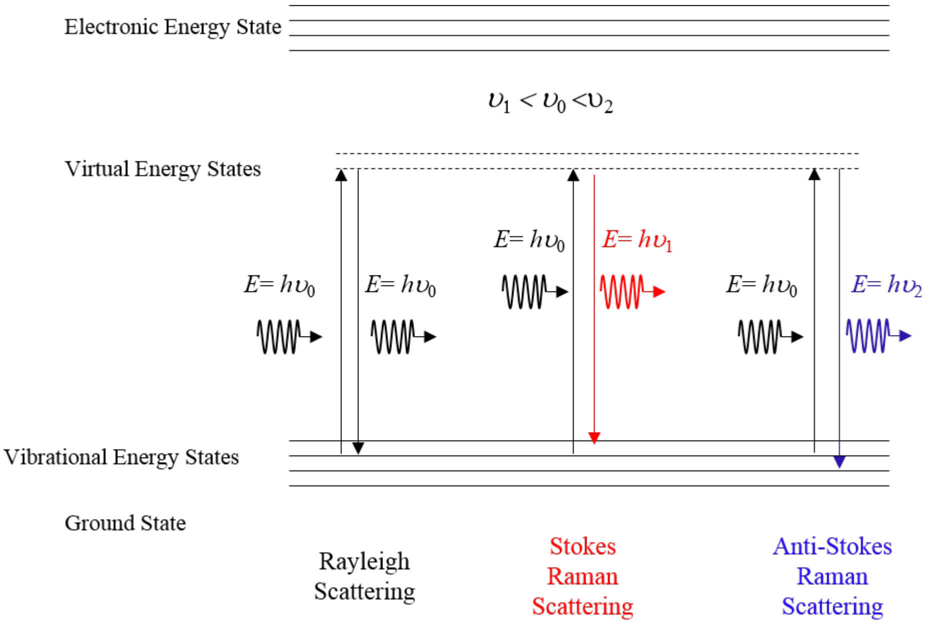

Figure 5.1: Quantum energy transitions for Rayleigh and Raman scattering.

from the Boltzmann factor in thermal equilibrium as follows [32].

$$\frac{I_{anti-stokes}}{I_{stokes}} = \frac{n(\nu = 1)}{n(\nu = 0)} = e^{\frac{-h\nu_{vib}}{k_B T}} \tag{5.1}$$

where, h, k_B, T and ν_{vib} are the Planck's constant, the Boltzmann constant, absolute temperature and wavenumber of the molecule vibration respectively.

5.1 Classical Theory of Raman Scattering

The classical theory of Raman effect was first developed by G. Placzek in 1934. It rests on the fact that the electric field $\vec{E}$ associated with the electromagnetic radiation induces a dipole moment μ in the molecule, given by $\mu = \alpha\vec{E}$, where α is the polarizability of the molecule. The electric field vector $\vec{E}$ itself is assumed in general form as:

$$\vec{E} = E_0 \cos(\omega t) \ = \ E_0 \cos(2\pi\nu_i t) \tag{5.2}$$

where E_0 and ν_i are the amplitude of the vibrating electric field vector and frequency of the incident light radiation respectively. Considering Eq. 5.2, μ can be written as follows:

$$\mu = \alpha E_0 \cos(2\pi\nu_i t) \tag{5.3}$$

The oscillating dipoles emits radiation of its own oscillation with a frequency ν_i, called Rayleigh signal. However, if the polarizability changes as a function of molecular vibration q, then, the polarizability of the molecule can be assumed to be as:

$$\alpha \,=\, \alpha_0 \,+\, q\frac{d\alpha}{dq} + \text{higher orders} \tag{5.4}$$

We can also write q as:

$$q \,=\, q_0 \cos(2\pi\nu_s t) \tag{5.5}$$

where, q_0 and ν_s are the amplitude of the molecular vibration and its frequency respectively.

Substituting the Eq. 5.5 into Eq. 5.4 then the result into Eq. 5.3 we have:

$$\mu = \alpha E_0 \cos(2\pi\nu_i t) + \frac{d\alpha}{dq} q_0 E_0 \cos(2\pi\nu_i t)\cos(2\pi\nu_s t) \tag{5.6}$$

Rewriting using the trigonometric relation $\cos(x) cos(y) = \frac{1}{2}[\cos(x-y) + \cos(x+y)]$, this equation can be arranged as:

$$\mu = \alpha E_0 \cos(2\pi\nu_i t) + \frac{1}{2}\frac{d\alpha}{dq} q_0 E_0 \cos(2\pi(\nu_i - \nu_s)t) + \frac{1}{2}\frac{d\alpha}{dq} q_0 E_0 \cos(2\pi(\nu_i + \nu_s)t) \tag{5.7}$$

It is clear from Eq. 5.7 that the oscillating dipole has three distinct frequency components as ν_i , $(\nu_i - \nu_S)$ and $(\nu_i + \nu_S)$ corresponding to the Rayleigh, Stokes and anti-Stokes scattering signals respectively. As $\frac{d\alpha}{dq}$ is a small number, the amplitude of Stokes and anti-Stokes signals is very small in comparison with that of the Rayleigh signal.

If, $\frac{d\alpha}{dq} = 0$, the amplitude of Stokes and anti-Stokes signal are zero, hence, the molecule is not a Raman active molecule [33, 34].

5.2 Quantum Theory of Raman Scattering

Classical theory of Raman scattering is straightforward but cannot explain the inequality of amplitude of Stokes and anti-Stokes scattered signals, while the quantum explanation is more compatible with the observed phenomena.

Quantum explanation rests on the fact that the energy of the incident photon cannot excite the molecules from ground state to the electronic state, but to a virtual state with lower energy and lifetime that electrons fall down to the ground state after a short time. If the electron goes back to the same vibrational ground level, then the wavelength of the scattered light is the same as the incident light, which is called Rayleigh scattering.

Another possibility for the electrons is vibrational state different from where they are excited. Hence, there is an energy difference between the emitted photon and the incident photon. If the emitted energy is smaller than the incident energy, the process is called Stokes scattering. The opposite is called the anti-Stokes scattering. Now, The intensity ratios between Stokes and anti-Stokes lines can be calculated by the occupation probabilities n of the initial states, $n(\nu = 0)$ for Stokes line and $n(\nu = 1)$ for anti-Stokes line, from the Boltzmann equation in thermal equilibrium (see Eq. 5.1). By considering this equation the difference in the intensity of Stokes and anti-Stokes Raman is clear. Obviously, as the temperature increases the intensity of the Stokes line decreases because the number of the particles in the ground state diminishes while for the anti-Stokes line the opposite takes place which is also clear from the Eq. 5.1 [32–34].

5.3 Challenges in Raman Spectroscopy

As already explained, Raman spectroscopy indicates the wavelength shift of a photon due to inelastic scattering and produces the spectral information about molecular vibrations. However, the cross section for Raman scattering is rather small, on the order of $10^{-31}\,cm^2 - 10^{-26}\,cm^2$ per molecule. This is the important and maybe the biggest drawback of the Raman scattering which leads to a weak scattered signal intensity. The lower intensity of the conventional Raman scattering leads to undesired difficulties in the experiments such as increasing the integration time, using high power laser etc that violate the safety limitation for Bio application, otherwise it is not possible to record the desired Raman signal [35–37]. There are several approaches to overcome the weak signal intensity such as coherent anti-Stokes Raman spectroscopy [38–42], stimulated Raman gain spectroscopy [43–47], surface enhanced Raman spectroscopy [48–52], and tip-enhanced Raman spectroscopy [53–57].

Apart from the small cross section, another problem that takes place in Raman spectroscopy especially in the short wavelength range is the fluorescence emission which can be eliminated by operating in the infrared. However, since the Raman intensity is inversely proportional to the fourth power of the wavelength of the incident light, operating too far in infrared region removes some of these advantages. Since Raman shifts are independent of the excitation wavelength, an optimal excitation wavelength based on the sample type and equipment sensitivity can be chosen.

Since Raman shift is independent of the incident photon energy, it is used to characterise the chemical composition and structure of a sample, which can be in the form of solid, gas, liquid, gel or powder. It is widely used for DNA/RNA analysis, disease diagnosis, bacteria detection, protein detection, forensic application (trace evidence from a crime scene), pharmaceuticals applications (skin depth profiling, compound distribution in tablets etc) and semiconductors (to analysis the purity, composition and defects) etc.

5.4 Surface Enhanced Raman Scattering

Surface Enhanced Raman spectroscopy (SERS) has emerged as a powerful spectroscopy technique to increase the intensity of Raman scattering signals from the analyte of interest. It is generally accepted that the main mechanism of the enhancement is due to the amplification of the light by excitation of localized surface plasmon resonances (LSPR) of the metallic nanoscale features and/or nanoparticles present on the surface where the analyte is put onto [58]. SERS was introduced in the mid-1970s [59–61], and since then significant research has been done to create and optimize SERS substrates with high density of hot spots in order to obtain the largest enhancement factor (EF) [62–65]. Hot-spots which is shown in Fig. 5.2 are the locations near nanostructures where the

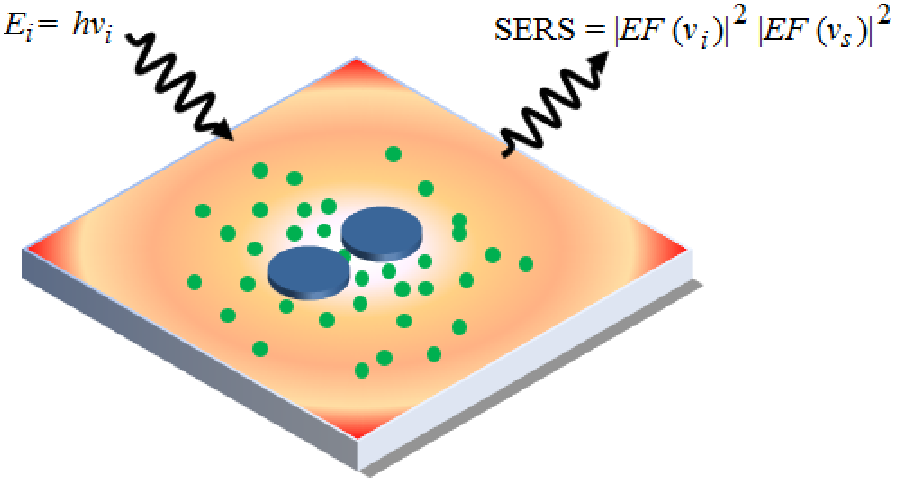

Figure 5.2: Hot spot representation on a SERS substrate. A dimer structure with a random distribution of the molecules is shown on the substrate. ν_i and ν_S are the incident frequency and scattered frequency respectively.

local electric field is enhanced, so that Raman scattering signals from the molecules near the hot spots are enhanced 10^4 to 10^7 times. A high local field is possible with metal nanoparticles of appropriate size, shape and type due to surface Plasmon resonance (SPR) phenomena which is the basis of SERS substrates. For this purpose different types of nanoparticle structures are investigated such as nanospheres, nanoshells, nanodiscs, nanotoroids including their dimer and trimer configurations. With nanospheres of $50\,nm - 100\,nm$ diameter size it is possible to work in visible range and have about 100 times enhancement in local electric field. For example, dimer and trimer gold nanoparticles when excited at $532\,nm$ and $632.8\,nm$ enhancement of 2×10^5 is obtained on the detected Raman signal of Rh6G [66]. Also, in nanoshell structures with similar size there is an increase in local electric field up to about 200 times but also there is a red shift in resonance wavelength [**?**, 67]. In the disc structures the local electric field enhances up to 300 times and resonance wavelength shifts to red part of visible range. For example, In reference [68], nanodiscs with different diameters, thicknesses and inter-disc distances have been excited with a red HeNe laser leading to maximum 1.2×10^6 times enhancement in SERS. Even much higher enhancement is possible with some special substrates enabling single molecule detection [69–72].

Although the noble metals and transition metals such as gold, silver, copper, zinc etc are mainly used as the SERS active substrates, however metal oxides such as CuO, Cu2O, ZnO, TiO2, Fe3O4 and Ag2O are also confirmed to act as the SERS active substrates [73–86]. The first experiment on the metal oxides as the SERS substrate was reported by Yamada et al at 1983. In this work, they observed surface enhanced Raman signal of adsorbed pyridine on the surface of single crystals TiO2 and NiO. Later, within 2007-2009 Zhao et al studied the capability of CuO, CdS, ZnS, CdTe, TiO2 and ZnO as the SERS active substrates [79–83]. They have used 4-mercaptopyridine as the probe molecule. The obtained enhancement factors were in the range of $2-4$ orders of magnitude.

The charge transfer (CT) mechanism between adsorbed analytes and the substrate is responsible for observed SERS from semiconductors substrates. In this process, the molecular polarizability tensor involved in charge transfer are magnified, which leads to enhancement in recorded Raman signal [84].

The main concern with the metal oxides as the SERS substrate is the enhancement factor which is solved by modifying their surface by noble or transition metals, which causes the charge transfer effect within the metal/metal oxide interface. The charge transfer allows manipulation of the localized surface Plasmon resonance and finally the Raman signal enhancement factor [87]. More recently, some works were done to show this effect. For example, in 2007 Yanfei Wang et al [78] showed the capability of copper oxide as a SERS active substrate with enhancement factor of two orders of magnitude. However, For instance, in 2016 Jayram et al [85] used silver decorated copper oxide nanostructured thin films as the SERS substrate and obtained enhancement factor of above seven orders of magnitude which showed five orders of magnitude much enhancement factor compared to Yanfei Wang's works. In another work, in 2017 Wu et all [86] has obtained enhancement factor of above seven orders of magnitude of R6G on $\alpha - MoO_{3-x}$ substrate by defect engineering.

The EF is generally written as [88, 89]:

$$EF = \frac{|E_{loc}(\omega_L)|^2}{|E_{inc}|^2} \times \frac{|E_{loc}(\omega_R)|^2}{|E_{inc}|^2}, \tag{5.8}$$

where E_{inc} is the amplitude of the incident laser light, and $E_{loc}(\omega_L)$ and $E_{loc}(\omega_R)$ are the local electric field amplitude at the incident laser frequency and the local electric field amplitude at the scattered Raman signal frequency respectively. In most cases the Raman shift is small enough to justify the approximation: $\omega_L \approx \omega_R$, in which case the SERS enhancement is simply proportional to the fourth power of the local field enhancement:

$$EF \approx \frac{|E_{loc}(\omega_L)|^4}{|E_{inc}(\omega_L)|^4}. \tag{5.9}$$

Although the SERS enhancement is roughly proportional to the fourth power of local electric field, in practice the overall SERS enhancement is much less since most of the attached molecules do not experience high local field.

5.4.1 Substrate Preparation

Over the years, generally, two different ways of building a SERS active substrate has emerged; coating a substrate with pre-synthesized nanoparticles by techniques such as chemical synthesis, colloidal aggregation etc., which are called as bottom-up methods [58,90–95], and fabrication of a nanoparticle template on a substrate by the nanofabrication techniques such as electron beam lithography (EBL), focused ion beam (FIB), scanning probe lithography etc., which are called as top-down methods [96–100]. Synthesis of colloidal nanoparticles is straightforward but it is too time consuming process, however it is appropriate for large scale production. Also, the nanoparticles accumulation is another disadvantage of this kind of process. The patterned substrates have advantages compared to the nanoparticle colloids such as adjusting the inter-particle distance, uniformity in enhancement factor, repeatability, and absence of particle aggregation issues. However, it has disadvantages as it is a time consuming process, more complicated and costly and also needs high tech fabrication facilities.

For instance, the Fig.5.3 demonstrates the procedure of fabrication of patterned substrates by EBL technique. The procedure is as follows: First a substrate (for instance, silicon wafer) is coated with an EBL resists such as polymethyl methacrylate (PMMA), ZEP520 or polydimethyl glutarimide (PMGI), then it is exposed to EBL beam with a given pattern (this process takes a couple of hours or even days). The exposed substrate must be developed with an appropriate developer depends on the coated resist. Now, it must be coated with the metal of interest such as gold, silver etc. The last process is called lift-off process which is carried out usually with acetone and an ultrasonic agitation.

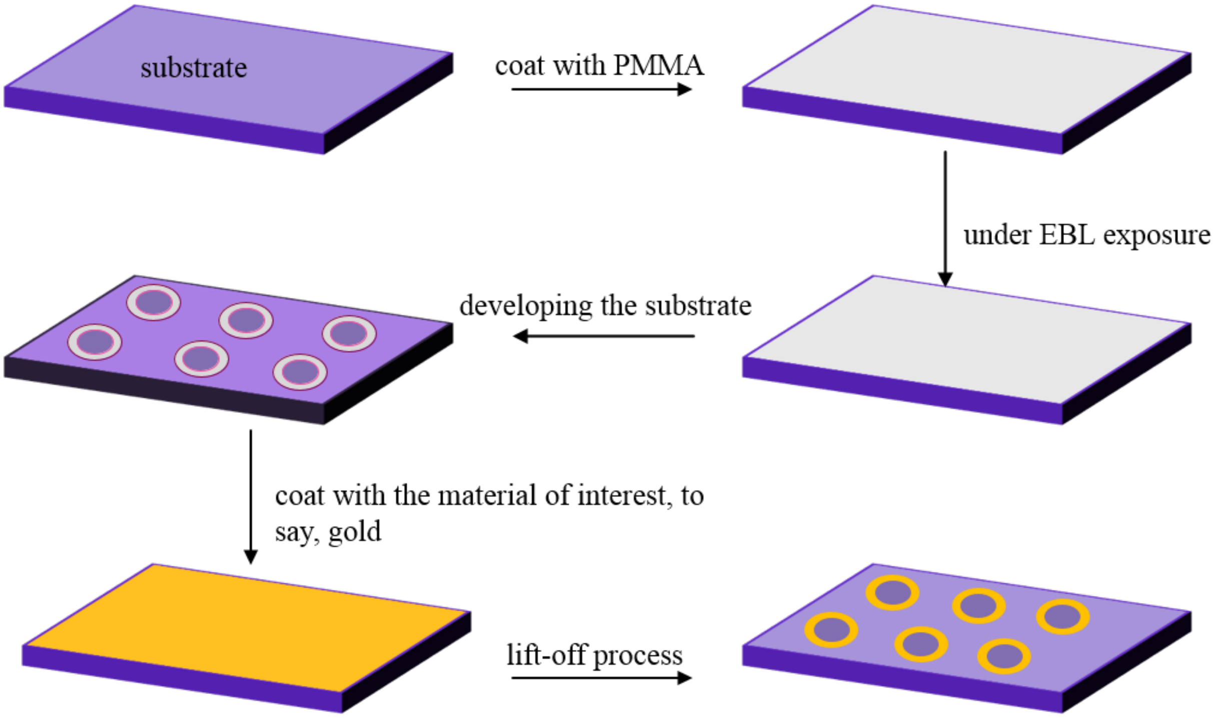

Figure 5.3: Procedure of fabrication of patterned substrates by EBL technique for SERS applications.

Recently, some researchers focused on synthesis of colloidal nanoparticles by electrolysis method for applications in the inkjet printing and SERS applications [101–104]. Synthesis of nanoparticles by electrolysis is a bottom-up method which is accomplished due to reduction and oxidation (see Fig. 5.4) at the cathode and anode respectively, and compared to most of the other techniques this is a simple and economical method. It is also advantageous since the size of the particles as well as their morphology can be controlled by the experiment conditions and deposition parameters such as temperature, current density, reaction media etc. The general setup of an electrolysis method is represented in Fig. 5.4, which two electrodes namely anode and cathode are placed inside the electrolyte and a voltage source is connected to the electrodes. The electrolyte and electrodes are chosen based on the structures of interest.

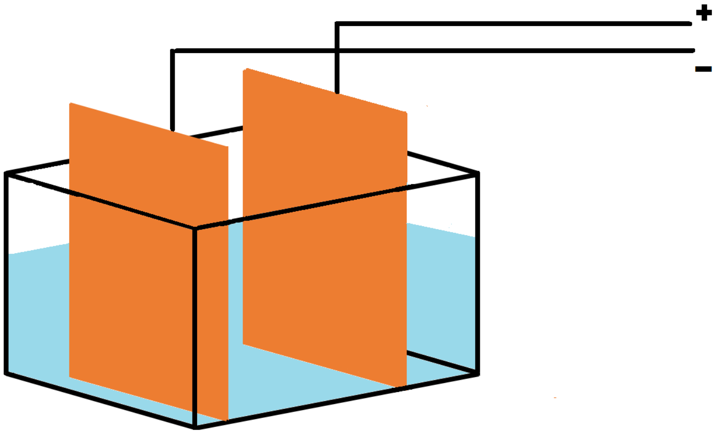

Figure 5.4: The general setup of an electrolysis method. Two electrodes as anode and cathode are placed inside the electrolyte and a voltage source is connected to these electrodes.

Therefore, electrochemical method is one of the simplest way of producing copper oxide nanoparticles which is discussed in the literature [104–110]. For example, Yuan et al. [104] have described the effect of current and electrolyte on the shape and size of the copper oxide nanostructures. In their experiment they have used copper plate as the anode and stainless steel plate as the cathode since the copper oxide nanoclusters will be collected on the cathode surface. The sacrificial anode and 1 molar sodium nitrate ($NaNO_3$) electrolyte were used for the synthesis of copper oxide nanocrystals under room temperature without any surfactants. They have investigated the electrolyte effect on the formation of copper oxide on the cathode surface. With aqueous $Cu(NO_3)_2$ as the electrolyte, no copper oxide was formed on the surface of the cathode but copper was formed there, but with $NaNO_3$ copper oxide particles were formed. They have also investigated the effect of the reaction media on the nanoclusters morphology by dissolving the $NaNO_3$ once in pure distilled water and then in $H_2O - EtOH$ mix-solvent (equal volume ratio). They have obtained a uniform and mono-disperse copper oxide nanospindles with about $80\,nm - 100\,nm$ in diameter and $200\,nm - 300\,nm$ in length when pure distilled water was used as an electrolyte. In contrast, with $H_2O - EtOH$ mix-solvent as the electrolyte, they have obtained copper oxide nanorods of $20\,nm - 50\,nm$ in diameter and $200\,nm - 300\,nm$ in length with sharp ends morphology. They have also investigated the effect of current density on the shape and size of the formed copper oxide particles. For three different current densities of $5\,mA/cm^2$, $10\,mA/cm^2$ and $20\,mA/cm^2$ they have obtained nanospindle, nanorods and irregular nanoplates copper oxide particles respectively. Finally, their total experiment time is a few hours.

Xu et al. [105] have synthesized leaf-like CuO mesocrystals by the electrochemical method then have discussed their capability as anode materials for lithium ion batteries. In their experiment, they have used copper foils as the working and counter electrodes and $NaNO_3$ of 100 mM as the electrolyte. The uniform copper oxide mesocrystal were formed at a $3\,V\,DC$ and temperature of $70^\circ\,C$. The width and the length of the produced CuO nanoleaves are about $50\,nm$ and several hundred nanometers respectively. Each produced CuO nanoleaf is the assembly of plenty of small particles causing to a rough surface of the formed CuO nanoleaves. However, they are very thin which is important for electrochemical performance. The importance of the CuO mesocrystals as anode material for lithium ion batteries are high reversible capacity and good cycle performance.

Lu et al. [106] have synthesized flower-like microspheres CuO by anodic dissolution of bulk Cu using sodium hydroxide of concentration 2 M as the electrolyte solution at room temperature. By this method they have synthesized copper oxide flower-like microspheres (CuO FM) of ca. $3\,\mu m$ which its surface is quite rough. They have investigated the sodium hydroxide concentration on the size of the formed CuO flower-like microspheres. The size of these microspheres were tunable from $400\,nm - 800\,nm$ to $6\,\mu m - 8\,\mu m$ by changing the concentration of sodium hydroxide from 0.5 M to 4.0 M.

Toboonsung et al. [110] have synthesized CuO nanorods and their bundles by an electrochemical dissolution and deposition process then studied the electrode separation, the deposition time and voltage effect on the nanorods morphology, thickness and the ratio of bundles/nanorods. They have used copper plates for both anode and cathode and also have attached a glass substrate (small size compared to the cathode plate) on the cathode to collect copper oxide nanostructures. Deionized water was used as the electrolyte, and a voltage of $10\,V - 30\,VDC$ was applied to the electrodes. They also changed the electrodes separation from $2\,mm$ to $10\,mm$ as well as the deposition time from one hour to eight hours. They found that the thickness of the formed nanoparticles decreased with increasing electrode separation, due to reduction in current. The maximum obtained thickness was $635\,nm$ corresponds to higher current and the minimum obtained thickness was approximately $25\,nm$ corresponds to lower current. The deposition time effect from 1 hour to 8 hours was investigated at electrode separation of $8\,mm$ and voltage of $10\,V$. After a deposition time of 1 hour to 2 hours, only nanorods with mean diameter in the range of $25\,nm - 40\,nm$ were observed, while after 3 hours to 8 hours, a mixture of nanorods and their bundles with mean diameter in the range of $40\,nm - 110\,nm$ were formed.

Chapter 6

Real-Time Substrates for SERS Applications

In this section of the thesis we present a simple, real-time operating and wavelength tunable copper SERS substrate formed by the electrolysis [111]. There are already widely used electrolysis methods for synthesis of nanoparticles as mentioned earlier, however those studies include metals salts in the electrolyte, and it takes hours to days for nanoparticle production in the solution or on the cathode. There are reports which indicate nanoparticle production on the cathode [110] and the anode [112] with distilled water alone but their measurements were done after hours of electrolysis. However, here, we observed production of cube shaped nanoparticles on the copper anode surface in matter of a few minutes using just the ultra-pure water (UPW) as the electrolyte. Our measurements indicate that the ions are extracted from the Cu anode form cube shaped copper oxide nanoparticles on the anode surface in such a short time, and we show that this anode can be used as a SERS substrate. Initially, the anode is removed from the electrolysis cell and a solution of rhodamine B (RhB) is applied over the surface to perform Raman spectroscopy. We obtained enhancement of Raman signals over five orders of magnitude. Afterwards, the experimental setup was modified to allow real-time Raman measurements of RhB while the electrolysis is ongoing, and we again obtained enhancement over five orders of magnitude within 90 seconds of electrolysis. Similar enhancements were obtained with crystal violet (CV) solutions as well.

The proposed method has some key advantages over existing SERS substrates: its not only a real time SERS substrate but also is a very fast, simple and a low cost technique. Furthermore this substrate is tunable in wavelength -albeit only irreversibly and in one direction- as the particle size is increasing as a function of time which implies that plasmon resonance wavelengths are increasing as well. This technique also omits the need for an electrolyte of containing the metal ions of interest for the nanoparticle production as just the deionized or distilled water is enough. This is an important point for the Raman measurements because the electrolyte being simply just the water there will not be an extra background noise added to the spectrum. This technique also allows preparation of a large effective area for SERS enhancement, virtually unlimited area. As long as the current distribution over the anode is uniform which is a trivial arrangement, nanoparticle distribution will have quite homogenous distribution. Other metal electrodes made of brass, zinc (Zn), silver (Ag) and aluminum (Al) also were tried as the anode but except brass none of the other metals showed any enhancement. Also it is confirmed with electron microscope images that there was nanoparticle formation on copper and brass electrodes but none on the other metals studied.

6.1 Experimental Setup

Three surface-cleaned copper electrodes have been placed inside a 3 mL quartz cuvette in which two of them were put in parallel, facing each other and electrically connected together while the third one is perpendicular to these electrodes, as illustrated in Fig. 6.1. The single electrode is used as the anode and the two parallel electrodes are used as the cathode. The reason that the anode and cathode are not located face to face is because we wanted to place the Raman probe facing the anode from the remaining facet of the cuvette.

In order to be able to record Raman spectrum of analytes while the nanoparticles are formed on the anode, the Raman probe is set in front of the quartz cuvette on an XYZ optical stage for ease of alignment. Longitudinal alignment (z-axis) of the probe is necessary for focusing the light source at the anode surface and capturing the backscattered Raman signal, while lateral positioning is necessary for accessing the different

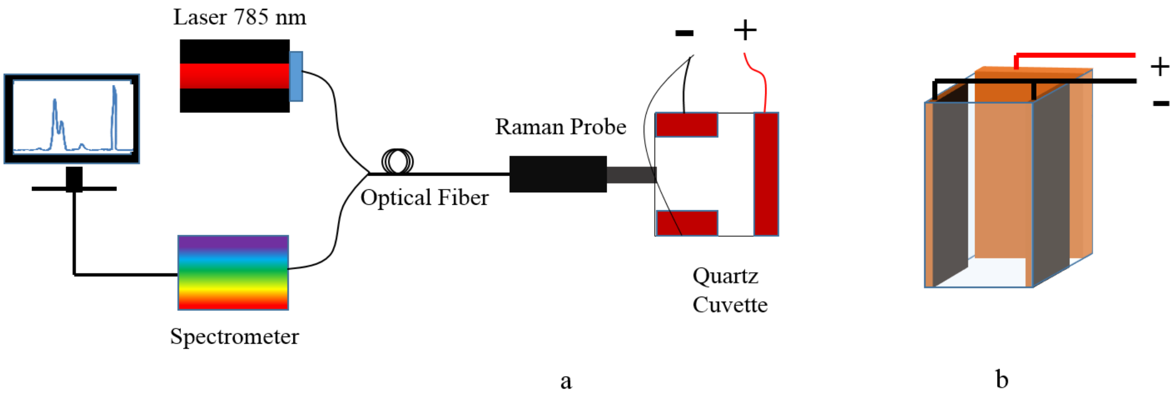

Figure 6.1: a) Drawing of the experimental setup for preparing real time SERS substrate and recording the Raman spectrum simultaneously. b) Quartz cuvette used as the electrolysis chamber and as a container simultaneously for the solution that the Raman spectrum is of interest. The anode and cathode electrode dimensions are $50\,mm \times 8.5\,mm \times 0.25\,mm$ and $50\,mm \times 5.5\,mm \times 0.25\,mm$ respectively. The Raman signal was recorded head-on from the anode surface.

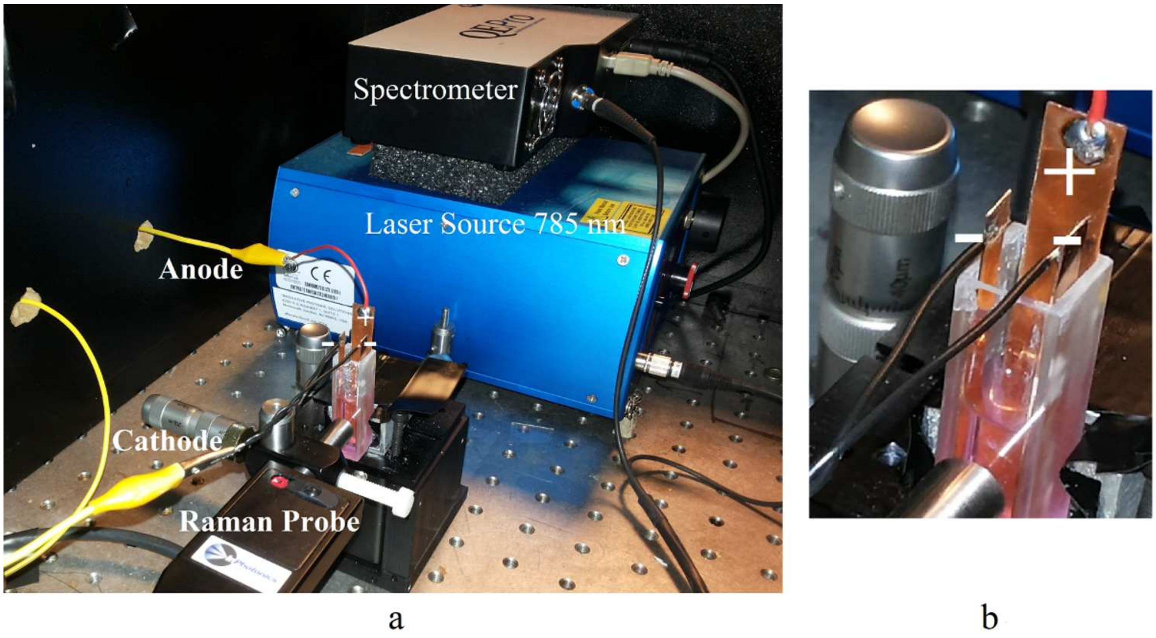

Figure 6.2: A photograph of the experimental setup for substrate preparation and recording the Raman spectrum. Quartz cuvette and the Raman probe are both set on optical XYZ stages for ease of alignment. Laser light is launched from the Raman probe and the back-scattered light from anode surface propagates back through the Raman probe to the spectrometer.

parts of the anode surface. Raman probe is made by InPhotonics Inc., the spectrometer (QEpro) and the 785 nm infrared laser source with adjustable power up to 500 mW are made by Ocean Optics Inc. Laser light is launched from the Raman probe and the back-scattered light from anode surface propagates back through the Raman probe to the spectrometer. A photograph of the experimental set-up is shown in Fig. 6.2.

6.2 SEM Images and SERS Results

Initially, the cuvette is filled with ultra-pure water, and just the electrolysis is performed without any Raman measurement. The conductivity of the water was $55\,nS/cm$, and the applied voltage between the anode and the cathode was $32\,V$. After five minutes of electrolysis the anode electrode was removed and dried. The captured scanning electron microscope (SEM) images of two different areas from the anode surface after five minutes electrolysis as shown in Fig. 6.3 confirms the production of cubic nanoparticles with dimensions upto $400\,nm$. It will be explained later that the nanocubes are actually CuO particles.

In the next set of experiments nanoparticle production and Raman experiments were performed simultaneously. After replacing the electrodes with a new and clean copper electrodes, we filled the cuvette with rhodamine B (RhB) dissolved in ultra-pure water of concentration $5\,\mu M$. The conductivity of this solution was $1.56\,\mu S/cm$, and $32\,V$ was applied during the electrolysis. SEM images of the nanoparticles formed on the anode after 90 seconds and 5 minutes of electrolysis time are shown in Fig. 6.4. In this figure, histograms of nanocubes dimensions are shown under the images. In the 90 second run the average particle size is about $100\,nm$ but in the 5 min run there are two peaks centered at $100\,nm$ and $300\,nm$ of particle size. It is quite interesting that we have two groups of nanocubes differing in size forming on the substrate.

Back scattered Raman signals from the anode surface was recorded as a function of time. Since $5\,\mu M$ solution of RhB is too low of a concentration for a normal Raman spectrum recording it is actually impossible to record the spectrum without SERS enhancement. Therefore, we had to record normal Raman spectrum of much higher concentration RhB solution ($100\,mM$) and normalize measurement results to obtain the enhancement factor of our substrate since the Raman intensity is proportional to the number density of the analyte. Namely, to quantify the enhancement of the recorded Raman signal we use [94, 95]:

$$EF = \frac{I_{SERS}}{I_{ref}} \times \frac{C_{ref}}{C_{SERS}},$$

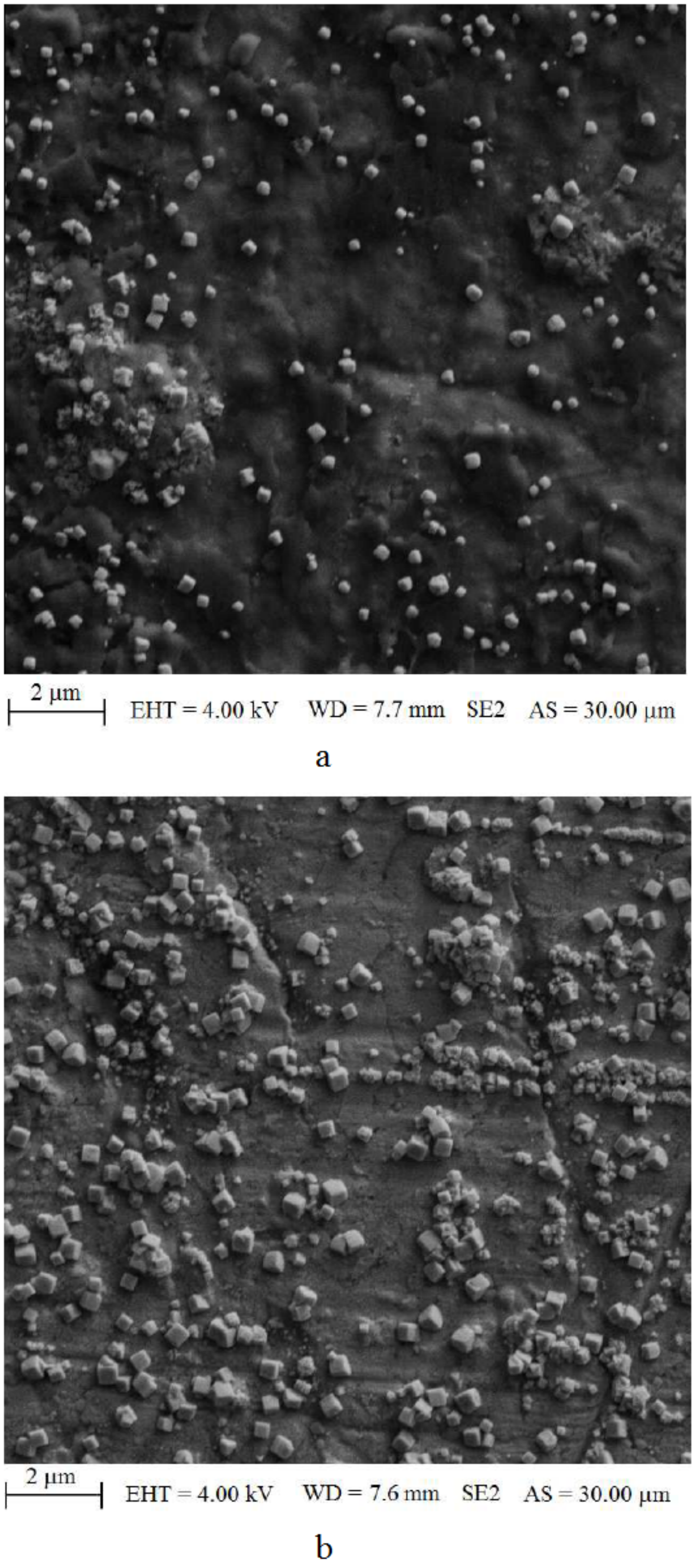

Figure 6.3: SEM images of two different areas from anode surface after 5 minutes of electrolysis while the container was filled with ultra-pure water.

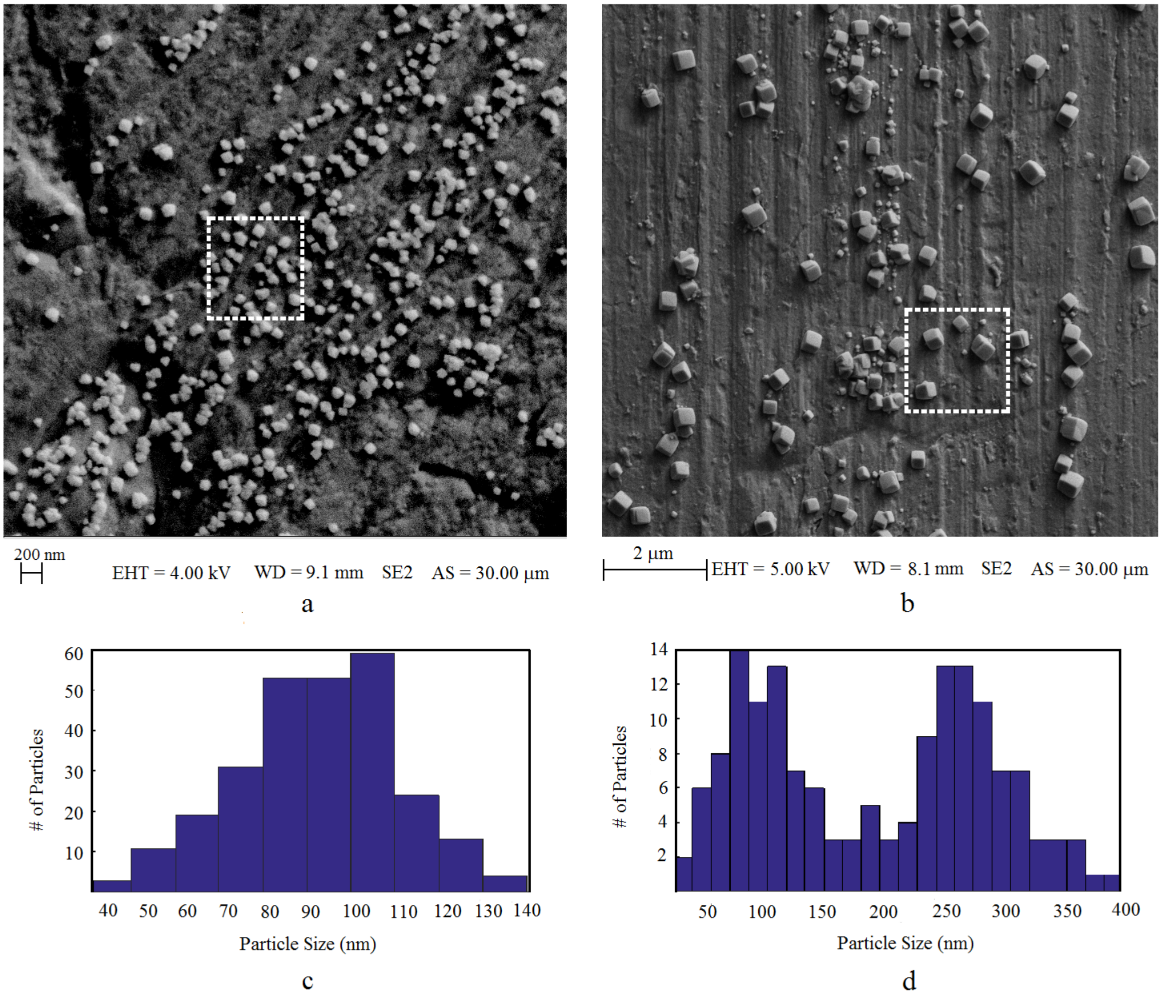

Figure 6.4: SEM images from anode surface for different electrolysis times when container was filled with $5\,\mu M$ RhB. a) 90 seconds of electrolysis time, b) 5 minutes of electrolysis time, c) the histogram of the produced nanoparticles at 90 seconds of electrolysis. The average is $100\,nm$ and the nanocubes size range from $20\,nm$ to $150\,nm$, d) the histogram of the produced nanoparticles at five minutes of electrolysis. There are two peaks, first peak is centered around $100\,nm$, and the second peak is centered around $300\,nm$, and nanocubes size range from $50\,nm$ to $400\,nm$. The nanoparticles shown inside the dashed square regions are used in simulations for calculating the electric field distributions and the surface plasmon resonances (see text).

where I_{SERS}, I_{ref}, C_{ref} and C_{SERS} correspond to recorded Raman signal intensity with the SERS substrate, intensity of the reference Raman signal, concentration of the reference sample, and concentration of the SERS sample respectively. Reference recording was performed with a new copper anode before the electrolysis, and after that copper electrode is cleaned and electrolysis is performed with lower RhB concentration. Experiments are performed with utmost attention to prevent left over contamination over the anode. In addition, we also made SERS measurements after replacing the anode altogether that is used for the reference measurements, and the results did not change.

In order to obtain the optimum required time for electrolysis -to find the maximum *EF*- we recorded the Raman spectrum at various electrolysis times. The recorded spectrums from the anode electrode surface and also the variation of *EF* for the 1509 cm^{-1} Raman peak of RhB is shown in Fig. 6.5. As it is clear from this figure, even for 30 seconds of electrolysis time the anode surface can function as a SERS active substrate. The maximum *EF*, roughly 1.5×10^5, occurred at 90 seconds into the electrolysis then it started to reduce gradually, which after 5 minutes of electrolysis time the *EF* decreased to almost 75% of the maximum.

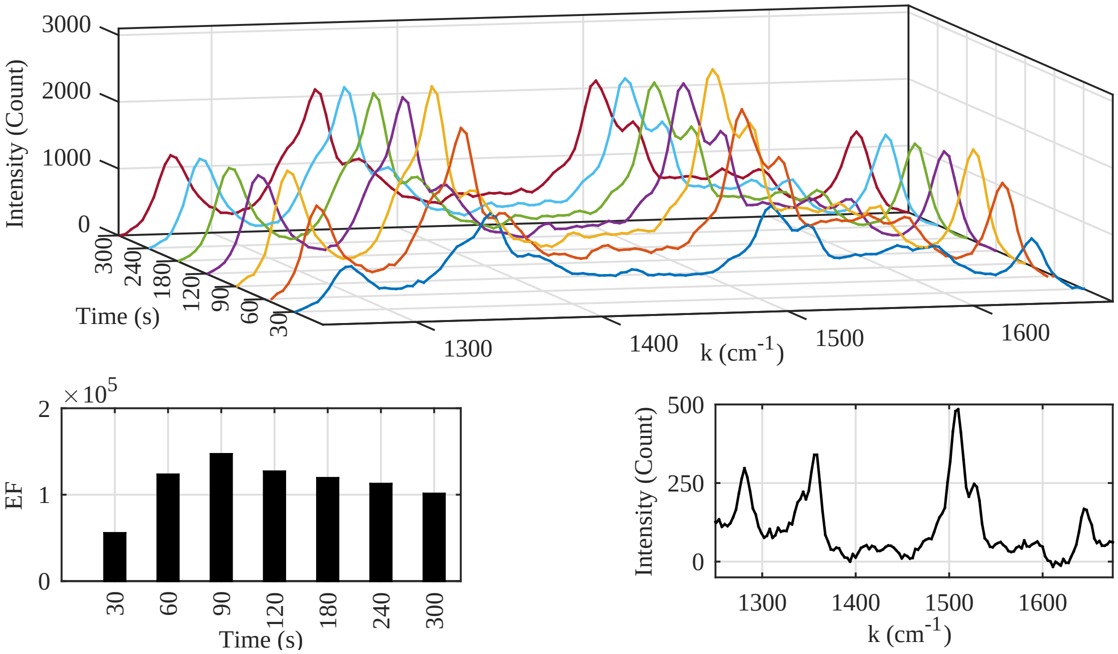

Figure 6.5: Enhancement factor (EF) of $5\mu M$ RhB variation for different electrolysis time. For electrolysis time of 90 seconds the EF for the Raman peaks of 1509 cm^{-1} reaches the maximum value of above 5 orders of magnitude. All of the spectrums were recorded in one second with laser power of $250mW$, and the reference spectrum was recorded with 100 mM RhB concentration.

This reduction in *EF* can be explained by the change in the dimensions of the nanoparticles on the anode surface. According to captured SEM images (see Fig. 6.4) from the anode surface, for 90 seconds electrolysis the average size of nanocubes is about 100 nm, while by increasing the electrolysis time to 5 minutes, the average size of the larger nanoparticles reaches to about $300\,nm$. Therefore a peak in EF is expected, as it will be explained in the discussion section, maximum enhancement should occur for surface plasmon resonance (SPR) wavelengths around $838\,nm$ which corresponds to a nanoparticle size of about $100\,nm$. After 5 minutes of electrolysis there is still a group of $100\,nm$ nanoparticles left but their number is smaller since some of them grew to larger sizes, therefore a decrease in EF is expected.

Although the nanoparticles on the anode is responsible for the SERS enhancement, there must be some nanoparticles in the electrolyte as well. However those nanoparticles are expected to be in negligible quantities and too small of size (tens of nanometer in size) as will be discussed later, they would not contribute to the Raman enhancement. For confirmation of this fact we also performed EF measurements offline, meaning that RhB solution is applied over the anode electrode after it was removed from the cuvette, and we still obtained similar above five orders of magnitude enhancement of Raman signals.

6.3 Substrate Uniformity

The substrate EF uniformity for the Raman peak of $1509\,cm^{-1}$ was checked by measuring the EF on eight random spots through a roughly $1\,cm^2$ area of the anode surface after 90 seconds electrolysis. The EF variation through these spots had a relative standard deviation(RSD) of roughly 12 percent, and the spectrums and the EF factors of these spots are shown in Fig. 6.6. A uniform EF was expected from the surface since the current density over the anode surface is rather uniform due to our electrode placement, which leads to uniform nanoparticle production on the anode. Simulated current distribution in the cuvette is also shown in the same figure.

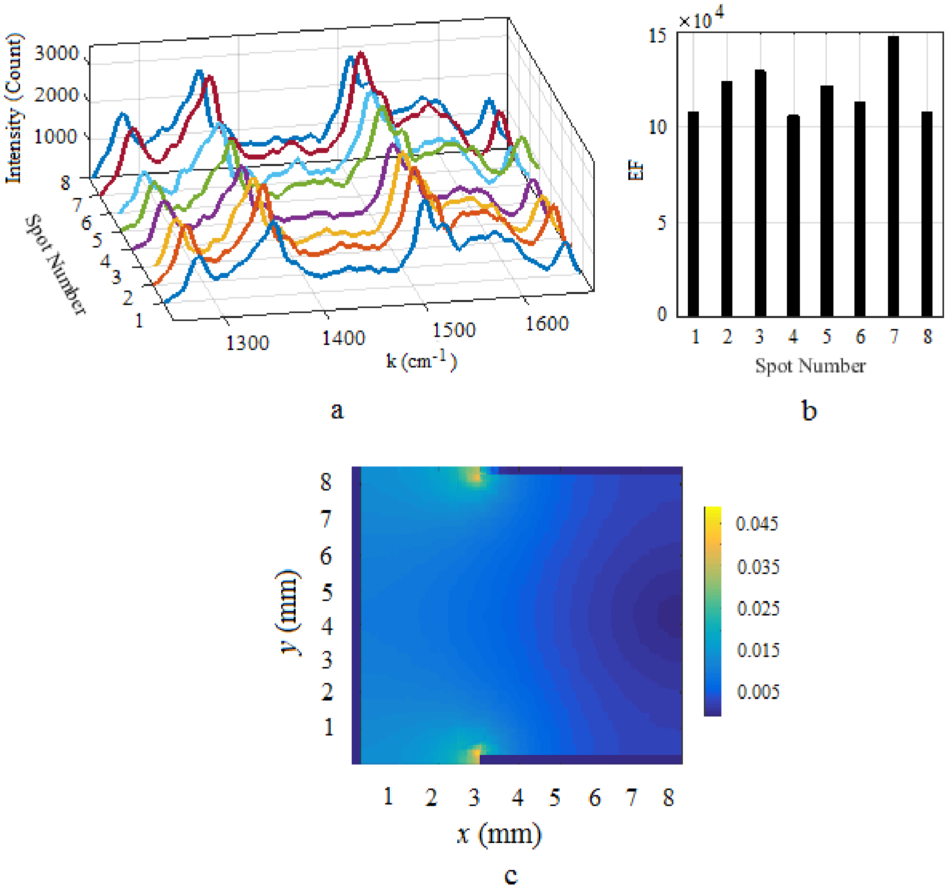

Figure 6.6: Left: The recorded Raman spectrum from eight random spots on the Cu substrate. Middle: Comparison of EF through these spots. Calculated RSD of the EF variation for the Raman peak of $1509\,cm^{-1}$ is 12 percent. The spectrums were recorded with 90 seconds of electrolysis time and RhB of concentration of $5\,\mu M$. Right: Simulated current distribution over the cross section of the cuvette. Anode is indicated with solid thick line at at $x = 0$.

6.4 Silver, Aluminum, Zinc and Brass as the SERS Substrates

We repeated similar electrolysis experiments with other metal electrodes including brass, Ag, Zn and Al which except brass, no Raman enhancement obtained. The recorded Raman spectrum from the anode surface of these metals are shown in Fig. 6.7. Enhancement from brass is understandable since it is an alloy of Cu and Zn. The obtained Raman signal from the brass anode surface is similar to that of copper, while for silver, zinc and aluminum no Raman peak is observed. The electrolysis time for these metals were even increased up to 10 minutes but still no enhancement observed. We have also inspected surfaces of anodes made of Ag, Al, and Zn with SEM and has not observed any nanoparticles.

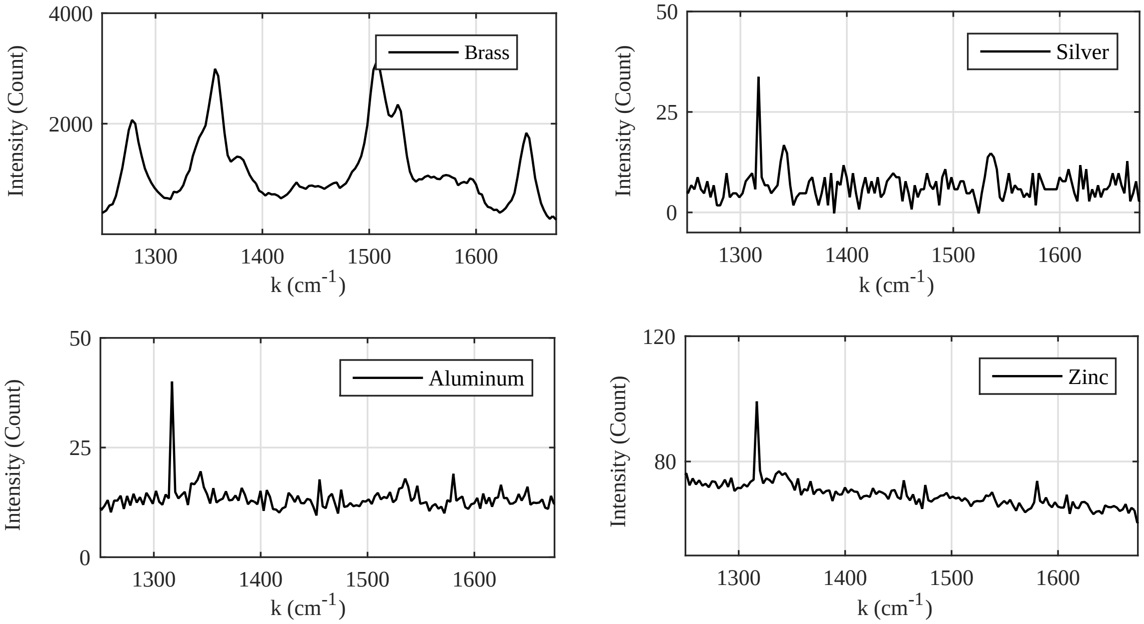

Figure 6.7: The recorded Raman spectrum from the anode surface brass, silver, aluminum and zinc while doing the electrolysis. The applied voltage is $32\,VDC$

Brass

As already mentioned, we did the same experiments as copper but with brass electrodes to study the real time SERS capability of this metal as well. In this experiment, as we expected, we observed almost similar enhancement factor to copper case; the recorded Raman spectrum is shown in Fig. 6.8. In this case, we think that the SERS enhancement comes from the formation of copper oxide nanoparticles. There are number of reasons to support this view:

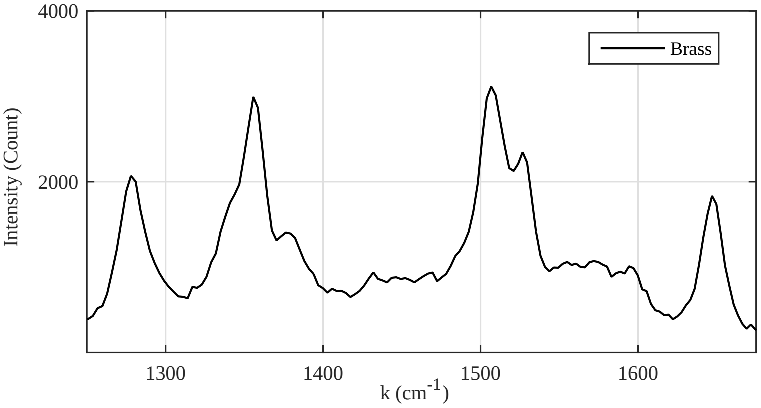

Figure 6.8: The measured Raman spectrum of Rhodamine B of $5\,\mu M$, from the brass anode surface which is practically the same as obtained from pure Cu anode..

First of all, when we replace the copper electrodes with pure zinc electrodes no Raman enhancement is observed.

Second, again with brass, Raman measurement from the anode surface during the electrolysis shows the presence of only CuO Raman peak ($290\,cm^{-1}$) and no ZnO Raman peaks (for example, $434\,cm^{-1}$ and $500\,cm^{-1}$) as shown in Fig. 6.9.

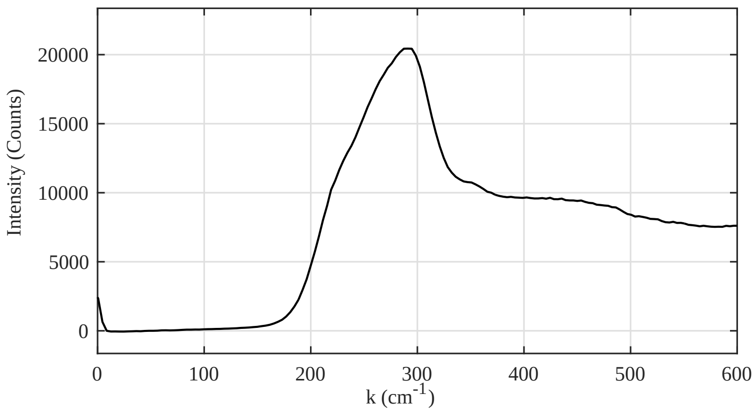

Figure 6.9: The recorded Raman spectrum from the brass anode surface shows the Raman peak of CuO at $290\,cm^{-1}$. Raman peaks of ZnO ($434\,cm^{-1}$ and $500\,cm^{-1}$) do not show up.

Third, we performed another experiment to supports this view. We used a brass anode and a stainless steel cathode in our electrolysis chamber (up-to 15 minutes). By this experiment we wanted to check if the ratio of the Cu and Zn atoms deposited on the cathode is similar to that of them in the original brass (70% to 30%, a ratio of 2.33).

The EDS measurements on the cathode (stainless-steel) show that Cu to Zn ratio ranges from 1.49 to 1.91 in 4 different areas indicating that much more Zn than Cu is deposited on the cathode. Each measurement was roughly on a $3\,mm^2$ area so that measurements were average of relatively large area. The EDS results are presented in Fig. 6.10. With the results of this experiment we can say that Zn is most likely to reach the cathode than the Cu, and/or, there is less copper on the cathode since they are used for CuO production on the anode and/or in the electrolyte.

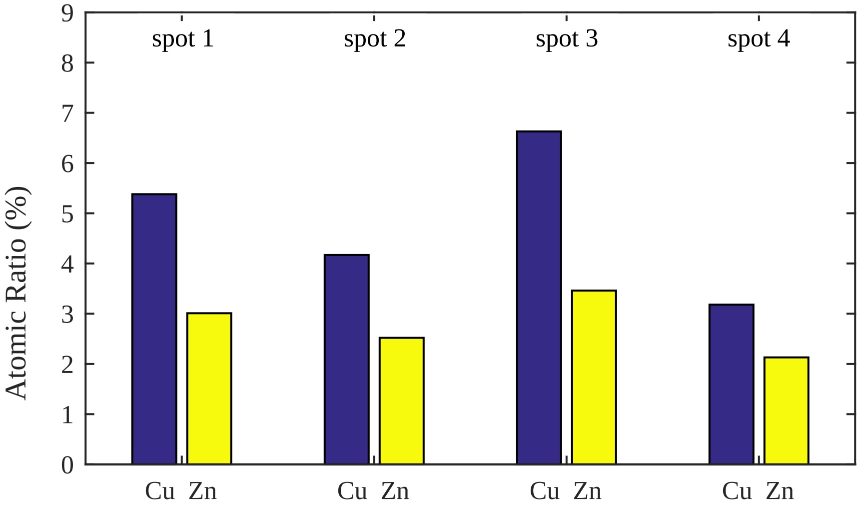

Figure 6.10: EDS measurement results: Elements on the cathode with a brass anode and a stainless steel cathode after 15 minutes of electrolysis. The elements of stainless-steel are not shown here to prevent cluttering.

Fourth, a new experiment was performed with a brass anode and cathode with stainless-steel plate at the bottom of the electrolysis chamber (see Fig. 6.11). This stainless-steel plate was electrically isolated -except the electrolyte- from the anode and cathode and its main function was to collect the nanoparticles falling from the anode (anode and cathode are in vertical position as already shown). After 15 minutes of electrolysis, brass anode electrode is shaken to cause more nanoparticles to fall on this stainless-steel plate. After carefully drying the electrolyte this stainless-steel plate was subjected to EDS measurement. The EDS elemental and mapping results showed formation of copper oxide nanoparticles but not zinc oxide anoparticles as shown in Fig. 6.12 below. As it is clear from these data, a tiny amount of zinc atoms are fallen on the stainless steel which are the zinc atoms suspended inside the electrolyte.

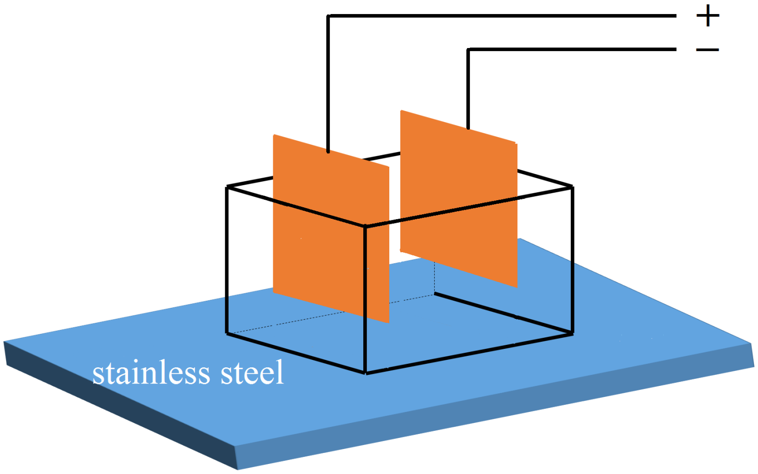

Figure 6.11: Brass as the anode and cathode with stainless-steel plate at the bottom of the electrolysis chamber. The stainless-steel plate is electrically isolated -except the electrolyte- from the anode and cathode.

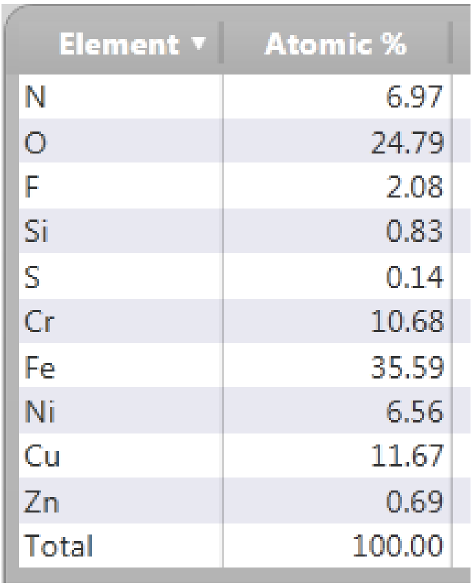

Element ▾	Atomic %
N	6.97
O	24.79
F	2.08
Si	0.83
S	0.14
Cr	10.68
Fe	35.59
Ni	6.56
Cu	11.67
Zn	0.69
Total	100.00

Figure 6.12: Brass anode electrode fall-out nanoparticle EDS data.

The EDS mapping images also were taken from the nanoparticles fell on the stainless steel. The obtained results also confirm that indeed the formed nanoparticles are copper oxide but not zinc oxide. The mapping images are shown in Fig. 6.13 - Fig. 6.16.

Figure 6.13: Brass anode electrode fall-out nanoparticle EDS layered image.

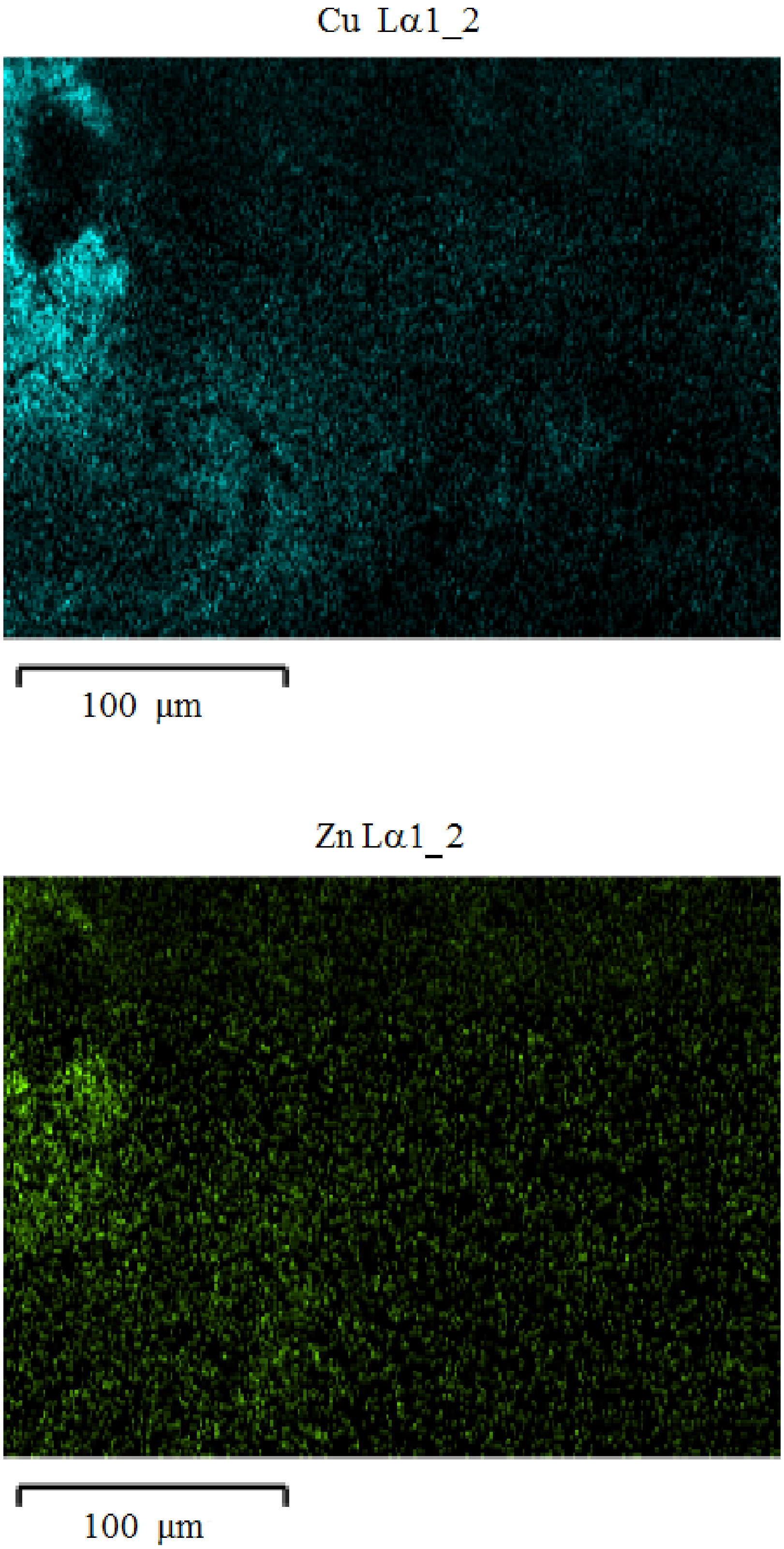

Figure 6.14: Brass anode electrode fall-out nanoparticle EDS mapping images of copper and zinc atoms. The ratio of copper to zinc is 95% to 5%.

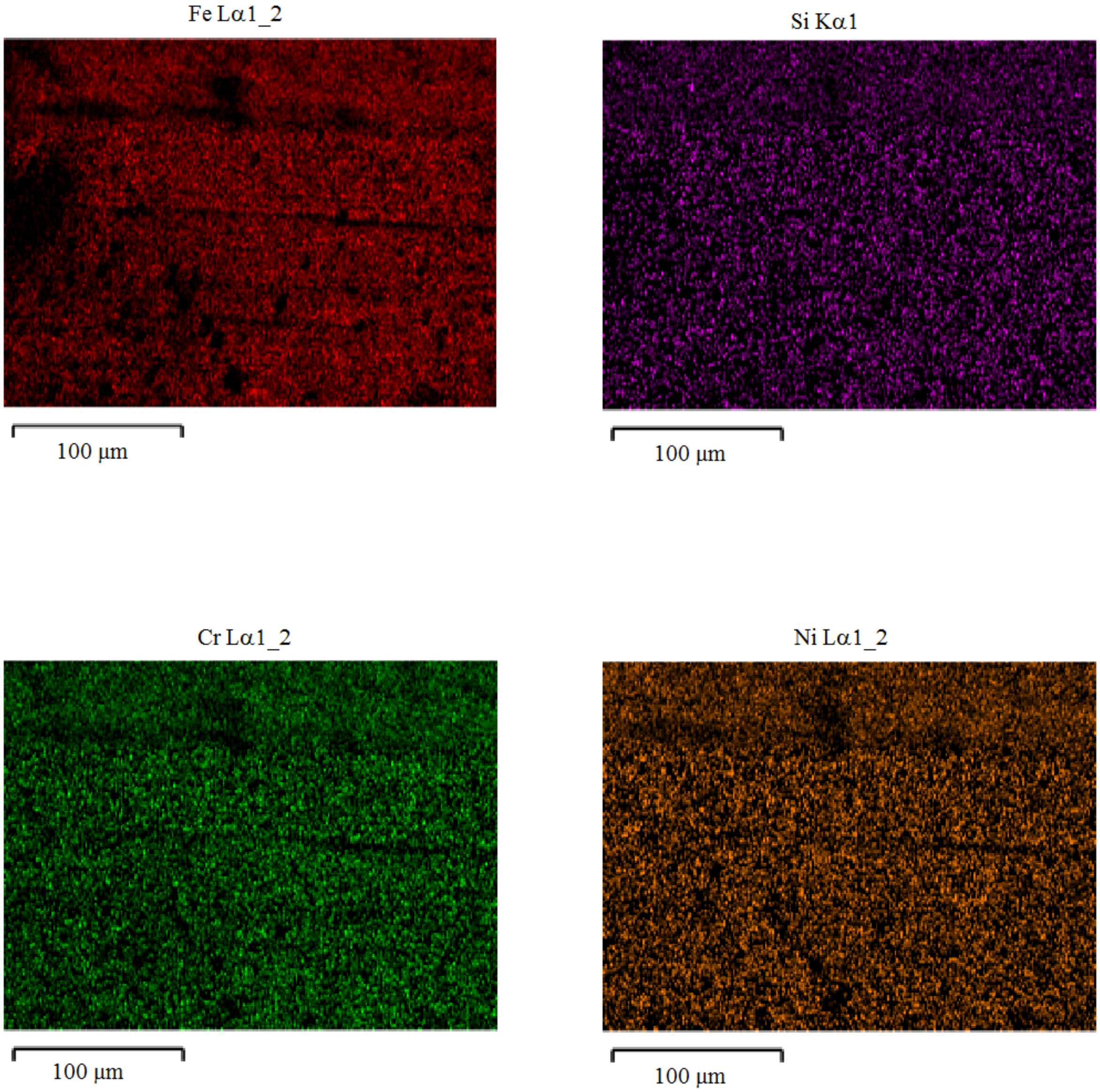

Figure 6.15: Brass anode electrode fall-out nanoparticle EDS mapping images of Fe, Si, Ni and Cr atoms. These are the atoms of the stainless steel.

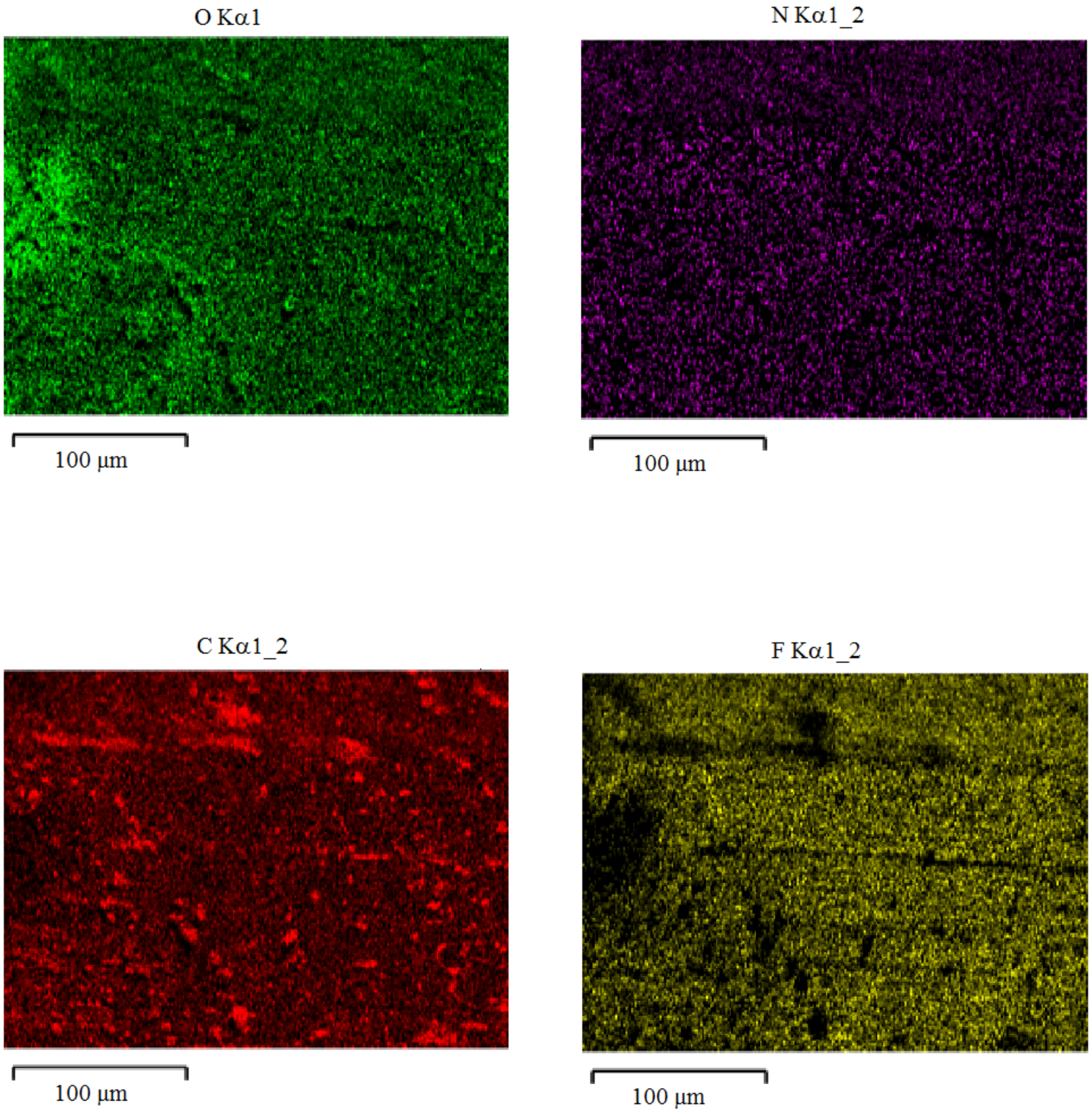

Figure 6.16: Brass anode electrode fall-out nanoparticle EDS mapping images of oxygen, carbon, nitrogen and fluorine atoms. Carbon atoms appear due to contamination in the EDS chamber.

In a nutshell

- The EDS mapping results which show a tiny amount of zinc atoms (5 percent compared to copper atoms) is found at the bottom of the container,
- With brass electrodes Raman peaks of CuO present but no ZnO peaks,
- With pure Zn electrodes no Raman peaks of ZnO is observed,
- The ratio of copper to zinc on the stainless-steel cathode surface is found to be less than the copper to zinc ratio of brass which indicates that more Zn atoms move to cathode and reduced there. We can also conclude that less Cu atoms move toward the cathode and reduce there, therefore some of the copper atoms get oxidized on the anode surface,
- Even with pure Zn anode there were not any nanoparticles produced on the anode surface. Hence no ZnO formation, therefore it is not surprising not to observe any ZnO formation with brass,

prove that indeed the enhancement of Raman signal from brass surface is due to copper oxide nanoparticles and not from zinc oxide nanoparticles.

Silver

We repeated the same experiments as copper but with silver electrodes to study the real time SERS capability of this metal as well. In this case, we were not able to record the Raman spectrum of RhB of $5\,\mu M$ concentration, which means silver cannot be used as a real time SERS substrate. During the experiment the silver nanoparticles (not silver oxide) of roughly $10\,nm$ (after 10 minutes electrolysis) are formed. When the formed silver nanoparticles are very small in dimension, say in the range of $10nm$, they will show surface Plasmon resonance in the UV range. Since we have used a near infrared laser source ($785\,nm$), the produced nanoparticles cannot be used as a SERS active substrate in this range. Also, UV sources are not appropriate for Raman measurements due to high fluorescence noise in this region.
In order to characterize the silver nanoparticles, after 10 minutes of electrolysis, we dried the electrolyte on a microscope slide, then measured its EDS signal. The EDS results in Fig. 6.17 shows the elements in three different areas of the microscope slide. In all areas the ratio of silver to oxygen confirms the formation of silver nanoparticles, perhaps with negligible amount of silver oxide.

We performed an XRD analysis of the produced silver nanoparticles as well. The XRD pattern we obtained is shown in Fig. 6.18 also confirms the production of silver nanoparticles of size of $10\,nm - 15\,nm$. More specifically, we calculate the average nanoparticles size according to Scherrer equation:

$$D = \frac{0.9\lambda}{\beta_{\frac{1}{2}}\cos(\theta)} \tag{6.1}$$

where, $D\,, \beta\,, \theta$ and λ are the average crystallite size, line broadening in radians, Bragg angle and X-ray wavelength respectively. For the calculation we have used the following values for the parameters:
$\lambda = 1.5418\,A^\circ$
$\beta_{\frac{1}{2}} = 0.01\,rad$

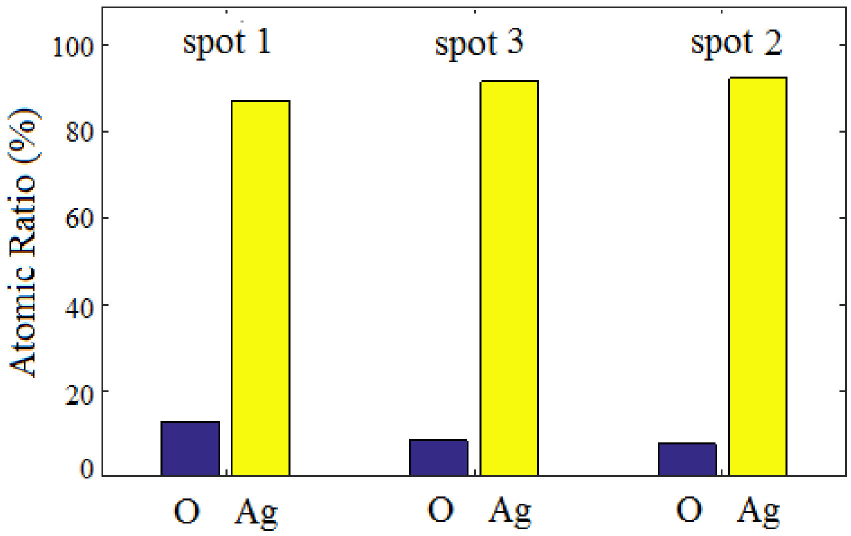

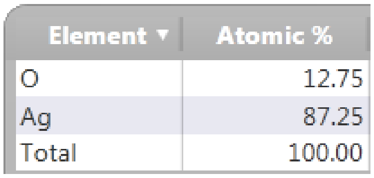

Element ▾	Atomic %
O	12.75
Ag	87.25
Total	100.00

1

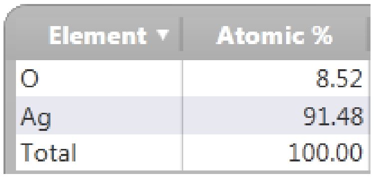

Element ▾	Atomic %
O	8.52
Ag	91.48
Total	100.00

2

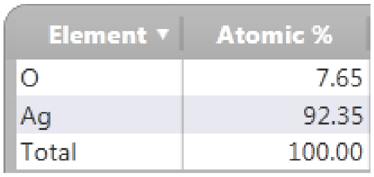

Element ▾	Atomic %
O	7.65
Ag	92.35
Total	100.00

3

Figure 6.17: The EDS element analysis of the produced nanoparticles during 10 minutes electrolysis with silver electrodes.

In addition, the SEM image in Fig. 6.19 of the silver anode surface confirms the production of nanoparticles in the range of $10\,nm - 15\,nm$.

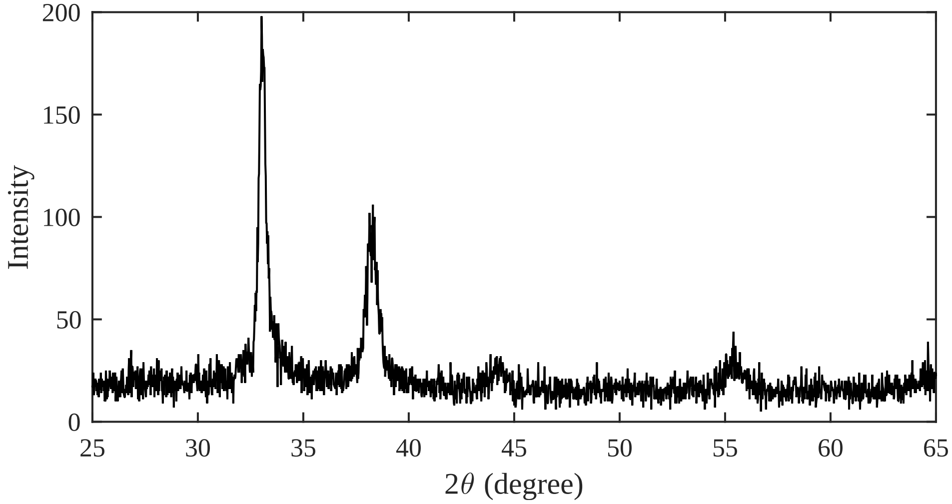

Figure 6.18: XRD pattern of the silver nanoparticles dried on a microscope slide.

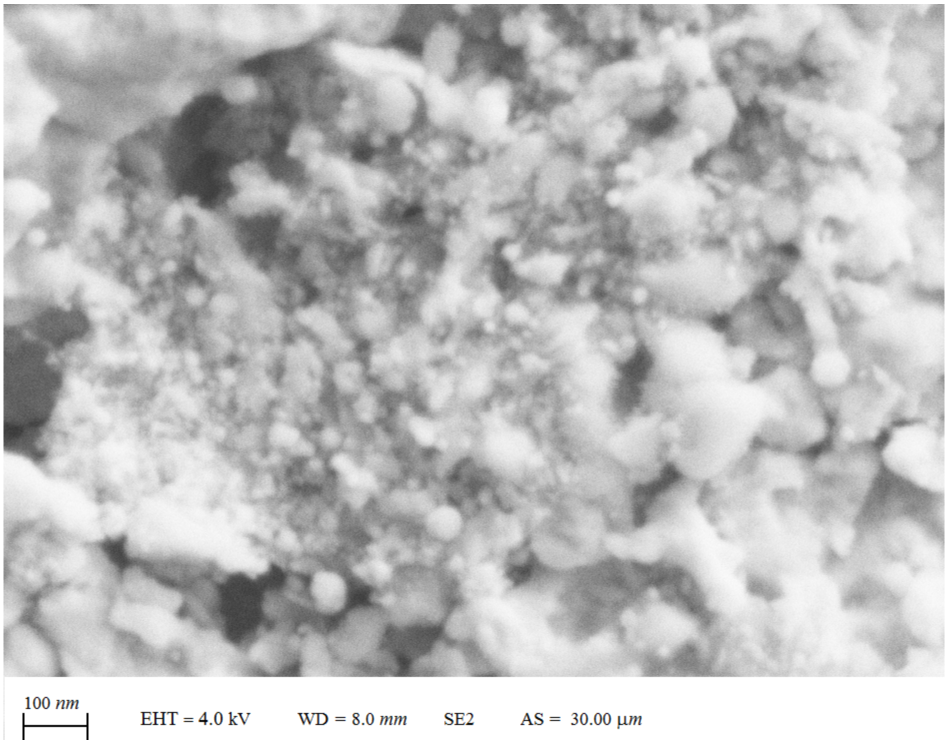

Figure 6.19: SEM image from the silver anode surface after 10 minutes electrolysis with $32\,V\ DC$ signal.

6.5 Crystal Violet SERS Signal

SERS experiments were repeated with solutions of crystal violet (CV) which is widely used as a histological stain, particularly in Gram staining for bacteria classification, and as the Fig. 6.20 shows the Raman peaks are enhanced again for more than 10^5 times. In this experiment we have used copper plates as the electrodes and done the electrolysis experiment with 32 V DC signal for three minutes. The Raman peak of CV at 1175 cm^{-1} is enhanced 1.75×10^5.

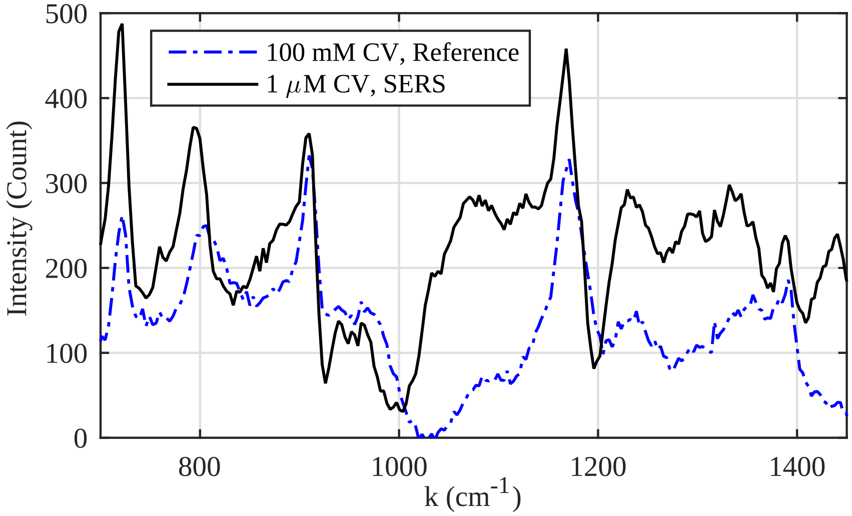

Figure 6.20: SERS Enhancement of crystal violet (CV) solution: $1\mu M$ crystal violet solution on Cu anode after 3 minutes of electrolysis compared to $100\,mM$ reference Raman measurement. All recordings were done in 1 sec with 250 mW of laser power. For example, the Raman peak of CV at $1175\,cm^{-1}$ is enhanced for more than 10^5.

6.6 Effect of Electrolysis Voltage

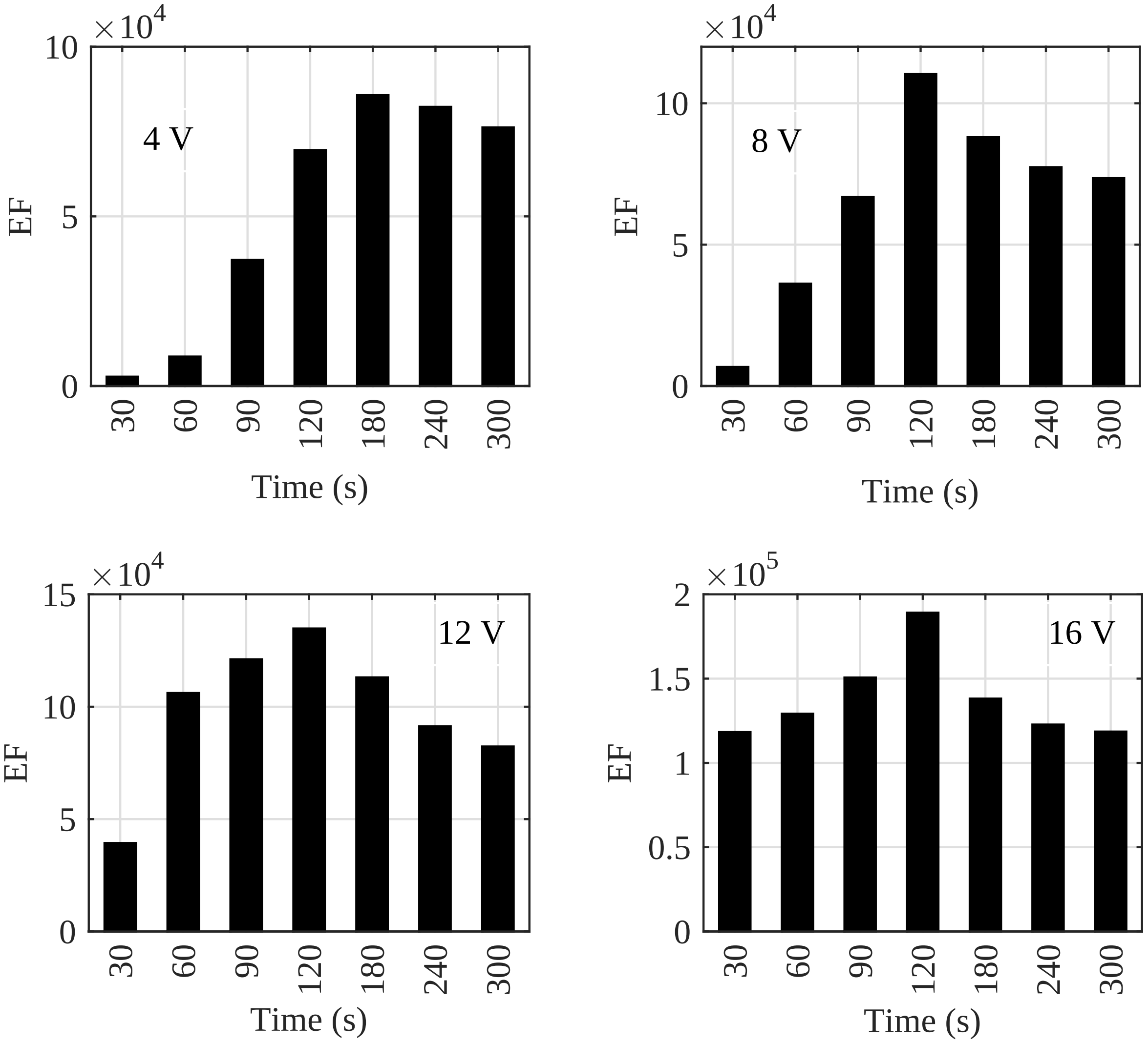

Figure 6.21: SERS enhancement factor (EF) versus time at different electrolysis voltages. The electrode and electrolyte are copper and RhB of $5\,\mu m$ respectively. The experiments are done with 4, 8, 12 and 16 volts as indicated on the figures.

The effect of electrolysis voltage on enhancement factor as well as the time at which the maximum EF occurs are investigated here. As the previous experiments these experiments also were done with copper electrodes and Rhodamine B of $5\,\mu m$.

Reducing the voltage value to 16 volts we obtained maximum EF of 1.9×10^5 at two minutes. Decreasing the voltage to 12 and 8 volts, the maximum EF reduced to 1.4×10^5 and 1.1×10^5 but still we obtained maximum enhancement at two minutes electrolysis. We reduced voltage down to 4 volts, which the maximum EF went below five orders of magnitude and also the time at which this maximum EF occur increased to three minutes. It seems reducing the voltage below 10 volts (tested for 4 and 8 volts), the maximum EF reduces and the corresponding time increases. However, to get a conclusive result about the optimum voltage for the maximum EF we need a large range of voltage sweep as well as theoretical calculations and estimations. Specially, we need to carry out the experiments with voltage below and above 32 volts as here, we did not do for voltages above 32 volts.

We think the reduction in EF with voltage below 10 volts is due to decrement of nanoparticle density on the anode surface. Decreasing the voltage, the current density (injected electrons from the external source) is diminishes and since the nanoparticle density is directly proportional to the injected electrons from the external source, the nanoparticle density on the anode surface decreases.

Also the increment in the time at which the maximum EF occurs is due to reduction of injected electrons from the external source. Because, as time passes more electrons enter the system, hence more nanoparticles are produced.

6.7 Discussions

6.7.1 Characterization of Nanoparticles

A traditional way to prove the existence of copper oxide is X-Ray diffractometry (XRD) technique but here we could not use this technique since the nanoparticles are produced on the copper surface, and the amount of signal from the copper plate overwhelms the signals emanating from the nanoparticles. Therefore, in order to determine whether the nanoparticles are copper or copper oxide, following experiment is performed: while the electrolysis is in progress, copper anode was subjected to Raman spectrum measurement. Back scattered Raman spectrum from the copper anode surface was recorded and it clearly showed the Raman peaks of CuO nanoparticles at $290\,cm^{-1}$. Furthermore, this Raman peak intensity changes over the electrolysis time in a similar fashion to the experiment done with RhB experiments which we can conclude that indeed resultant Raman signal is from the forming CuO nanoparticles.

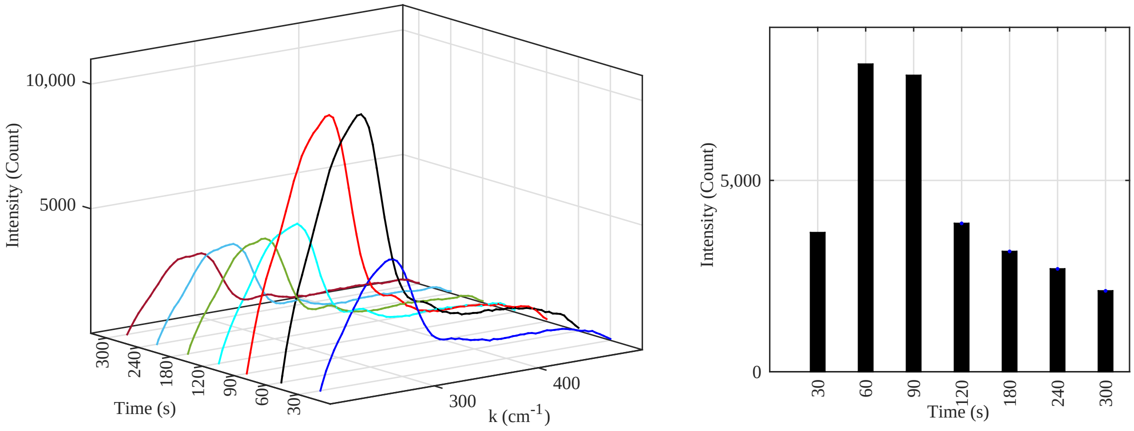

Figure 6.22: The recorded Raman spectrums from the anode surface at different electrolysis times which show a peak at $290\,cm^{-1}$. The electrolyte was just the ultra-pure water, and the peak intensity changes in a similar pattern as a function of electrolysis time as the Raman measurements done with RhB. This measurement confirms that the nanoparticles are indeed CuO particles.

Another point to note that CuO maximum peak occurs at 60 seconds electrolysis as shown in Fig. 6.22, while the maximum EF with RhB happens at 90 seconds electrolysis time. This is expected since the Raman peak of CuO at $290\,cm^{-1}$ is closer the laser wavelength than the Raman peak of RhB at $1509\,cm^{-1}$, which means that nanoparticle size should be smaller for the SPR enhancement in this case. The intensity of Raman peak of CuO at $290\,cm^{-1}$ is also decreasing after 90 seconds electrolysis as the case measurement with of RhB indicating that the nanocubes are growing in size.

The similar experiment was done during the experiment with brass electrodes which is already explained. The recorded Raman spectrum from anode surface of brass shows Raman peak at $290\,cm^{-1}$ which corresponds to copper oxide Raman line. The absence of Raman peaks at $434\,cm^{-1}$ and $500\,cm^{-1}$ prove the absence of zinc oxide nanoparticles in the electrolysis experiment with brass electrodes.

In the electrolysis experiment with other metals (zinc, silver and aluminum), the recorded Raman spectrums do not show any Raman line correspond to the oxide of these metals. The absence of their Raman line means no metal oxide was formed during the electrolysis.

6.7.2 Nanoparticle Synthesis

In an electrochemical cell, when a voltage is applied between the anode and cathode, electrons are removed from the anode and they are replaced from the cathode. Metal ions are extracted from the anode (cations) and migrate to cathode where the reduction takes place and metallic clusters form. When a metal salt is used in the electrolyte such as copper sulphate ($CuSO_4$) in the case of copper nanoparticle production with copper anode, due to ionization, $CuSO_4$ is dissociated into Cu^{2+} and SO_4^{2-} ions. The current is carried by Cu^{2+} and SO_4^{2-} in the solution, and Cu^{2+} ions move towards the cathode. Some of those cations get reduced in the electrolyte, the remaining ones arrive to cathode and they get reduced to Cu atoms and deposited on the cathode. The metallic clusters are formed over time and this process takes hours to days and the size of nanoparticles produced are on the order of tens of nanometers to hundred nanometers range [102,103]. Therefore in matter of minutes the size of produced nanoparticles would be too small to be suitable for SERS applications as the surface plasmon resonance frequencies would be towards the UV range and would not be applicable for Raman spectrum measurements.

In contrast to those studies, when we performed electrolysis with copper anode in ultra-pure water we observed copper oxide nanoparticles over the anode surface in matter of minutes at the sizes of up-to $400\,nm$. When the anode material is copper we contemplate the following reactions to occur on the surface:

$$\begin{gathered}
\mathrm{H_2O} \rightarrow \mathrm{H^+} + \mathrm{OH^-} \\
\mathrm{Cu} \rightarrow \mathrm{Cu^{2+}} + 2\mathrm{e^{-1}} \\
2\mathrm{H^+} + 2\mathrm{e^{-1}} \rightarrow \mathrm{H_2} \\
\mathrm{Cu^{2+}} + 2\mathrm{OH^-} \rightarrow \mathrm{CuO} + \mathrm{H_2O}
\end{gathered}$$

Some of the oxidized copper atoms remain attached to surface and combine with OH^- to form CuO and start the crystallization to form the nanoparticle in cubic form. There should be copper cations moving towards the cathode and reduced on the way, or at the cathode but their cluster size must be negligible in size because of the short of amount of electrolysis time. When the experiments are repeated for anodes made of other metals such as brass, Al, Zn, and Ag, except brass, no nanoparticles on the anode is observed during the electrolysis times for up-to ten minutes. The cations from the anode are in competition with H^+ to gain the electrons, hence for the reduction to form the relevant atoms or their oxides on the anode, and the electrode potential will determine which cation will win the competition. According to electrode potentials listed below:

Reaction	Electrode Potential (V)
$Al^{3+} + 3e^- \rightarrow Al$	-1.66 V
$Zn^{2+} + 2e^- \rightarrow Zn$	-0.76 V
$2H^+ + 2e^- \rightarrow H_2$	0.00 V
$Cu^{2+} + e^- \rightarrow Cu^+$	0.15 V
$Cu^{2+} + 2e^- \rightarrow Cu$	0.34 V
$Ag^+ + 1e^- \rightarrow Ag$	0.8 V

copper cations have much more tendency to get reduced compared to hydrogen (H^+), therefore, more copper cations will gain electrons in competition with H^+. However, considering the aluminum and zinc cations, hydrogen has more reduction tendency in comparison, hence, they will fail to gain electrons and get reduced to produce enough metal atoms and/or metal oxide nanoparticles especially in such short electrolysis times. For the silver, electrode potential is much bigger than that of the hydrogen, hence much more silver atoms and consequently nanoparticles (compared to copper) were produced inside the liquid during the experiment but the lower tendency of silver for oxidation limits silver oxide nanoparticle growth on the anode surface in short time. Also, the silver nanoparticles in the electrolyte must be in too small of a size and/or small number of quantity to contribute to the real-time Raman signal enhancement in experiments performed.

An important to note that in the case of brass, although, Zn loses electrons easier than Cu (hence oxidizes faster), however in order to obtain ZnO or CuO, Zn and Cu ions have to be reduced. In that case Cu ions wins the competition (since oxidation and reduction potentials are opposite of each other). Besides Cu ions, electron capture rate of H^+ is also higher than Zn ions. Therefore, when H2O forms H^+ and OH^-, the oxygen from OH^- reduces the Cu ions to form CuO. Then Zn ions must travel toward the cathode and they get reduced there.

6.7.3 Surface Plasmon Resonance Simulations

When a metal nanostructure is exposed to an electric field of amplitude E_0 and frequency of ω, at some frequencies the electric field around the nanosphere (called local electric field) is enhanced as depicted in Fig.6.23. The enhancement of local electric field is due to excitation of surface Plasmons which are non-propagating excitation of the conduction electrons coupled to the incident field [113].

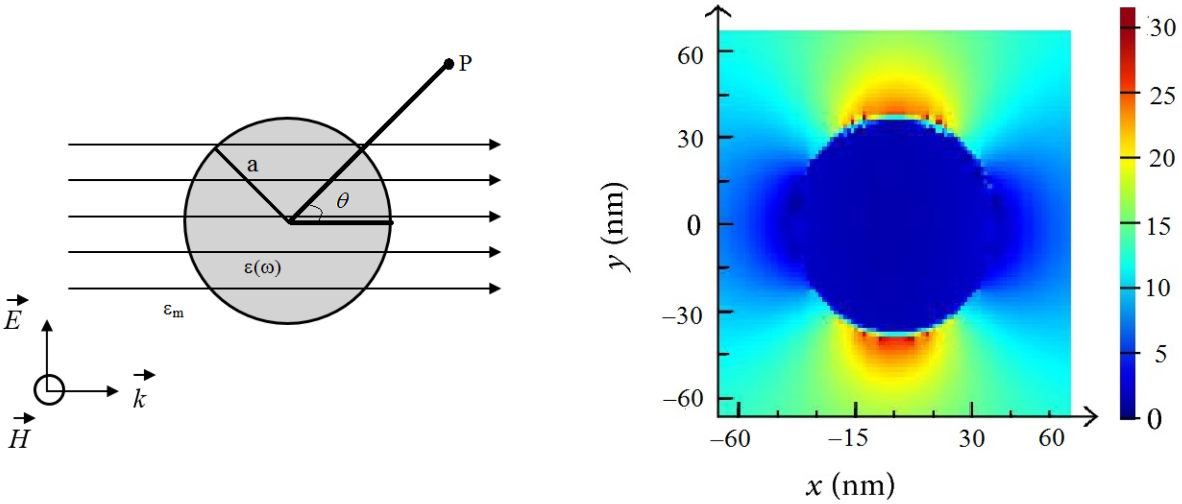

Figure 6.23: Electric field distribution around a metal nanosphere. There is electric field enhancement in the vicinity of the nanosphere called local field enhancement.

For instance, lets assume a metal nanosphere of radius a and permittivity of $\epsilon(\omega)$ embedded in a host material of permittivity ϵ_m. We also assume this nanosphere is subject to an external electric field of amplitude E_0. The electric field inside and outside of the nanosphere can be calculated by solving the Laplace equation for the potential, $\nabla^2\phi = 0$, under the boundary conditions of the metal nanosphere. Solving this equation the potential inside and outside the metal nanosphere are calculated as follows:

$$\begin{aligned} \phi_{in} &= \frac{-3\epsilon_m}{\epsilon + 2\epsilon_m} E_0 r \cos\theta \\ \phi_{out} &= -E_0 r \cos\theta + \frac{\epsilon - \epsilon_m}{\epsilon + 2\epsilon_m} E_0 a^3 \frac{\cos\theta}{r^2} \end{aligned} \tag{6.2}$$

where r is the distance from the sphere center. Electric field can be calculated according to $E = -\nabla\phi$.

If we note, ϕ_{out} in Eq. 6.2 is composed of two parts; incident field and the field of a dipole located at the center of the particle. Therefore, in terms of dipole moment (p), ϕ_{out} can be written as follows:

$$\phi_{out} = -E_0 r\cos\theta + \frac{\vec{p}.\vec{r}}{4\pi\epsilon_0\epsilon_m r^3} \tag{6.3}$$

where $\vec{p} = 4\pi\epsilon_0\epsilon_m a^3 \dfrac{\epsilon - \epsilon_m}{\epsilon + 2\epsilon_m}\vec{E}_0$.

Considering Eq. 6.3 we can conclude that the incident field induces a dipole moment inside the nanosphere. The amplitude of the induced dipole is directly proportional to the amplitude of the incident field as well as the third power of the nanosphere radius. Another important to note is $(\epsilon(\omega) + 2\epsilon_m)$ which, since in the metals $\epsilon(\omega)$ is a complex and frequency dependent parameter, we can find the frequencies in which $|\epsilon(\omega) + 2\epsilon_m| = \text{minimum}$. This frequency called surface Plasmon resonance (SPR) frequency. The permittivity of metals is a complex value which can be written as $\epsilon(\omega) = \epsilon_1(\omega) + j\epsilon_2(\omega)$. Therefore the minimum value of $|\epsilon(\omega) + 2\epsilon_m)|$ occurs at $\epsilon_1(\omega) = -2\epsilon_m$.

$$(\epsilon_1(\omega) + 2\epsilon_m)^2 + \epsilon_2(\omega)^2 = \text{minimum} \rightarrow \quad \epsilon_1(\omega) = -2\epsilon_m \tag{6.4}$$

In the SPR frequency the maximum local electric field occurs, and the imaginary part of the metal permittivity ($\epsilon_2(\omega)$) determines the width and height of the resonance.

In the previous part the SPR of the single metal nanosphere is discussed. However, when the metal nanoparticles are placed in a close distance, their SPR frequencies are changed due to near field interparticle coupling effect. The near field coupling causes a red shift of resonance frequency. Nordlander et. al [114, 115] developed the plasmon hybridization method to study the optical absorption and plasmon frequencies of

nanospheres in dimer, trimer and quadrumer structures. In this method the plasmon modes of theses nanostructures are calculated as the linear combinations of the individual nanospheres. For instance, they have shown that the dimer plasmons can be considered as the bonding and anti-bonding combinations, means hybridization of the individual nanoparticle plasmons. In the plasmon hybridization method electrons are treated as charged, incompressible liquid. These electrons are assumed sitting on top of the positively charged ions.
The dependence of the plasmon modes on the interparticle distance (d) is also investigated by palsmon hybridization method. At large interparticle distance (d), the change of the dimer dipolar plasmon energies can be explained only considering the interaction between two classical dipole which is inversely proportional to the third power of the interparticle distance ($\frac{1}{d^3}$). However, at smaller d the energy shifts get stronger and also sharper change occurs which is due to interaction of higher order oscillations such as quadrupole etc.

When the number of nanoparticles are increased and/or the shape of the nanoparticles is not as simple as nanosphere, finding an analytical solution to calculate the plasmon resonance energies is impossible. Therefore, here, in this thesis the effect of nanoparticle size on the *EF* factor is investigated using finite difference time domain (FDTD) technique by calculating the surface plasmon resonance wavelength of nanoparticles. The simulation is performed first for a single nanocube of size ranging from $100\,nm$ to $400\,nm$, with cubic mesh and minimum mesh step size of $4\,nm$ and the time step size stability factor of 0.85. The calculated extinction cross sections of the nanocubes as a function of wavelength is shown in Fig. 6.24 below. As it is clear form this figure the growth in nanocubes size leads to red shift in surface plasmon resonance peaks and also produce other SPR resonance wavelengths -due to excitation of higher-order resonance modes- appearing at shorter wavelengths. The red shift in SPR causes a mismatching between the SPR peak and the excitation source wavelength used, which is the reason for *EF* having a maximum as a function of electrolysis time. However the single nanoparticle simulation is not really reflecting the reality since it does not

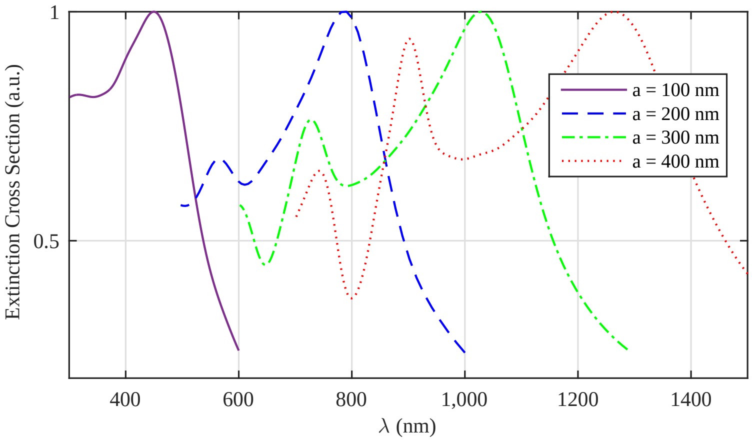

Figure 6.24: Simulated SPR of copper oxide nanocubes of different size; increasing the nanocubes size leads to red shift in SPR wavelength and also excitation of the higher order resonance modes.

include the mutual coupling effects between the nanoparticles and the substrate. Light intensity should increase in the gap between the nanoparticles and on the sharp corners and crevices, therefore a more realistic simulation is in order for calculating the field distribution and the extinction cross section. For this purpose we selected a realistic collection of particles on a copper substrate as shown with the dashed squares in Fig 6.4. For the ninety second run simulations, we selected the $1\,\mu m \times 1\,\mu m$ area shown in this figure and performed a FDTD simulations. Here we assumed nanocubes are copper oxide nanocubes of size ranging from $85\,nm$ to $150\,nm$ in accord with the particle dimensions on that selected square. Inter-particle distances were assumed to range from $10\,nm$ up to $350\,nm$ and the nanocubes were sitting on copper substrate. The electric field was assumed to propagate perpendicular to the substrate surface. The values for the refractive index, n, and the extinction coefficient, k for copper and copper oxide are taken from literature [116, 117]. The results of this simulation is shown in Fig 6.25, where the particle distribution, electric field distribution at the surface plasmon resonance of $794\,nm$, and the extinction cross section as a function of wavelength is shown.

Same simulation is repeated for larger particle distribution which is obtained by five minutes of electrolysis. In this case the simulated area was $2\,\mu m \times 2\,\mu m$, and the nanocube dimensions were ranging from $60\,nm$ to $300\,nm$ with inter particle gaps ranging from $50\,nm$ to $1000\,nm$ as estimated from Fig. 6.4. The results of this simulation

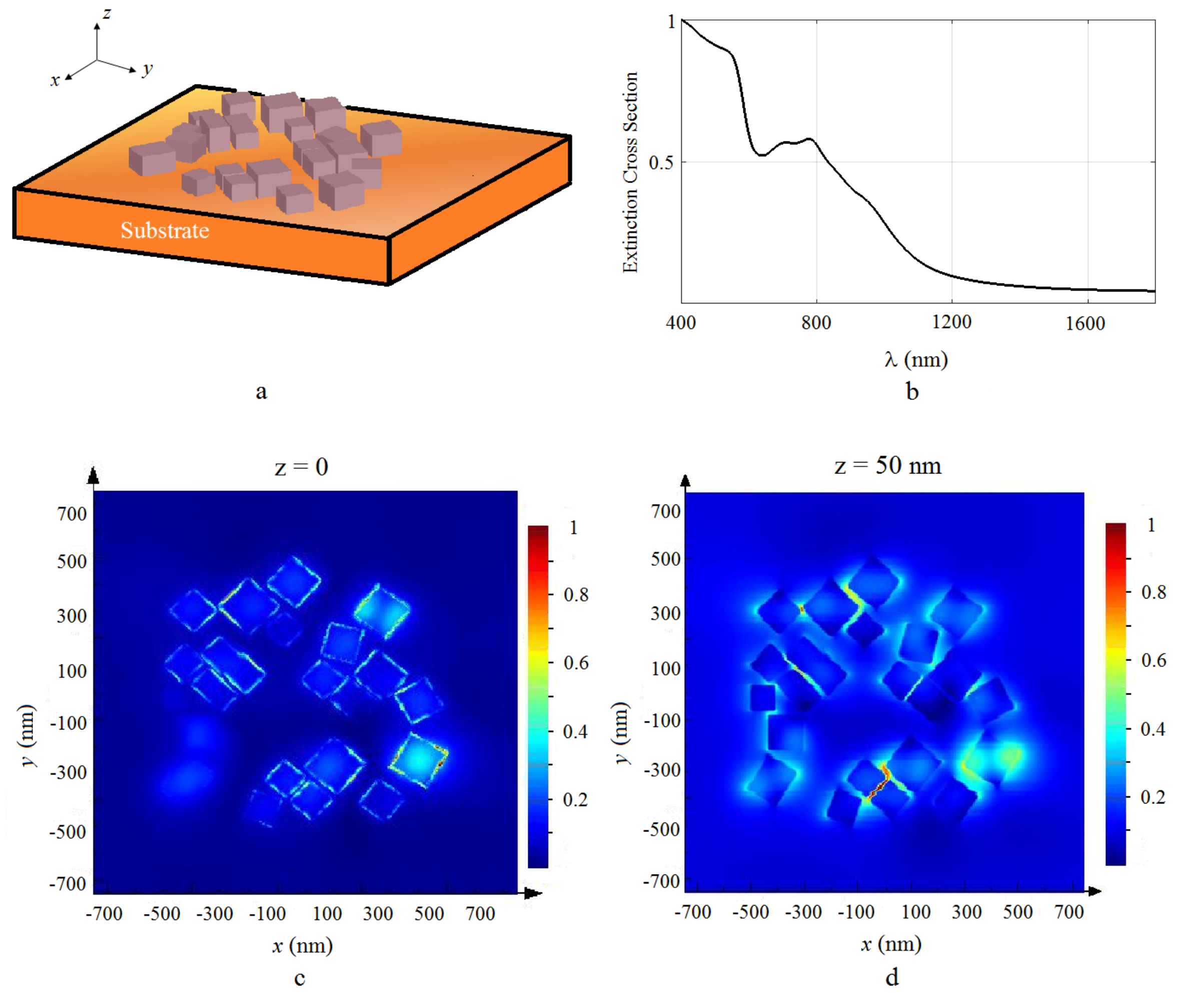

a

b

c

d

Figure 6.25: a) The simulated area is $1\,\mu m \times 1\,\mu m$ where size of copper oxide nanocubes range from 85 nm up to 150 nm, inter-particle gaps range from $10\,nm$ to $350\,nm$, b) The extinction cross section of this assembly of nanocubes as a function of wavelength, c) Electric field amplitude distribution at $0\,nm$ above the surface at SPR resonance of $794\,nm$, d) Electric field amplitude distribution at $50\,nm$ above the surface at SPR resonance of $794\,nm$.

is shown in Fig 6.26, where the particle distribution, electric field distribution at the surface plasmon resonance of $971\,nm$, and the extinction cross section as a function of wavelength is shown.

Although, according to theory the maximum SERS enhancement occurs when the substrate resonates at laser wavelength, in practice the maximum enhancement takes place when the SPR resonance occurs around the middle of the excitation wavelength and Raman scattering wavelength [118]. Since the laser source has a wavelength of $785\,nm$, the Raman peak of RhB at $1509\,cm^{-1}$ (corresponds to $891\,nm$ in terms of wave-

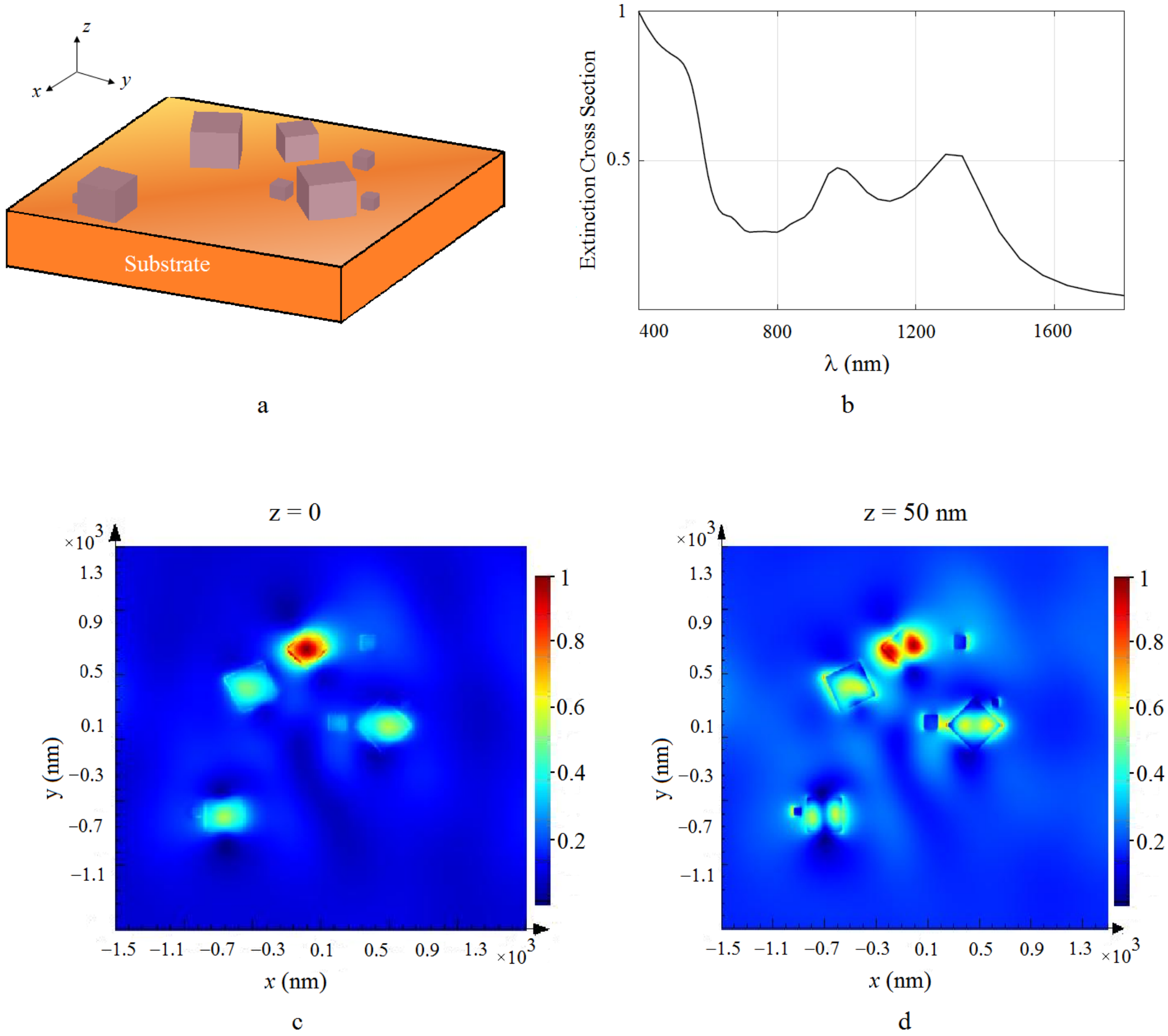

Figure 6.26: a) The simulated area is $2\,\mu m \times 2\,\mu m$ where size of copper oxide nanocubes range from $60\,nm$ up to $300\,nm$, inter-particle gaps range from $50\,nm$ to $1000\,nm$, b) The extinction cross section of this assembly of nanocubes as a function of wavelength, c) Electric field amplitude distribution at $0\,nm$ above the surface at SPR resonance of $971\,nm$, d) Electric field amplitude distribution at $50\,nm$ above the surface at SPR resonance of $971\,nm$.

length), therefore we would expect enhancement for SPR resonances around $838\,nm$. According to our simulations for a typical distribution of nanoparticles at 90 seconds, the resonance wavelength is around $794\,nm$ for average nanoparticle size of $100\,nm$ as shown in Fig 6.25. Considering that the particles are distributed randomly and the selected area produces resonances around the expected wavelengths, we can conclude that the experimental results are in good agreement with the theoretical predictions; as the SEM images in Fig. 6.4 show, the average size of nanocubes are about $100\,nm$ when the maximum EF occurs. When the electrolysis time is extended to 5 minutes the resonant wavelength is shifted to $971\,nm$ as observed from Fig 6.26. Also it is known that as the nanoparticle size grow comparable to the wavelength of excitation, the non-radiative modes are excited on the particles which diminishes the SERS enhancement factor [119]. We might also see this effect come into play for longer electrolysis times. An important to note is that as far as the SERS phenomenon is concerned usually noble metals and transition metals are used for the SERS substrates. However metal oxides are also confirmed to act as the SERS active substrate. In general it is contemplated that there is a charge transfer effect within the metal/metal oxide interface. The charge transfer allows manipulation of the localized surface Plasmon resonance and finally the Raman signal enhancement factor. In our case, we performed our simulations for copper oxide nanoparticles over a metallic surface therefore this effect is included. When the simulations are performed without metal backing there is only semiconductor/dielectric resonances of the particles and the resultant electric fields are not as high as when the copper oxide nanoparticles sitting over copper surface.

6.7.4 Substrate Roughness Effect on the EF

A legitimate question would be if the roughness created during the formation of nanoparticles on the substrate surface affect the SERS enhancement factor since the local electric field around the sharp edges is enhanced. In our experiments the effect of the substrate roughness is negligible. We have two supporting reasons for this claim:

First, During the experiment and observing the enhancement of the Raman signal, when we shake the electrode a bit, the Raman signal disappears. We think nanoparticles drop from the surface, consequently, we lose the enhancement. Therefore, if the surface roughness was the reason of the enhancement, we should have seen the enhancement after shaking the substrate as well.

Second, after the electrolysis, we remove the electrode and perform Raman measurements of say RhB, and see the enhancement. However after cleaning the substrate lightly and applying the RhB solution again produces no enhancement.

These two carried out experiments clearly proves that the obtained enhancement of Raman signal is only due to formation of copper oxide nanoparticles, and not the roughness created on the surface.

6.7.5 Comparison

In this section we compare our SERS substrate function and efficiency with commercially available SERS substrates. There are several companies producing SERS active substrates and sell them off the shelf. For example Ocean Optics Inc sells these substrates for about $80\,USD$ and have a shelf life of a few months. We have compared the performance of our substrate with theirs. They have gold, silver and gold+silver based substrates.

Since they have listed detectable analyte amounts in terms of part per million (ppm) and part per billion (ppb), we have converted this value to molarity.

The comparison for **Rhodamine B** is as follows:

Commercially available data:

Substrate used: RAM SERS AU:

Concentration: $40\,ppm$

Time: 3 seconds

Laser Power: $15\,mW$

Raman Intensity: 1500 counts

Our SERS substrate data:

Concentration: $5\,\mu M$

Time:1 second

Laser Power: $250\,mW$

Raman Intensity: 3000 counts

First we have to convert 40 ppm into molarity.

$$40\,\text{ppm} = \frac{40\,\frac{mg}{L}}{480\,\frac{g}{M}} = 83\mu M \tag{6.5}$$

Therefore:

$$\frac{EF_{\text{ours}}}{EF_{\text{commercail}}} = \frac{83\,\mu M}{5\,\mu M} \times \frac{3\,s}{1\,s} \times \frac{3000}{1500} \times \frac{15\,mW}{250\,mW} \approx 6 \tag{6.6}$$

Our substrate performed actually 6 times better for RhB measurements.

The comparison for **Crystal Violet** is as follows:

Commercially available data:

Substrate used: RAM SERS AU:

Concentration: $1\,ppm$

Time: 1 seconds

Laser Power: $21.2\,mW$

Raman Intensity: 2500 counts

Our SERS substrate data:

Concentration: $1\,\mu M$

Time:1 second

Laser Power: $250\,mW$

Raman Intensity: 500 counts

First we have to convert 1 ppm into molarity.

$$1\,\text{ppm} = \frac{1\,\frac{mg}{L}}{408\,\frac{g}{M}} = 2.5\mu M \tag{6.7}$$

Therefore:

$$\frac{EF_{\text{ours}}}{EF_{\text{commercail}}} = \frac{2.5\,\mu M}{1\,\mu M} \times \frac{1\,s}{1\,s} \times \frac{500}{2500} \times \frac{21.2\,mW}{250\,mW} \approx \frac{1}{23} \tag{6.8}$$

In this case our substrate performed 23 times worse.

Nevertheless, our substrate with CuO nanoparticles perform practically at the same level as the commercially available substrates.

In conclusion, we have experimentally found that using just the ultra-pure water as the electrolyte and the copper electrodes, ions extracted from the anode form copper oxide nanoparticles on the anode surface in matter of minutes. As a proof of principle experiment, we used this anode electrode as a SERS substrate for enhancing the Raman peaks of RhB and CV and obtained EF factors over five orders of magnitude. The proposed method has some key advantages over existing SERS substrates: it is not only a real time SERS substrate but also is a very fast, simple and a low cost technique. This technique also allows preparation of a large effective area for SERS enhancement, virtually unlimited area as long as the current is uniform over the substrate during the electrolysis. Although nanocubes are the only nanoparticles produced and in random orientation, their size is controllable, and the repeatability of the substrate, as far as the nanoparticle size is concerned, is excellent. Furthermore this substrate is tunable in wavelength, although irreversibly and only in one direction. We also investigated other metal electrodes including Ag, Al, Zn and brass for their real time SERS substrate capability, which none of them except brass exposed this capability, nanoparticles were produced only at copper and brass anodes for electrolysis times up-to ten minutes. An explanation for CuO nanoparticle formation on anodes made of copper and brass but not with other metals is given using standard electrode potentials of the metals. Also, surface plasmon resonance simulations of the nanoparticles were performed in accord with the nanoparticle distributions obtained from the SEM images. The simulation results agree with the change in SERS intensity as a function of time since as the nanoparticles grow in size SPR wavelengths shift.

Chapter 7

Conclusion

In conclusion, this thesis composed of two parts, each of them discusses different topics related to Raman spectroscopy.

In the first part of this thesis a novel broadband static Fourier transform spectrometer (static-FTS) configuration based on the division of the spectrum into multiple narrow-bands is proposed and implemented by combining a static-FTS and dispersive elements. Dividing the broadband input spectrum into narrow-band signals we have used the band-pass sampling theorem to reduce the sampling frequency (or increase the scanning step in the FTS concept). The dispersive part includes a double diffraction grating structure to disperse the input spectrum in horizontal direction (to divide the input light into multiple narrow-band signals) and the static-FTS part includes a static Michelson interferometer to make different PLDs in the vertical direction. The static Michelson interferometer is composed of a beam-splitter (BS), a flat mirror and a stair-case mirror. However, in actual setup a diffraction grating in Littrow configuration is used to realize the stair-case mirror. The effect of this configuration on the visibility of the spectrometer is also studied. Using off-shelf diffraction gratings as the stair-case mirror decreases the total cost of the prototyped device. A CCD camera is used at the exit port of the static-FTS part, to record the formed interferograms.

The proposed configuration not only decreases the spectrometer size but also allows operation in the traditional spectrometer wavelength range, namely $400\,nm - 1100\,nm$

with better resolution. This technique solves the Nyquist sampling rate issue and enables recording high resolution spectrums with regular CCDs. The proposed configuration and the method, in fact, solve the trade of between resolution and bandwidth, and also eliminate the need for nanometer step size mirrors. An algorithm is developed to process the recorded signal and calculate the Fourier transform of the recorded interferograms on the CCD camera. Finally, the recorded spectrums with the prototyped spectrometer are compared with the results of a commercially available spectrometer.

In the second part, we have shown the capability of copper oxide (CuO) nanoparticles formed on copper (Cu) electrodes by the electrolysis as a real time active substrate for surface enhanced Raman scattering (SERS). We have experimentally found that using just the ultra pure water as the electrolyte and the Cu electrodes, ions are extracted from the copper anode form copper oxide nanoparticles on the anode surface in matter of minutes. Average particle size on the anode reaches to 100 nm in ninety seconds and grows to about 300 nm in five minutes. This anode is used in SERS experiments in real time as the nanoparticles were forming and the maximum enhancement factor (EF) of Raman signals were over five orders of magnitude. Other metal electrodes made of brass, zinc (Zn), silver (Ag) and aluminum (Al) also tested as candidate anode materials for their potential as real-time substrates for SERS applications. Experimentally obtained enhancement factors were above five orders of magnitude for brass electrodes like the copper but for the other metals no enhancement is observed. Electron microscope images show the cubic nanoparticle formation on copper and brass electrodes but none in the other metals studied.

The proposed method has some key advantages over existing SERS substrates: its not only a real time SERS substrate but also is a very fast, simple and a low cost technique. Furthermore this substrate is tunable in wavelength -albeit only irreversibly and in one direction- as the particle size is increasing as a function of time which implies that plasmon resonance wavelengths are increasing as well. This technique also omits the need for an electrolyte of containing the metal ions of interest for the nanoparticle production as just the deionized or distilled water is enough. This is an important point for the SERS measurements because the electrolyte being simply just the water there will not be an extra background noise added to the spectrum. This technique also allows preparation of a large effective area for SERS enhancement, virtually unlimited area. As long as the current distribution over the anode is uniform which is a trivial arrangement, nanoparticle distribution will have quite homogeneous distribution. The homogeneous nanoparticles distribution means a uniform enhancement factor on the produced substrate.

The results are also compared with commercially available substrates, which our substrate with CuO nanoparticles performs practically at the same level as the available substrates made of gold and silver. Our substrate is a real-time and low cost substrate which high tech facilities are not required to fabricate it. The commercially available substrates have a limited shelf life namely a few months, high tech facilities are need, and also are costly.

Future Works

- In this thesis the proposed configuration as the broadband and high resolution static-FTS was implemented by a small 1.3 megapixels CCD camera. Since the CCD dimensions determines the bandwidth and resolution of the spectrometer, one can increase the device bandwidth as well as its optical resolution by using a larger CCD camera. Another important to note is, one should order a CCD camera with specific pixel dimensions as discussed in the section 4.4. This spectrometer can be commercialized using a specific CCD as already mentioned.
- For higher SERS enhancement factor one needs dimer and trimmer structures. Therefor it is possible to increase the enhancement factor of the real-time SERS substrates by controlling the inter-particle distance.
- Under the discussed conditions in this thesis, we could only use copper and brass electrodes as the real-time SERS substrates. Therefore, studying the conditions in which other metals also can be used as a real-time SERS substrate can be another future work.
- Right now the commercially available SERS active substrates are costly and also have a limited area and shelf life time. Since the discussed method as the real-time SERS substrate here, is a simple method and also it is possible to fabricate a SERS active substrate in real-time, with commercializing the suggested method as the SERS probe, one can produce SERS substrates with no time or SERS active area limitations.

Bibliography

[1] Chuyang Y Tang, Young-Nam Kwon, and James O Leckie. Effect of membrane chemistry and coating layer on physiochemical properties of thin film composite polyamide ro and nf membranes: I. FTIR and XPS characterization of polyamide and coating layer chemistry. *Desalination*, 242(1):149–167, 2009.

[2] Jopi JW Mikkonen, Jussi Raittila, Lassi Rieppo, Reijo Lappalainen, Arja M Kullaa, and Sami Myllymaa. Fourier transform infrared spectroscopy and photoacoustic spectroscopy for saliva analysis. *Applied Spectroscopy*, 70(9):1502–1510, 2016.

[3] Jinyang Li, Dan-Feng Lu, and Zhi-Mei Qi. A prototype stationary Fourier transform spectrometer for near-infrared absorption spectroscopy. *Applied Spectroscopy*, 69(9):1112–1117, 2015.

[4] Antoine Lacan, François-Marie Bréon, Alain Rosak, Frank Brachet, Lionel Roucayrol, Pierre Etcheto, Christophe Casteras, and Yves Salaün. A static Fourier transform spectrometer for atmospheric sounding: concept and experimental implementation. *Optics Express*, 18(8):8311–8331, 2010.

[5] Boglárka Balázs, Péter Sipos, Corina Danciu, Stefana Avram, Codruta Soica, Cristina Dehelean, Gábor Varju, Gábor Erős, Mária Budai-Szűcs, Szilvia Berkó, et al. ATR-FTIR and Raman spectroscopic investigation of the electroporation-mediated transdermal delivery of a nanocarrier system containing an antitumour drug. *Biomedical Optics Express*, 7(1):67–78, 2016.

[6] Brian C. Smith. *Fundamentals of Fourier transform infrared spectroscopy.* CRC Press, second edition, 1995.

[7] A Synytsya. Fourier transform Raman and infrared spectroscopy of pectins. *Carbohydrate Polymers*, 54(1):97–106, 2003.

[8] A A Balashov, G D Bogomolov, A P Kiryanov, A K Nikitin, V I Pustovoit, V A Vaguin, and G N Zhizhin. Asymmetric static Fourier-spectrometer for solid surfaces and nano-films study. *Vibrational Spectroscopy*, 43(1):46–48, 2007.

[9] M Beekes, P Lasch, and D Naumann. Analytical applications of Fourier transform-infrared (FT-IR) spectroscopy in microbiology and prion research. *Veterinary Microbiology*, 123(4):305–319, 2007.

[10] G. R. Sauer, W. B. Zunic, J. R. Durig, and R. E. Wuthier. Fourier transform Raman spectroscopy of synthetic and biological calcium phosphates. *Calcified Tissue International*, 54(5):414–420, may 1994.

[11] Antoine Lacan, François-Marie Bréon, Alain Rosak, Frank Brachet, Lionel Roucayrol, Pierre Etcheto, Christophe Casteras, and Yves Salaün. A static Fourier transform spectrometer for atmospheric sounding: concept and experimental implementation. *Optics Express*, 18(8):8311–31, apr 2010.

[12] C. Pierangelo, P. Hébert, C. Camy-peyret, C. Clerbaux, P. Coheur, T. Phulpin, L. Lavanant, T. Tremas, P. Henry, and A. Rosak. SIFTI: a static infrared Fourier transform interferometer dedicated to ozone and CO pollution monitoring. In *ITSC16 Proceedings*, 2008.

[13] Brian C Smith. *Fundamentals of Fourier transform infrared spectroscopy*. CRC press, 2011.

[14] Vidi Saptari. *Fourier transform spectroscopy instrumentation engineering*. SPIE Optical Engineering Press, 2003.

[15] Peter R Griffiths and James A De Haseth. *Fourier transform infrared spectrometry*, volume 171. John Wiley & Sons, 2007.

[16] R Glenn Sellar and Glenn D Boreman. Comparison of relative signal-to-noise ratios of different classes of imaging spectrometer. *Applied Optics*, 44(9):1614–1624, 2005.

[17] Stephen E Bialkowski. Overcoming the multiplex disadvantage by using maximum-likelihood inversion. *Applied Spectroscopy*, 52(4):591–598, 1998.

[18] Janine Connes and Pierre Connes. Near-infrared planetary spectra by Fourier spectroscopy. i. instruments and results. *JOSA*, 56(7):896–910, 1966.

[19] Liang Jing-qiu, Liang Zhong-zhu, L V Jin-guang, F U Jian-guo, and Zheng Ying. Simulation and experiment of the static FTIR based on micro multi-step mirrors. In *International Symposium on Photoelectronic Detection and Imaging 2011: Sensor and Micromachined Optical Device Technologies*, volume 8191, pages 10–17, 2011.

[20] Jun Zhao and Richard L. McCreery. Multichannel FT-Raman spectroscopy: noise analysis and performance assessment. *Applied Spectroscopy*, 51(11):1687–1697, nov 1997.

[21] Frank Brachet, Philippe-Jean Hébert, Elodie Cansot, Christian Buil, Antoine Lacan, Lionel Roucayrol, Etienne Courau, Frédéric Bernard, Christophe Casteras, Jacques Loesel, and Clémence Pierangelo. Static Fourier transform spectroscopy breadboards for atmospheric chemistry and climate. In *SPIE Europe Proceedings*, number 2, pages 81–87, 2008.

[22] Michael Schardt, Patrik J Murr, Markus S Rauscher, Anton J Tremmel, Benjamin R Wiesent, and Alexander W Koch. Static Fourier transform infrared spectrometer. *Optics Express*, 24(7):7767–7776, 2016.

[23] Takanori Kiyokura, Takahiro Ito, and Renshi Sawada. Fourier transform near-infrared spectrometer using a corner-cube integrated prism scanning interferometer. *Applied Spectroscopy*, 58(12):1447–1451, 2004.

[24] *https://oceanotics.com.*

[25] *http://www.citizenscales.net/.*

[26] Behzad Sardari, Federico Davoli, and Meriç Özcan. A simple configuration for static Fourier transform infrared spectrometers. In *SPIE Photonics Europe*, pages 98990T–98990T. International Society for Optics and Photonics, 2016.

[27] R.G. Vaughan, N.L. Scott, and D.R. White. The theory of bandpass sampling. *IEEE Transactions on Signal Processing*, 39(9):1973–1984, 1991.

[28] Behzad Sardari, Federico Davoli, and Meriç Özcan. A broadband configuration for static Fourier transform spectroscopy with bandpass sampling. *Review of Scientific Instruments*, 87(10):103106, 2016.

[29] Sumner P. Davis, Mark C. Abrams, and J. W. (James W.) Brault. *Fourier transform spectrometry*. Academic Press, first edition, 2001.

[30] Peter J Miller and Andy R Harvey. Signal to noise analysis of various imaging systems. In *Proceedings of SPIE*, volume 4259, pages 16–21, 2001.

[31] R. Glenn Sellar and Glenn D. Boreman. Comparison of relative signal-to-noise ratios of different classes of imaging spectrometer. *Applied Optics*, 44(9):1614, mar 2005.

[32] K Venkateswarlu. Relative intensities of stokes and anti-stokes Raman lines in crystals. In *Proceedings of the Indian Academy of Sciences-Section A*, volume 13, pages 64–67. Springer, 1941.

[33] Derek Albert Long and DA Long. *Raman Spectroscopy*, volume 206. McGraw-Hill New York, 1977.

[34] Herman A Szymanski. *Raman spectroscopy: theory and practice*. Springer Science & Business Media, 2012.

[35] Jeankun Oh. *Transcutaneous measurement of glucose using Raman spectroscopy*. PhD thesis, Massachusetts Institute of Technology, 2004.

[36] Tae-Woong Koo. *Measurement of glucose in human blood serum using near-infrared Raman spectroscopy*. PhD thesis, Massachusetts Institute of Technology, 1998.

[37] Ishan Barman, Chae-Ryon Kong, Gajendra P Singh, Ramachandra R Dasari, and Michael S Feld. Accurate spectroscopic calibration for noninvasive glucose monitoring by modeling the physiological glucose dynamics. *Analytical Chemistry*, 82(14):6104–6114, 2010.

[38] XN He, J Allen, PN Black, T Baldacchini, X Huang, H Huang, L Jiang, and YF Lu. Coherent anti-stokes Raman scattering and spontaneous Raman spectroscopy and microscopy of microalgae with nitrogen depletion. *Biomedical Optics Express*, 3(11):2896–2906, 2012.

[39] Conor L Evans and X Sunney Xie. Coherent anti-stokes Raman scattering microscopy: chemical imaging for biology and medicine. *Annu. Rev. Anal. Chem.*, 1:883–909, 2008.

[40] Ji-Xin Cheng and X Sunney Xie. Coherent anti-stokes Raman scattering microscopy: instrumentation, theory, and applications, 2004.

[41] Eric O Potma, Conor L Evans, and X Sunney Xie. Heterodyne coherent anti-stokes Raman scattering (CARS) imaging. *Optics Letters*, 31(2):241–243, 2006.

[42] RF Begley, AB Harvey, and Robert L Byer. Coherent anti-stokes Raman spectroscopy. *Applied Physics Letters*, 25(7):387–390, 1974.

[43] Dan Fu, Fa-Ke Lu, Xu Zhang, Christian Freudiger, Douglas R Pernik, Gary Holtom, and Xiaoliang Sunney Xie. Quantitative chemical imaging with multiplex stimulated Raman scattering microscopy. *Journal of the American Chemical Society*, 134(8):3623–3626, 2012.

[44] Yasuyuki Ozeki, Fumihiro Dake, Shinichiro Kajiyama, Kiichi Fukui, and Kazuyoshi Itoh. Analysis and experimental assessment of the sensitivity of stimulated Raman scattering microscopy. *Optics Express*, 17(5):3651–3658, 2009.

[45] Yasuyuki Ozeki, Yuma Kitagawa, Kazuhiko Sumimura, Norihiko Nishizawa, Wataru Umemura, Shinichiro Kajiyama, Kiichi Fukui, and Kazuyoshi Itoh. Stimulated Raman scattering microscope with shot noise limited sensitivity using subharmonically synchronized laser pulses. *Optics Express*, 18(13):13708–13719, 2010.

[46] Christian W Freudiger, Wei Min, Brian G Saar, Sijia Lu, Gary R Holtom, Chengwei He, Jason C Tsai, Jing X Kang, and X Sunney Xie. Label-free biomedical imaging with high sensitivity by stimulated Raman scattering microscopy. *Science*, 322(5909):1857–1861, 2008.

[47] Brian G Saar, Christian W Freudiger, Jay Reichman, C Michael Stanley, Gary R Holtom, and X Sunney Xie. Video-rate molecular imaging in vivo with stimulated Raman scattering. *Science*, 330(6009):1368–1370, 2010.

---

[48] Katrin Kneipp, Harald Kneipp, Irving Itzkan, Ramachandra R Dasari, and Michael S Feld. Surface-enhanced Raman scattering and biophysics. *Journal of Physics: Condensed Matter*, 14(18):R597, 2002.

[49] A Otto, I Mrozek, H Grabhorn, and W Akemann. Surface-enhanced Raman scattering. *Journal of Physics: Condensed Matter*, 4(5):1143, 1992.

[50] Michael J Weaver, Shouzhong Zou, and Ho Yeung H Chan. Peer reviewed: the new interfacial ubiquity of surface-enhanced Raman spectroscopy, 2000.

[51] Shangyuan Feng, Duo Lin, Juqiang Lin, Buhong Li, Zufang Huang, Guannan Chen, Wei Zhang, Lan Wang, Jianji Pan, Rong Chen, et al. Blood plasma surface-enhanced Raman spectroscopy for non-invasive optical detection of cervical cancer. *Analyst*, 138(14):3967–3974, 2013.

[52] Hae Mi Lee, Seung Min Jin, Hyung Min Kim, and Yung Doug Suh. Single-molecule surface-enhanced Raman spectroscopy: a perspective on the current status. *Physical Chemistry Chemical Physics*, 15(15):5276–5287, 2013.

[53] Marcos Ghislandi, Günter G Hoffmann, Evgeniy Tkalya, Lijing Xue, and Gijsbertus De With. Tip-enhanced Raman spectroscopy and mapping of graphene sheets. *Applied Spectroscopy Reviews*, 47(5):371–381, 2012.

[54] Kristen D Alexander and Zachary D Schultz. Tip-enhanced Raman detection of antibody conjugated nanoparticles on cellular membranes. *Analytical Chemistry*, 84(17):7408–7414, 2012.

[55] Raoul M Stöckle, Yung Doug Suh, Volker Deckert, and Renato Zenobi. Nanoscale chemical analysis by tip-enhanced Raman spectroscopy. *Chemical Physics Letters*, 318(1):131–136, 2000.

[56] V Deckert. Tip-enhanced Raman spectroscopy. *Journal of Raman Spectroscopy*, 40(10):1336–1337, 2009.

[57] Jens Steidtner and Bruno Pettinger. Tip-enhanced Raman spectroscopy and microscopy on single dye molecules with 15 nm resolution. *Physical Review Letters*, 100(23):236101, 2008.

[58] Bhavya Sharma, M Fernanda Cardinal, Samuel L Kleinman, Nathan G Greeneltch, Renee R Frontiera, Martin G Blaber, George C Schatz, and Richard P Van Duyne. High-performance SERS substrates: Advances and challenges. *MRS Bulletin*, 38(08):615–624, 2013.

[59] Martin Fleischmann, Patrick J Hendra, and AJ McQuillan. Raman spectra of pyridine adsorbed at a silver electrode. *Chemical Physics Letters*, 26(2):163–166, 1974.

[60] David L Jeanmaire and Richard P Van Duyne. Surface Raman spectroelectrochemistry: Part i. heterocyclic, aromatic, and aliphatic amines adsorbed on the anodized silver electrode. *Journal of Electroanalytical Chemistry and Interfacial Electrochemistry*, 84(1):1–20, 1977.

[61] M Grant Albrecht and J Alan Creighton. Anomalously intense Raman spectra of pyridine at a silver electrode. *Journal of the American Chemical Society*, 99(15):5215–5217, 1977.

[62] Paul L Stiles, Jon A Dieringer, Nilam C Shah, and Richard P Van Duyne. Surface-enhanced Raman spectroscopy. *Annu. Rev. Anal. Chem.*, 1:601–626, 2008.

[63] Katrin Kneipp, Harald Kneipp, I Itzkan, RR Dasari, and MS Feld. Surface-enhanced Raman scattering: A new tool for biomedical spectroscopy. *Curr. Sci*, 77(7):915–924, 1999.

[64] Meikun Fan, Gustavo FS Andrade, and Alexandre G Brolo. A review on the fabrication of substrates for surface enhanced Raman spectroscopy and their applications in analytical chemistry. *Analytica Chimica Acta*, 693(1):7–25, 2011.

[65] Jordan F Betz, W Yu Wei, Yi Cheng, Ian M White, and Gary W Rubloff. Simple SERS substrates: powerful, portable, and full of potential. *Physical Chemistry Chemical Physics*, 16(6):2224–2239, 2014.

[66] Zhenglong Zhang, Pengfei Yang, Hongxing Xu, and Hairong Zheng. Surface enhanced fluorescence and Raman scattering by gold nanoparticle dimers and trimers. *Journal of Applied Physics*, 113(3):033102, 2013.

[67] Chris Oubre and Peter Nordlander. Finite-difference time-domain studies of the optical properties of nanoshell dimers. *The Journal of Physical Chemistry B*, 109(20):10042–10051, 2005.

[68] Pingping Zhang, Shumin Yang, Liansheng Wang, Jun Zhao, Zhichao Zhu, Bo Liu, Jun Zhong, and Xuhui Sun. Large-scale uniform Au nanodisk arrays fabricated via X-ray interference lithography for reproducible and sensitive SERS substrate. *Nanotechnology*, 25(24):245301, 2014.

[69] Shuming Nie and Steven R Emory. Probing single molecules and single nanoparticles by surface-enhanced Raman scattering. *Science*, 275(5303):1102–1106, 1997.

[70] Katrin Kneipp, Yang Wang, Harald Kneipp, Lev T Perelman, Irving Itzkan, Ramachandra R Dasari, and Michael S Feld. Single molecule detection using surface-enhanced Raman scattering (SERS). *Physical Review Letters*, 78(9):1667, 1997.

[71] Yoshihiro MARUYAMA, Mitsuru ISHIKAWA, and Masayuki FUTAMATA. Single molecule detection with SERS. *Analytical Sciences/Supplements*, 17(0):i1181–i1183, 2002.

[72] Hongwen Liu, Ling Zhang, Xingyou Lang, Yoshinori Yamaguchi, Hiroshi Iwasaki, Yasushi Inouye, Qikun Xue, and Mingwei Chen. Single molecule detection from a large-scale SERS-active Au79Ag21 substrate. *Scientific Reports*, 1:112, 2011.

[73] BH Loo. Observation of the surface enhanced Raman scattering effect from the semiconductorelectrolyte interface. *Journal of Electroanalytical Chemistry and Interfacial Electrochemistry*, 136(1):209–213, 1982.

[74] H Yamada and Y Yamamoto. Surface enhanced Raman scattering (SERS) of chemisorbed species on various kinds of metals and semiconductors. *Surface Science*, 134(1):71–90, 1983.

[75] Ping Zhang, Yinsheng Wang, Tianjing He, Baozhong Zhang, Xiuyan Wang, Houwen Xin, and Fan-chen Liu. SERS of pyridine, 1, 4-dioxane and 1-ethyl-3-methyl-2-thiacyanine iodide adsorbed on α-Fe2O3 colloids. *Chemical Physics Letters*, 153(2-3):215–222, 1988.

[76] C Mou, T He, X Wang, Fan-Zhen Liu, Ji-Sen Jiang, and Long-Wu Chen. Surface enhanced Raman scattering (SERS) from H˜ 2TSPP and Ag (ii) TSPP adsorbed on uniform Fe˜ 3O˜ 4 colloids. *ACTA PHYSICOCHIMICA SINICA*, 12:841–844, 1996.

[77] A Kudelski, M Janik-Czachor, J Bukowska, M Dolata, and A Szummer. Surface-enhanced Raman scattering (SERS) on copper electrodeposited under nonequilibrium conditions. *Journal of Molecular Structure*, 482:245–248, 1999.

[78] WANG Yanfei, HU Hailong, JING Shengyu, WANG Yunxin, SUN Zhihua, ZHAO Bing, ZHAO Chun, and John R Lombardi. Enhanced Raman scattering as a probe for 4-mercaptopyridine surface-modified copper oxide nanocrystals. *Analytical Sciences*, 23(7):787–791, 2007.

[79] Yanfei Wang, Zhihua Sun, Hailong Hu, Shengyu Jing, Bing Zhao, Weiqing Xu, Chun Zhao, and John R Lombardi. Raman scattering study of molecules adsorbed on ZnS nanocrystals. *Journal of Raman Spectroscopy*, 38(1):34–38, 2007.

[80] Yanfei Wang, Zhihua Sun, Yunxin Wang, Hailong Hu, Bing Zhao, Weiqing Xu, and John R Lombardi. Surface-enhanced Raman scattering on mercaptopyridine-capped CdS microclusters. *Spectrochimica Acta Part A: Molecular and Biomolecular Spectroscopy*, 66(4):1199–1203, 2007.

[81] Libin Yang, Xin Jiang, Weidong Ruan, Bing Zhao, Weiqing Xu, and John R Lombardi. Observation of enhanced Raman scattering for molecules adsorbed on TiO2 nanoparticles: charge-transfer contribution. *The Journal of Physical Chemistry C*, 112(50):20095–20098, 2008.

[82] Yanfei Wang, Junhu Zhang, Huiying Jia, Minjie Li, Jianbo Zeng, Bai Yang, Bing Zhao, Weiqing Xu, and John R Lombardi. Mercaptopyridine surface-functionalized CdTe quantum dots with enhanced Raman scattering properties. *The Journal of Physical Chemistry C*, 112(4):996–1000, 2008.

[83] Yanfei Wang, Weidong Ruan, Junhu Zhang, Bai Yang, Weiqing Xu, Bing Zhao, and John R Lombardi. Direct observation of surface-enhanced Raman scattering in ZnO nanocrystals. *Journal of Raman Spectroscopy*, 40(8):1072–1077, 2009.

[84] Xiaotian Wang, Wensheng Shi, Guangwei She, and Lixuan Mu. Surface-enhanced Raman scattering (SERS) on transition metal and semiconductor nanostructures. *Physical Chemistry Chemical Physics*, 14(17):5891–5901, 2012.

[85] Naidu Dhanpal Jayram, D Aishwarya, S Sonia, D Mangalaraj, P Suresh Kumar, and G Mohan Rao. Analysis on superhydrophobic silver decorated copper oxide nanostructured thin films for SERS studies. *Journal of Colloid and Interface Science*, 477:209–219, 2016.

[86] Hao Wu, Hua Wang, and Guanghai Li. Metal oxide semiconductor SERS-active substrates by defect engineering. *Analyst*, 2017.

[87] Aneta Aniela Kowalska, Agnieszka Kaminska, Witold Adamkiewicz, Evelin Witkowska, and Marek Tkacz. Novel highly sensitive Cu-based SERS platforms for biosensing applications. *Journal of Raman Spectroscopy*, 46(5):428–433, 2015.

[88] Eric Le Ru and Pablo Etchegoin. *Principles of surface-enhanced Raman spectroscopy: and related plasmonic effects*. Elsevier, 2008.

[89] Alan X Wang and Xianming Kong. Review of recent progress of plasmonic materials and nano-structures for surface-enhanced Raman scattering. *Materials*, 8(6):3024–3052, 2015.

[90] Yuliang Wang and Younan Xia. Bottom-up and top-down approaches to the synthesis of monodispersed spherical colloids of low melting-point metals. *Nano Letters*, 4(10):2047–2050, 2004.

[91] Xiaoshuang Shen, Liyong Chen, Dehui Li, Liangfang Zhu, Hong Wang, Cuicui Liu, Yong Wang, Qihua Xiong, and Hongyu Chen. Assembly of colloidal nanoparticles directed by the microstructures of polycrystalline ice. *ACS Nano*, 5(10):8426–8433, 2011.

[92] Ales Panacek, Libor Kvitek, Robert Prucek, Milan Kolar, Renata Vecerova, Nadezda Pizurova, Virender K Sharma, Tat'jana Nevecna, and Radek Zboril. Silver colloid nanoparticles: synthesis, characterization, and their antibacterial activity. *The Journal of Physical Chemistry B*, 110(33):16248–16253, 2006.

[93] Taeghwan Hyeon. Chemical synthesis of magnetic nanoparticles. *Chemical Communications*, (8):927–934, 2003.

[94] Fei Hu, Haiyang Lin, Zhaoshun Zhang, Fan Liao, Mingwang Shao, Yeshayahu Lifshitz, and Shuit-Tong Lee. Smart liquid SERS substrates based on Fe3O4/Au nanoparticles with reversibly tunable enhancement factor for practical quantitative detection. *Scientific Reports*, 4, 2014.

[95] Kihoon Kim, Hye Soo Han, Inhee Choi, Chiwon Lee, SoonGweon Hong, Sang-Hee Suh, Luke P Lee, and Taewook Kang. Interfacial liquid-state surface-enhanced Raman spectroscopy. *Nature Communications*, 4, 2013.

[96] Werayut Srituravanich, Nicholas Fang, Cheng Sun, Qi Luo, and Xiang Zhang. Plasmonic nanolithography. *Nano Letters*, 4(6):1085–1088, 2004.

[97] Hua Zhang, Sung-Wook Chung, and Chad A Mirkin. Fabrication of sub-50-nm solid-state nanostructures on the basis of dip-pen nanolithography. *Nano Letters*, 3(1):43–45, 2003.

[98] GM Wallraff and WD Hinsberg. Lithographic imaging techniques for the formation of nanoscopic features. *Chemical Reviews*, 99(7):1801–1822, 1999.

[99] ES Snow, PM Campbell, and FK Perkins. High speed patterning of a metal silicide using scanned probe lithography. *Applied Physics Letters*, 75(10):1476–1478, 1999.

[100] Jon Orloff, LW Swanson, and Mark Utlaut. Fundamental limits to imaging resolution for focused ion beams. *Journal of Vacuum Science & Technology B*, 14(6):3759–3763, 1996.

[101] Jin Min Cheon, Jin Ha Lee, Yongsul Song, and Jongryoul Kim. Synthesis of Ag nanoparticles using an electrolysis method and application to inkjet printing. *Colloids and Surfaces A: Physicochemical and Engineering Aspects*, 389(1):175–179, 2011.

[102] Jinmin Cheon, Jinha Lee, and Jongryoul Kim. Inkjet printing using copper nanoparticles synthesized by electrolysis. *Thin Solid Films*, 520(7):2639–2643, 2012.

[103] Xiao-Feng Tang, Zhen-Guo Yang, and Wei-Jiang Wang. A simple way of preparing high-concentration and high-purity nano copper colloid for conductive ink in inkjet printing technology. *Colloids and Surfaces A: Physicochemical and Engineering Aspects*, 360(1):99–104, 2010.

[104] Gao-Qing Yuan, Huan-Feng Jiang, Chang Lin, and Shi-Jun Liao. Shape-and size-controlled electrochemical synthesis of cupric oxide nanocrystals. *Journal of Crystal Growth*, 303(2):400–406, 2007.

[105] Minwei Xu, Fei Wang, Bingjun Ding, Xiaoping Song, and Jixiang Fang. Electrochemical synthesis of leaf-like CuO mesocrystals and their lithium storage properties. *RSC Advances*, 2(6):2240–2243, 2012.

[106] Lu Lu and Xirong Huang. Room temperature electrochemical synthesis of CuO flower-like microspheres and their electrooxidative activity towards hydrogen peroxide. *Microchimica Acta*, 175(1-2):151–157, 2011.

[107] Qiaobao Zhang, Kaili Zhang, Daguo Xu, Guangcheng Yang, Hui Huang, Fude Nie, Chenmin Liu, and Shihe Yang. CuO nanostructures: synthesis, characterization, growth mechanisms, fundamental properties, and applications. *Progress in Materials Science*, 60:208–337, 2014.

[108] Nillohit Mukherjee, Bibhutibhushan Show, Swarup Kumar Maji, Utpal Madhu, Sanjib Kumar Bhar, Bibhas Chandra Mitra, Gobinda Gopal Khan, and Anup Mondal. CuO nano-whiskers: electrodeposition, Raman analysis, photoluminescence study and photocatalytic activity. *Materials Letters*, 65(21):3248–3250, 2011.

[109] Jianwen Xu, Ke Yu, Jin Wu, Dejian Shang, Lijun Li, Yu'e Xu, and Ziqiang Zhu. Synthesis, field emission and humidity sensing characteristics of honeycomb-like CuO. *Journal of Physics D: Applied Physics*, 42(7):075417, 2009.

[110] Buppachat Toboonsung and Pisith Singjai. Formation of CuO nanorods and their bundles by an electrochemical dissolution and deposition process. *Journal of Alloys and Compounds*, 509(10):4132–4137, 2011.

[111] Behzad Sardari and Meriç Özcan. Real-time and tunable substrate for surface enhanced Raman spectroscopy by synthesis of copper oxide nanoparticles via electrolysis. *Scientific Reports*, 7(7730), 2017.

[112] Dinesh Pratap Singh, Nageswara Rao Neti, ASK Sinha, and Onkar Nath Srivastava. Growth of different nanostructures of Cu2O (nanothreads, nanowires, and nanocubes) by simple electrolysis based oxidation of copper. *The Journal of Physical Chemistry C*, 111(4):1638–1645, 2007.

[113] Stefan Alexander Maier. *Plasmonics: fundamentals and applications*. Springer Science & Business Media, 2007.

[114] Peter Nordlander, C Oubre, E Prodan, K Li, and MI Stockman. Plasmon hybridization in nanoparticle dimers. *Nano Letters*, 4(5):899–903, 2004.

[115] Daniel W Brandl, Nikolay A Mirin, and Peter Nordlander. Plasmon modes of nanosphere trimers and quadrumers. *The Journal of Physical Chemistry B*, 110(25):12302–12310, 2006.

[116] Perrin Walker and William H Tarn. *CRC handbook of metal etchants*. CRC press, 1990.

[117] Dahlang Tahir and Sven Tougaard. Electronic and optical properties of Cu, CuO and Cu2O studied by electron spectroscopy. *Journal of Physics: Condensed Matter*, 24(17):175002, 2012.

[118] Adam D McFarland, Matthew A Young, Jon A Dieringer, and Richard P Van Duyne. Wavelength-scanned surface-enhanced Raman excitation spectroscopy. *The Journal of Physical Chemistry B*, 109(22):11279–11285, 2005.

[119] Martin Moskovits. Surface-enhanced Raman spectroscopy: a brief retrospective. *Journal of Raman Spectroscopy*, 36(6-7):485–496, 2005.